Compressed Sensing Based Micro-CT Methods and Applications

Kriti Sen Sharma

Dissertation submitted to the Faculty of the
Virginia Polytechnic Institute and State University
in partial fulfillment of the requirements for the degree of

Doctor of Philosophy
in
Electrical Engineering

Ge Wang, Chair
Christopher L. Wyatt
Claudio da Silva
Nicholas Polys
Shuhai Xiao

May 2, 2013
Blacksburg, Virginia

Keywords: compressed-sensing, x-ray micro-CT, image reconstruction, few-view CT,
interior tomography, offset detector CT

Compressed Sensing Based Micro-CT Methods and Applications

Kriti Sen Sharma

(ABSTRACT)

High-resolution micro computed tomography (micro-CT) offers 3D image resolution of 1 μm for non-destructive evaluation of various samples. However, the micro-CT performance is limited by several factors. Primarily, scan time is extremely long, and sample dimension is restricted by the x-ray beam and the detector size. The latter is the cause for the well-known interior problem. Recent advancement in image reconstruction, spurred by the advent of compressed sensing (CS) theory in 2006 and interior tomography theory since 2007, offers great reduction in the number of views and an increment in the volume of samples, while maintaining reconstruction accuracy. Yet, for a number of reasons, traditional filtered back-projection based reconstruction methods remain the *de facto* standard on all manufactured scanners.

This work demonstrates that CS based global and interior reconstruction methods can enhance the imaging capability of micro-CT scanners. First, CS based few-view reconstruction methods have been developed for use with data from a real micro-CT scanner. By achieving high quality few-view reconstruction, the new approach is able to reduce micro-CT scan time to up to $1/8^{th}$ of the time required by the conventional protocol. Next, two new reconstruction techniques have been developed that allow accurate interior reconstruction using just a limited number of global scout views as additional information. The techniques represent a significant progress relative to the previous methods that assume a fully sampled global scan. Of the two methods, the second method uses CS techniques and does not place any restrictions on scanning geometry. Finally, analytic and iterative reconstruction methods have been developed for enlargement of the field of view for the interior scan with a small detector. The idea is that truncated projections are acquired in an offset detector geometry, and the reconstruction procedure is performed through the use of a weighting function / weighted iteration updates, and projection completion. The CS based reconstruction yields the highest image quality in the numerical simulation. Yet, some limitations of the CS based techniques are observed in case of real data with various imperfect properties. In all the studies, physical micro-CT phantoms have been designed and utilized for performance analysis. Also, important guidelines are suggested for future improvements.

GRANT INFORMATION

This work was supported by an NIH SIG grant (RR025667), an NSF MRI grant (CMMI0923297) as well as internal funding from ICTAS and SBES at Virginia Tech.

Dedication

To *Ma* and *Baba*.
Without their encouragement, I might never have begun working for my Ph.D.

And to *Lakshmi*.
Without her support, I might never have completed.

Acknowledgments

[As I write this hurriedly on a Sunday afternoon, with the ETD submission deadline looming in a few hours, I am sure that I will forget to acknowledge some people. My apologies in advance.]

Thanks are due to many people.

They say that life during Ph.D. is totally dependent on one's Ph.D. advisor. With that said, I was fortunate enough to have Dr Ge Wang as my Ph.D. advisor. Dr Wang is not only one of the most gifted researchers in the CT community, but more importantly, he is an excellent human being. And that made life during my Ph.D. one of the most wonderful years of my life.

Even though Dr Hengyong Yu was not a part of my Ph.D. committee, he was like a co-advisor to me. I was greatly helped by his technical guidance through e-mails / teleconferences, and manuscript reviews.

Dr Christopher Wyatt was like the second (unofficial) co-advisor for my Ph.D. Whenever I strayed too far from the broader aims of my thesis, he helped focus my attentions back to the task at hand. And the fact that he was strict about submission deadlines actually helped me complete my Ph.D. degree done on time.

I knew Dr Claudio da Silva even before I joined Dr Ge Wang's lab. I am grateful that he always took out time from his busy schedule to help with much needed advice and guidance.

It was also a privilege to have interacted with Dr Shuhai Xiao and Dr Nicholas Polys, each great scientists in their respective fields. They were always extremely encouraging about my research, and this really helped me a lot (especially in the initial years).

Thanks are also due to Dr Amy Bell – it was her confidence in my abilities that helped me clear the admissions hurdle at Virginia Tech. She also gave me invaluable lessons by walking me through the writing of my first research paper.

While working in Dr Ge Wang's lab from 2009 to 2013, I was able to interact with many wonderful colleagues, researchers and Professors – Xin Jin, James Bennett, Haiou Shen, Sourav Mishra, Deepak Bharkhada, Alexander Cong, Dr Wenxiang Cong, Dr Guohua Cao, Omid Ghasemalizadeh, Hao Gao, Baodong Liu, Chuang Miao, Peng He, Cody Edgell, Matthew

Ruder, Dr Fenglin Liu, Peng Feng.

Also my internship and collaboration with Xradia gave me the opportunity to learn from some of the greatest researchers in x-ray microscopy – Michael Feser, Christian Holzner, Tom Case.

During my summer internship at GE Healthcare, I learned a lot about problem solving in CT thanks to the mentorship of Debashish Pal, and guidance of other leading scientists like Brian Nett, Guangzhi Cao, Jiang Hsieh.

Collaborations with various researchers in Virginia Tech and outside allowed me to expand my research capabilities in CT and in different research domains. I am grateful to have worked with Bireswar Laha, Shree Narayanan, Dragoş Vasilescu, Abhilash Kizhakke Puliyakote, Dong Wang, Masoud Agah, Linbing Wang, Spencer Lee.

Great friends in the department made going to lab something worth looking forward to. I fondly remember many '*adda*' sessions in the BMES break room with Abhijit Gurjarpadhye, Gaurav Jain, Satyavrata Samavedi, Prasad Vaidya, Saugata Sarkar. And during my years at Torgersen Hall, with Aparna Mahadevan, Cunhao Gao, Canming Jiang, Ju.

Life outside lab was what kept me going through the many years of the Ph.D. I will always remember my Blacksburg friends as my first family in the USA. First and foremost, Arnab Gupta (my room-mate of first three years at Blacksburg) has been a great support. Thanks are also due to Puranjoy Bhattacharjee, Andrea L'Afflito, Bireswar Laha, Abhijit Sarkar, Manidipa Basu, Manjushree Palit. And the many others who touched my life in the 'Burg (surely I will miss many names here) – Suchismita Bhattacharjee, Tannistha Maiti, Balachandar Guduri, Sharmistha Mitra, Riya Sarker, Reina Kogenamaru, Poulomi Laha, Shreya Mitra, Souvik Pal.

Amma, Mahesh Anna, Padma, Peri-amma, Rajesh Anna have been such a great support. I am extremely lucky to have such wonderful in-laws. I am sure Appa would have been proud of my achievement, and that he still guides us in our daily lives.

If I had to pick out one thing as my happiest experience at Virginia Tech, it would be falling in love and marrying Lakshmi Dharmarajan. My school friends Soumallya Sengupta and Nilay Chandra would say that it was destined to be, but I remain ever thankful to the Virginia Tech Admissions Committee! Lakshmi's innate energy and positivity has helped me bring a new revitalized outlook not just to my life, but also to my research work.

And finally, the greatest debt lies to the two people who helped shape my life during my formative years, who encouraged me to go to USA and pursue a Ph.D. degree, and who stuck with me from day one of my Ph.D. to the very end. Ma and Baba – "*tumhara beta 'Doctor' ban gaya!*".

Contents

1 Introduction **1**

1.1 Micro-CT . . . 1

1.1.1 Micro-CT scanner components . . . 2

1.1.2 Imaging capability . . . 3

1.2 Image reconstruction algorithms . . . 4

1.2.1 Filtered back projection . . . 6

1.2.2 FBP and imaging capability . . . 6

1.2.3 Iterative reconstruction . . . 7

1.3 Compressed sensing based image reconstruction . . . 9

1.3.1 Gap between algorithmic advances and practice . . . 10

1.4 Contributions of this work (and thesis outline) . . . 10

Bibliography . . . 16

2 Experimental results on few-view micro-CT **17**

2.1 Abstract . . . 18

2.2 Introduction . . . 18

2.3 Micro-CT 3D Phantom . . . 20

2.3.1 Motivation . . . 20

2.3.2 Fabrication . . . 21

2.4 Numerical Tests and Micro-CT Samples . . . 21

2.4.1 Tests on Shepp-Logan Phantom . . . 22

2.4.2 Micro-CT Scans . . . 22
2.5 Image Reconstruction . . . 24
2.5.1 Filtered Back Projection . . . 24
2.5.2 Iterative Reconstruction . . . 25
2.5.3 Image quality metrics . . . 27
2.6 Results . . . 30
2.6.1 Simulations on Shepp-Logan Phantom . . . 30
2.6.2 Results on 3D micro-CT phantom . . . 33
2.6.3 Results on asphalt mastic . . . 33
2.7 Conclusions and Discussion . . . 33
2.8 Acknowledgments . . . 37
2.9 Appendix: Details of Image Reconstruction . . . 37
Bibliography . . . 44

3 Scout-view assisted interior micro-CT 45
3.1 Abstract . . . 46
3.2 Introduction . . . 46
3.3 Materials and Methods . . . 49
3.3.1 Micro-CT scanner . . . 49
3.3.2 Micro-CT phantoms and samples . . . 49
3.3.3 Scan protocols . . . 51
3.3.4 Interior reconstruction algorithms . . . 55
3.4 Results . . . 58
3.4.1 Results: Interior micro-CT phantom I . . . 58
3.4.2 Results: Interior micro-CT phantom II . . . 61
3.4.3 Results: Rock sample . . . 63
3.4.4 Results: Mouse lung . . . 64
3.5 Conclusion and discussion . . . 66
3.6 Acknowledgments . . . 67

Bibliography . . . 72

4 Interior micro-CT with an offset detector array **73**

4.1 Abstract . . . 74

4.2 Introduction . . . 74

4.3 Methods . . . 76

4.3.1 Interior tomography with an offset detector array . . . 76

4.3.2 Numerical simulations . . . 76

4.3.3 Experimental setup . . . 78

4.3.4 Reconstruction algorithms . . . 80

4.3.5 Image quality analysis . . . 86

4.4 Results . . . 86

4.4.1 Results: numerical simulations . . . 86

4.4.2 Experimental results . . . 91

4.4.3 Comments on method III . . . 94

4.5 Conclusions and Discussion . . . 96

Bibliography . . . 101

5 Conclusion **102**

5.1 Contributions of this work . . . 102

5.2 Future research directions . . . 103

Bibliography . . . 106

A Other related work carried out during dissertation **107**

Bibliography . . . 111

B Program parameters **112**

B.1 Few-view micro-CT . . . 112

B.1.1 Fan-beam FBP . . . 112

B.1.2 SART-TV . . . 113

B.2 Scout-view assisted interior micro-CT 113
B.2.1 Truncated-FBP 113
B.2.2 SS-SART-TV 114
B.2.3 Scout interpolation 114
B.2.4 Scout-reconstruction 114
B.3 Interior micro-CT with an offset detector array 115
B.3.1 Method I: Pre-convolution weighting 116
B.3.2 Method II: Post-convolution weighting 116
B.3.3 Method III: Iterative reconstruction 116

C Publication information **117**

List of Figures

1.1 Various biological applications of micro-CT scanners 2
1.2 Various components of a micro-CT scanner 3
1.3 Interior tomography (exact, instead of approximate, local reconstruction) . . 4
1.4 Geometry of a CT scan 5
1.5 Discrete representation of CT scan geometry 7

2.1 The 3D micro-CT phantom 22
2.2 Noise and resolution measurement in reconstructed images 27
2.3 Procedure for calculating sharpness parameter 29
2.4 Few-view reconstruction at different noise levels 31
2.5 Reconstruction metrics for the Shepp-Logan phantom 32
2.6 Few view reconstruction on the 3D micro-CT phantom 34
2.7 Reconstruction metrics for the 3D micro-CT phantom 35
2.8 Few view reconstruction on asphalt dataset 36
2.9 Imaging model for few-view reconstruction 38

3.1 Samples used in characterizing interior micro-CT 50
3.2 Sinograms demonstrating steps in interior reconstruction 53
3.3 Two configurations of high-resolution interior projections 54
3.4 Graphic depicting scout-reconstruction method of Sec. 3.3.4 57
3.5 Line profiles for interior reconstruction algorithms 59
3.6 Relative root mean square error (RRME) for interior reconstruction 60

3.7 Interior reconstruction results of interior micro-CT phantom II 62
3.8 Results on rock sample 63
3.9 Tomographic reconstruction of mouse lung sample 65

4.1 Interior tomography with offset detector array 77
4.2 Micro-CT system components 79
4.3 Micro-CT phantom fabrication 80
4.4 Steps in image reconstruction algorithms 82
4.5 Reconstructed images for numerical simulations 87
4.6 Difference of reconstructed image w.r.t. effective-ROI reconstruction 88
4.7 Line profiles for numerical simulations 88
4.8 Plots of reconstruction error in numerical simulation 90
4.9 Reconstruction of micro-CT phantom by method I 91
4.10 Reconstruction of micro-CT phantom by method II 92
4.11 Reconstruction of micro-CT phantom by method III 93
4.12 Central ROI for three reconstruction methods 94
4.13 Effect of projection completion 95

A.1 Steps in matching of nano-CT and micro-CT images 108
A.2 Training and education, and volume visualization 109

List of Tables

2.1 Scan settings for study on few-view reconstruction 23
2.2 Projection noise levels in numerical simulations 23

3.1 Scan settings for study on scout-view assisted interior tomography 52
3.2 Algorithm run-times 67

4.1 Scan settings for offset detector study 81

Chapter 1

Introduction

Thesis Statement
Compressed-sensing based reconstruction methods
can enhance the imaging capability of micro-CT scanners.

1.1 Micro-CT

Computed tomography (CT) scanners are most widely known for their use in the medical field. However CT scanners are also used to perform non-destructive imaging in a variety of other applications e.g. cargo and vehicle inspection [15], airport luggage screening [14], preclinical research with mouse models [27], non-destructive evaluation and fault-finding in semiconductor fabrication [10], imaging of internal cellular structures within tissue samples [1], etc. In all these scans, the imaging resolution is different – a trailer-truck may be imaged at resolution of a few cm and be able to reveal sufficient detail of the target material, while a study of internal cellular structures requires a resolution of 50 - 100 nm. An increasingly important piece of the resolution spectrum is taken up by the domain of micro-CT (resolution: 1 μm to $\sim$100 μm). The domain of micro-CT can be further divided into two sub-domains – conventional/traditional micro-CT (resolution: 50 - 100 μm) [37] and high-end or high-resolution micro-CT (resolution: 1 - 20 μm) [10]. The current study focuses on high-resolution micro-CT scanners. However some of the results in the study may be extended to conventional micro-CT, industrial CT etc.

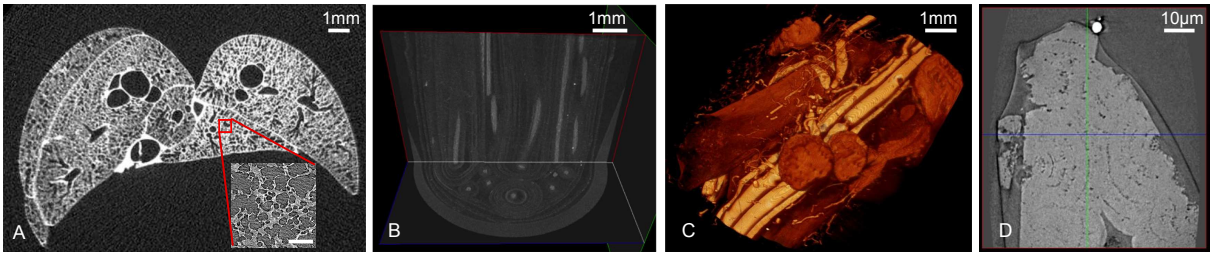

Figure 1.1: Various biological applications of micro-CT scanners. (A) Mouse lung reconstructed slice (0.5x objective of MicroXCT, 13.1 μm voxel); Inset (scale bar: 200 μm): interior region of interest (ROI) imaged at 10x, 2.04 μm voxel. (B) Osteon mimicking scaffold multi-planar view (4x MicroXCT, 5.0 μm voxel). (C) Mouse limb volume rendering of bones and vasculature (4x MicroXCT, 4.3 μm voxel). (D) Nano-CT scan of a microfossil reconstructed slice (phase-contrast mode NanoXCT, 64 nm voxel); the ROI for this scan was selected by a primary scan on a micro-CT scanner.

The first micro-CT systems were built in the 1980-s [37] and used synchrotron radiation sources. A synchrotron may produce a monochromatic x-ray beam at a very high flux rate. These are ideal conditions for x-ray imaging – (1) the high flux assures high quality imaging in a very short time, and (2) the single frequency allows the formulation of a truly linear imaging model. Unfortunately, synchrotron sources are not easily available for usage by a vast population of researchers / users. Also synchrotrons are immensely expensive to build and maintain. As a more accessible alternative, micro-CT scanners have been developed by using in-house x-ray sources. Their sizes may vary between desktop versions [30] to those that are a couple of meters wide [10]. Such micro-CT scanners are increasingly being used in universities, research organizations and industries for a variety of purposes e.g. semiconductor fabrication [10], transportation engineering [42], preclinical cancer research [27], evolutionary studies [31], regenerative medicine [33], lung morphology studies [41] etc. Figure 1.1 depicts a few biological applications of micro-CT scanners.

1.1.1 Micro-CT scanner components

The typical components of a micro-CT scanner are shown in Fig. 1.2 [21]. X-rays generated by an x-ray source pass through a sample placed on the sample stage. The x-rays then reach the detector that is comprised of a scintillator, optical lens, and a CCD (see Fig. 4.3a in [37]). The x-rays are absorbed by the scintillator and converted to visible light; the lens magnifies the visible light onto the CCD. Different magnification objectives are available, allowing the imaging resolution to be modified. Furthermore, the geometric magnification of the system is dependent on the source to object distance a and the object to detector distance b according to the relation [10]:

$$M = \frac{a+b}{a} \tag{1.1}$$

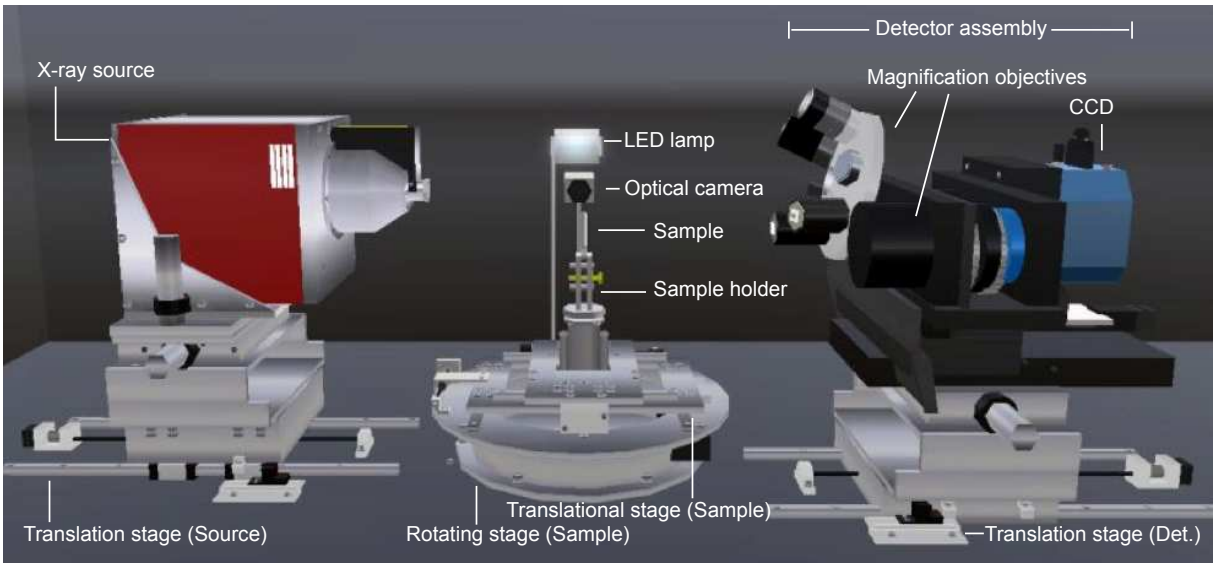

Figure 1.2: Various components of a micro-CT scanner.

In the micro-CT system, the geometrical magnification may be modified by translating the source and detector stages according to the needs of the sample. The sample can also be translated in the x-y-z directions. The above arrangement is specific to the Xradia MicroXCT-400 scanner (Xradia Inc., CA). Though all commercial micro-CT scanners have unique design traits [37], many of the components and/or capabilities are similar.

1.1.2 Imaging capability

Imaging capability of micro-CT scanners is a broad term, and relates to many aspects of the scanning process e.g. the ability to image a wide variety of samples, scanning speed, image resolution, reconstruction noise etc. This work focuses on 2 aspects of capability:

i. **Total scan time**: Tomographic acquisition times on the scanners are quite high, ranging anywhere from 30 minutes to $>$ 6 hours [10, 20, 32]. Longer scans are especially problematic in applications where many samples have to be scanned, as part of a research study, or in a routine process like failure analysis. Also, tomography data-sets are usually stored in uncompressed formats and their sizes range anywhere from 1–15 GB. Even though high-capacity memory disks are relatively inexpensive these days, any reduction in number of views (especially if the reduction factor is > 2) can have significant impact on digital storage costs and manageability.

ii. **Allowable sample size**: One major limitation of computed tomography has been that the x-ray beam needs to cover the entire sample as in Fig. 1.3a. If the beam does not cover the entire object boundary (also called object support) as shown in Fig. 1.3b, this

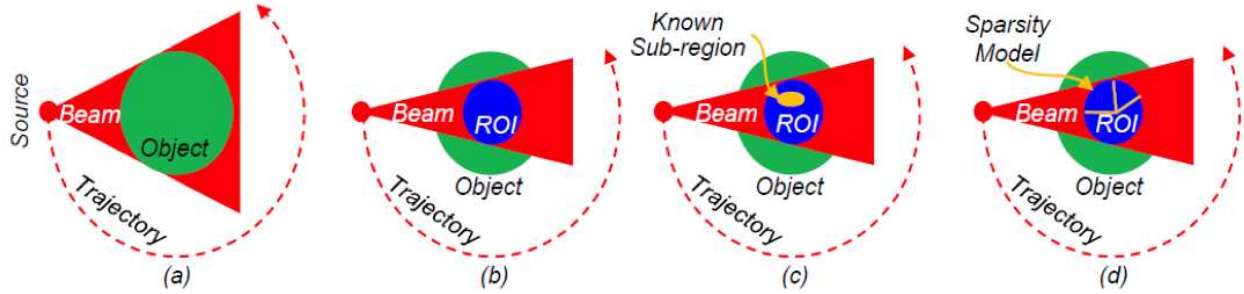

Figure 1.3: Interior tomography (exact, instead of approximate, local reconstruction). (a) Conventional tomography allows exact reconstruction of an object from a half-scan; (b) it was considered impossible to uniquely reconstruct an ROI from truncated local data, which is known as the interior problem; (c) it was proven in 2007 that the interior problem can be exactly and stably solved assuming a known sub-region; and (d) it was established in 2009 that based on a piecewise polynomial ROI model the interior problem can be uniquely solved.

leads to truncated projections. It has been proven that for truncated projections, there is no unique value for reconstruction (this is called the 'interior tomography' problem) [23]. In high resolution micro-CT, x-ray beam is narrow and field-of-view (FOV) varies between 0.5 mm and 1 cm, with higher resolution at lower FOV-s [37, 10]. Many objects of interest are larger than the x-ray beam, and this places a major restriction on developing new applications. One approach is to cut the sample to a portion of interest that fits within FOV. However this is not possible in many cases, or may significantly alter sample integrity. Another approach is to go on acquiring truncated projection sinograms (the term 'sinogram' denotes a projection data-set), and artificially extend the sinogram before reconstruction [5]. While this provides images comparable to global reconstruction in certain cases (e.g. homogeneous samples), artifacts may arise in specimens with complex anisotropic features, or greater mass outside the region-of-interest (ROI) [37, 5].

1.2 Image reconstruction algorithms

To model the x-ray projection process, a point source is assumed as shown in Fig. 1.4A. A single x-ray (the direction of the ray being along an arbitrary s axis) with an initial number of photons N_i impinges upon the imaged object and the number of photons after passing through the object is reduced to N_o. The intersection of the x-ray with the object boundary is at points $s = a$ and $s = b$. If $f(s)$ is the attenuation coefficient along the x-ray direction,

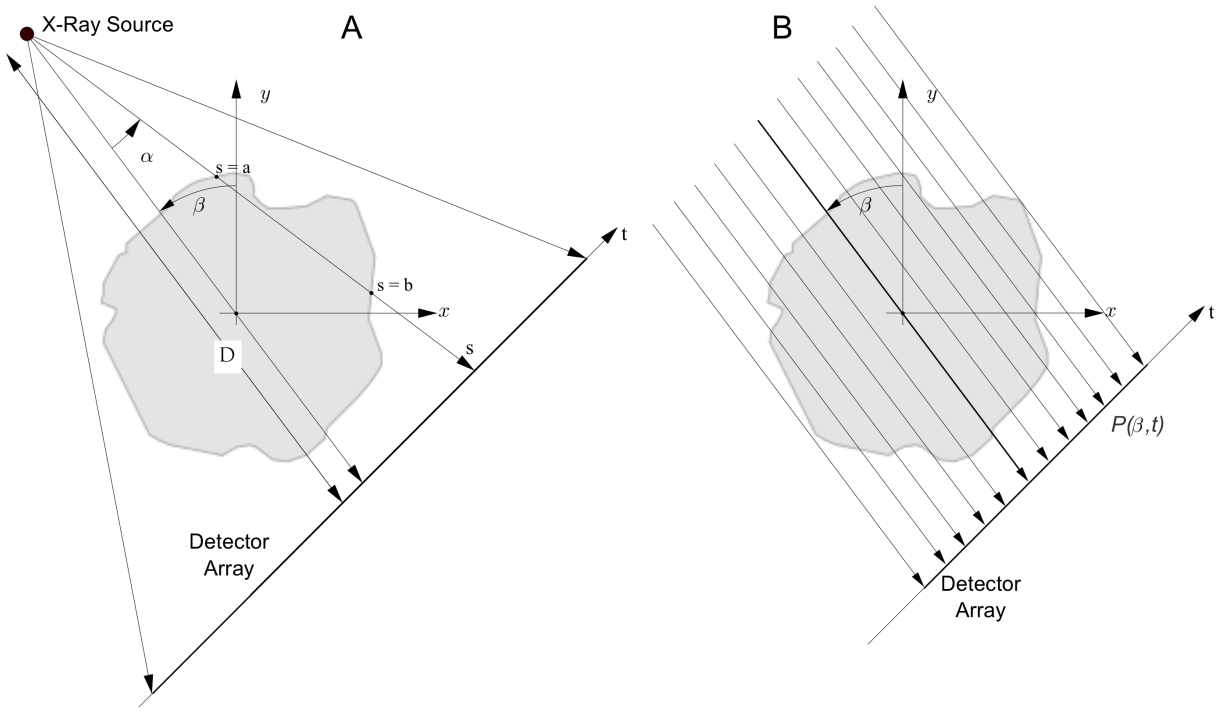

Figure 1.4: Geometry of a CT scan. (A) Fan-beam geometry. (B) Parallel-beam geometry

then the attenuation is related to the photon counts by:

$$N_o = N_i \exp^{-\int_a^b f(s)\,ds} \tag{1.2}$$

By taking logarithm on both sides, the above equation yields a linear form (and the projection value P):

$$P = -\log\left(\frac{N_o}{N_i}\right) = \int_a^b f(s)\,ds \tag{1.3}$$

Now we extend the object to two dimensions along the x-y directions i.e. the attenuation map of the object is $f(x, y)$, and the projection value $P(\beta, t)$ is known for various projection angles β and the spatial location t within each projection. (If the angular location within each projection is measured as α, the projections are labeled as $P(\beta, \alpha)$.) The reconstruction problem deals with determination of the unknown $f(x, y)$ from the measured values $P(\beta, t)$ or $(P(\beta, \alpha))$.

1.2.1 Filtered back projection

Filtered back projection(FBP) is the most popular reconstruction algorithm of choice [26]. The formula for filtered back-projection for x-ray tomography acquired in parallel beam geometry is given by [16]:

$$f(x,y) = \int_0^{\pi} \left[\int_{-\infty}^{\infty} P(\beta, t')\, p(t - t')\, dt' \right] d\beta \tag{1.4}$$

where the variables β, t are defined according to Fig. 1.4B. $P(\beta, t)$ denotes the measured parallel beam projections, and $f(x,y)$ is the unknown object attenuation map. The inner integral denotes a convolution where $p(t)$ is the inverse Fourier transform of the ramp function $|w|$ in the frequency domain. The convolution kernel $p(t)$ is known as the ramp filter (or the Ram-Lak filter).

Eq. 1.4 may be modified according to the needs of the scanning geometry [14, 16, 55], source trajectory [3] etc. For example, reconstruction algorithms in commercial micro-CT scanners are extensions of the FBP reconstruction formula [45]. In this study, the fan-beam FBP reconstruction algorithm was modified to handle short-scan acquisition and center shifted geometry. The details of the modified algorithm are provided in Ch. 2 (Appendix 2.9).

1.2.2 FBP and imaging capability

The following important observations may be made about Eq. 1.4:

A. The outer integral is over the continuous range $[0, \pi]$. In the discrete implementation of this formula, sufficient angular sampling must be maintained to prevent aliasing artifacts [14, Ch. 7].

B. The inner integral is a convolution that must be calculated over $-\infty$ and ∞. In reality, the projections $P(\beta, t)$ are usually bounded within a range of t i.e. $P(\beta, t) = 0, \forall t \notin [t_i, t_f]$. Thus, to evaluate Eq. 1.4 accurately, complete information$P(\beta, t)$ within the range $t \in [t_i, t_f]$ is required.

C. This formula does not account for the presence of measurement noise in the projections. Convolution with $p(t)$ is equivalent to multiplying the Fourier transform of a projection with the ramp function $|w|$. Thus, high-frequency noise may be greatly amplified by the ramp filter. To suppress the noise amplification, a low-pass filter like a Hanning window [16] is usually applied during ramp filtering. However, this has the disadvantage that some of the original high-frequency information in the measured projections is lost (thus leading to lower image resolution in the reconstructed slices).

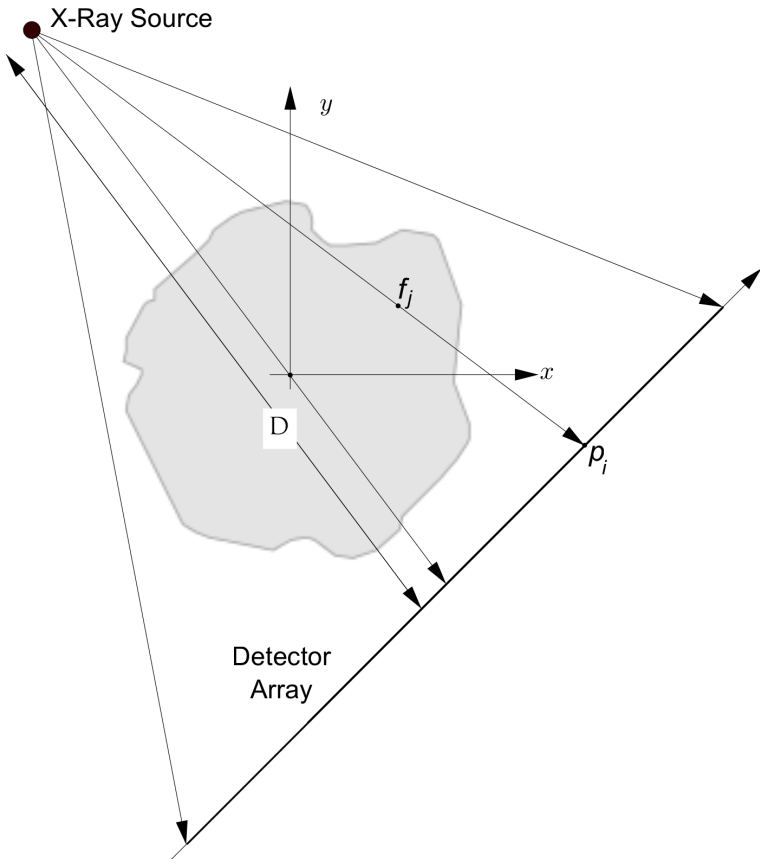

Figure 1.5: Discrete representation of CT scan geometry.

The above observations about the FBP algorithm directly affect the imaging capability of micro-CT scanners (Sec. 1.1.2). For example, the total scan time may be reduced by acquiring lesser number of projections in a tomography. However observation A above requires that the angular sampling be sufficiently high so as to maintain high reconstruction quality. Secondly, micro-CT samples are routinely larger than the FOV. Yet the condition for convolution (observation B above) requires that the projections be measured over the entire object support. Thus, FBP places severe restriction on the imaging capability of micro-CT scanners.

1.2.3 Iterative reconstruction

In Fig. 1.4A, the acquisition parameters, projection values and object attenuation map were all represented as continuous variables. By considering a discretized notation, the geometry of a CT scan may be represented as in Fig. 1.5. The object attenuation map may be represented by a discrete image grid where the pixels are represented by the set

f_j, $j = 1, 2, \ldots N$. The projection values at any projection angle are represented by the set p_i, $i = 1, 2, \ldots M$ (here, M is the sum of all detector pixels for all projection angles). The relationship between f_j's and p_i's may be represented as in [16]:

$$\sum_{j=1}^{N} w_{ij} f_j = p_i, \qquad i = 1, 2, \ldots M \tag{1.5}$$

where w_{ij} is the weighting factor that represents the contribution of the jth cell (pixel) to the ith ray integral.

If we denote all the rays in all projections by the vector $\mathbf{p}$, and all the image pixels by the vector $\mathbf{f}$ we get the following equation for the complete imaging system:

$$\mathbf{W}\ \mathbf{f} = \mathbf{p} \tag{1.6}$$

One solution to Eq. 1.6 is direct matrix inversion:

$$\mathbf{f} = \mathbf{W}^{-1}\mathbf{p}, \quad \text{W is a square matrix} \tag{1.7}$$

$$\mathbf{f} = \left(\mathbf{W}^T\mathbf{W}\right)^{-1}\mathbf{W}^T\mathbf{p}, \quad \text{W is not a square matrix} \tag{1.8}$$

However the matrix W is extremely large and it is computationally inefficient to calculate the inverse of this matrix. Iterative reconstruction (IR) algorithms have been developed to solve Eq. 1.6 e.g. algebraic reconstruction technique (ART), simultaneous iterative reconstruction technique (SIRT), simultaneous ART (SART) etc [16, 44, 55]. As an example, the SART algorithm is described here. Starting with an arbitrary image matrix $f^{(0)}$, the image matrix is updated at each iteration by:

$$f_j^{(k+1)} = f_j^{(k)} + \lambda^{(k)} \frac{\displaystyle\sum_{i \in P(\beta')} \left[\frac{w_{ij}\left(p_i - \mathbf{W}_i \mathbf{f}^{(k)}\right)}{\displaystyle\sum_{j=1}^{N} w_{ij}} \right]}{\displaystyle\sum_{i \in P(\beta')} w_{ij}} \tag{1.9}$$

where $i \in P(\beta')$ denotes that summation is carried out over the detector pixels at projection angle β'. $\lambda^{(k)}$ is the relaxation factor at iteration k, and $\mathbf{W}_i\mathbf{f}^{(k)}$ is the forward projected estimate at detector location i.

IR algorithms have an advantage over FBP in that they do not have same restrictions as FBP (those listed in Sec. 1.2.1). Yet, IR techniques have some of their own disadvantages:

- **Computational load**: IR techniques require multiple iterations of forward- and back-projection, each of which are extremely computationally intensive. In the past, such computational load has been very inconvenient to handle. FBP consists of one back-projection step, and one filtering step, and is much less computationally demanding.
- **Noise performance**: The result of IR techniques may be too noisy unless some special noise-handling is introduced. Special noise-handling techniques used in the past included ordered subset SART [44], non-linear filtering [46, 50] etc.

1.3 Compressed sensing based image reconstruction

We rewrite Eq. 1.6, this time along with the dimensions of the relevant matrices:

$$\underbrace{\mathbf{W}}_{M\times N}\ \underbrace{\mathbf{f}}_{N\times 1} = \underbrace{\mathbf{p}}_{M\times 1}, \qquad \mathbf{f} = ? \tag{1.10}$$

It was traditionally known that the above equation has a unique solution for the unknown $\mathbf{f}$ only when $M \geq N$ (i.e. the number of measurements is greater than the number of unknowns). Then, in 2006, the signal processing community experienced a major shift with the introduction of compressed sensing (CS) theory [6, 9]. It was shown that under certain assumptions, unknowns could be accurately recovered with far fewer samples than earlier considered necessary. If the unknown $\mathbf{f}$ was sparse in a transform domain ψ, Eq. 1.10 may be solved even if $M < N$. The solution was achieved by a non-linear reconstruction

$$\min_{\mathbf{f}^*} \|\psi \mathbf{f}^*\|_{l_1}, \quad \text{subject to} \mathbf{W}\mathbf{f}^* = \mathbf{p} \tag{1.11}$$

where $\|.\|_{l_1}$ is the **l-1** norm [6].

The CS theory had vast implications to a variety of disciplines including the field of image reconstruction. Very soon after the introduction of CS, several groups reported the ability to reconstruct CT images using far lower data-set sizes than required by traditional FBP algorithm [34, 35, 53, 38]. CS-based iterative techniques were demonstrated to reduce x-ray dose and scan time (simultaneously increasing temporal resolution) [2, 24, 36].

In 2007, it was proven that the interior problem could be exactly solved if sub-region in an ROI was exactly known [51, 8, 17, 52] (this discovery was not based on the CS theory). Yet, precise knowledge of sub-region within an ROI is difficult to obtain. Again, using CS theory, exact interior reconstruction was achieved under the assumption that imaged object was piecewise constant or piecewise polynomial [53]. It turns out that the piecewise polynomial assumption holds true for many real cases, and CS-based reconstruction methods were found to achieve high quality interior reconstruction in real applications [48].

The implementation of the non-linear reconstruction process described by Eq. 1.11 is an iterative technique. We explain below how the two disadvantages of iterative reconstruction

techniques listed in Sec. 1.2.3 (computational load, and noise performance) apply to CS theory and other recent developments.

- Concurrent with developments of CS theory and algorithmic advancements, there have been major advancements in the field of high performance computing using graphic processing units (GPU-s). These advancements enable the building of relatively inexpensive hardware systems that can handle the computational load of iterative reconstruction schemes [47, 49].
- It was observed that the noise performance improves when CS theory is incorporated into the iterative reconstruction framework [28, 36, 38, 53].

1.3.1 Gap between algorithmic advances and practice

Through the developments described above, image reconstruction researchers in the field of micro-CT were convinced that CS theory had the potential to enhance imaging capabilities (like scan time and sample size, see Sec. 1.1.2). Sadly enough, the algorithmic advances of recent years are rarely translated to the field and FBP remains the reconstruction algorithm of choice in almost all manufactured CT scanners [26]. The gap is attributable to many reasons, some of which are listed below:

i. proprietary nature of CT technology
ii. unavailability of corrected raw projection data-sets (since there are no DICOM like standards for CT data, data sharing is difficult)
iii. lack of easily adaptable (plug and play) image reconstruction software in the public domain
iv. familiarity of manufacturers/users with FBP and lack of immediate economic motivation to change.

1.4 Contributions of this work (and thesis outline)

The objective of this work is to illustrate that CS based reconstruction can enhance imaging capability in micro-CT scanners. In particular, the problems of lengthy scan times and constrained sample size were tackled by innovative reconstruction algorithms.

The specific achievements in this work are:

In **Chapter 2**, the CS-based reconstruction algorithms were extended for use with real micro-CT data. Next, through numerical simulations and tests on a novel micro-CT phantom, the performance of CS-based reconstruction methods were characterized vis-à-vis traditional

FBP methods. It was found that CS-based methods allowed high quality reconstruction by using only $1/8^{th}$ the number of views required by FBP.

Chapter 3 focuses on the reconstruction accuracy of interior reconstruction algorithms. In the past, multi-resolution acquisition methods have been developed that used a low-resolution global scan to achieve accurate reconstruction of an interior ROI [19, 22, 25, 29, 39]. However, previous methods placed restrictions on the scan geometry, or required a fully sampled low-resolution scan. In this Chapter, two new methods that achieve accurate interior reconstruction with just a handful of global projections (or scout views) are described . The first method is an extension of previous sinogram extrapolation methods [13], and works on specific geometries only. The second method is more flexible in terms of geometry, and combines CS based reconstruction with multi-resolution acquisition. Also, unlike previous studies that demonstrated interior reconstruction only with numerically truncated real global projections, this study used real data where global views and interior data were acquired in completely separate scans.

In **chapter 4**, techniques are described that allow the increase of the size of an interior ROI that can be covered by a fixed-size detector. Previously, it has been shown that the scan FOV may be increased by displacing (or offset-ing) the detector array [7, 43]. Yet, all previous studies made the assumption that the increased FOV covered the entire sample. In the field of micro-CT, that assumption may not hold true, but there would still be benefit in imaging a larger sized interior ROI. This chapter details three methods that achieve interior reconstruction with an offset detector array. The proposed methods extend previous analytic [7, 11, 18, 43, 54] and iterative reconstruction techniques [4, 12] to accommodate the special needs of the problem at hand. Numerical simulations illustrate the advantages / disadvantages of the proposed methods – a CS based reconstruction method is found to provide the highest accuracy. Finally, the methods are tested on real data acquired on an in-house micro-CT scanner.

Finally, **chapter 5** concludes this thesis with a discussion and future research directions.

The broader impact of this work is that algorithms were verified on data from real scanners, and thus help motivate real applications (and industrial adoption) of theoretical advancements. Also in accord with the reproducible research policy [40], software and data have been released into the public domain for aid of other researchers.

Bibliography

[1] Joy C Andrews, Eduardo Almeida, Marjolein C H van der Meulen, Joshua S Alwood, Chialing Lee, Yijin Liu, Jie Chen, Florian Meirer, Michael Feser, Jeff Gelb, Juana Rudati, Andrei Tkachuk, Wenbing Yun, and Piero Pianetta. Nanoscale X-ray microscopic imaging of mammalian mineralized tissue. *Microscopy and microanalysis : the official journal of Microscopy Society of America, Microbeam Analysis Society, Microscopical Society of Canada*, 16(3):327–36, June 2010.

[2] T M Benson and J Gregor. Three-dimensional focus of attention for iterative cone-beam micro-CT reconstruction. *Physics in medicine and biology*, 51(18):4533–46, September 2006.

[3] Deepak K Bharkhada. *Development of Novel Cardiac CT Methods*. PhD thesis, Wake Forest University, 2010.

[4] Junguo Bian, Jiong Wang, Xiao Han, Emil Y Sidky, Lingxiong Shao, and Xiaochuan Pan. Optimization-based image reconstruction from sparse-view data in offset-detector CBCT. *Physics in medicine and biology*, 58(2):205–30, January 2013.

[5] Anne Bilgot, Laurent Desbat, and Valerie Perrier. Filtered backprojection method and the interior problem in 2D tomography, 2009.

[6] E.J. Candès, Justin Romberg, and Terence Tao. Robust Uncertainty Principles : Exact Signal Reconstruction from Highly Incomplete Frequency Information. *Information Theory, IEEE Transactions on*, 52(2):489–509, 2006.

[7] Paul S Cho, Anthony D Rudd, and Roger H Johnson. Cone-beam CT from width-truncated projections. *Computerized medical imaging and graphics*, 20(1):49–57, 1996.

[8] M Courdurier, F Noo, M Defrise, and H Kudo. Solving the Interior Problem of Computed Tomography Using a Priori Knowledge. *Inverse problems*, 24(6):65001, September 2008.

[9] D.L. Donoho. Compressed sensing. *Information Theory, IEEE Transactions on*, 52(4):1289–1306, 2006.

[10] M Feser, J Gelb, H Chang, H Cui, F Duewer, S H Lau, A Tkachuk, and W Yun. Sub-micron resolution CT for failure analysis and process development. *Measurement Science and Technology*, 19(9):094001, September 2008.

[11] J Gregor, SS Gleason, and MJ Paulus. Conebeam x-ray computed tomography with an offset detector array. In *Image Processing, 2003. ICIP 2003. Proceedings. 2003 International Conference on*, volume 2, pages II–803, 2003.

[12] Eberhard Hansis, Jörg Bredno, David Sowards-Emmerd, and Lingxiong Shao. Iterative Reconstruction for Circular Cone-Beam CT with an Offset Flat-Panel Detector. In *Nuclear Science Symposium Conference Record (NSS/MIC), 2010 IEEE*, pages 2228–2231, 2010.

[13] Stefan Hoppe, Joachim Hornegger, Gunter Lauritsch, Frank Dennerlein, and Frederic Noo. Truncation correction for oblique filtering lines. *Medical Physics*, 35(12):5910, 2008.

[14] Jiang Hsieh. *Computed tomography: principles, design, artifacts, and recent advances*. SPIE Publications, 2003.

[15] James H Johnson and Paul Bjorkholm. Vehicle mounted inspection systems and methods, 2005.

[16] A.C. Kak and M. Slaney. *Principles of Computerized Tomographic Imaging*. Society of Industrial and Applied Mathematics, 2001.

[17] Hiroyuki Kudo, Matias Courdurier, Frédéric Noo, and Michel Defrise. Tiny a priori knowledge solves the interior problem in computed tomography. *Physics in medicine and biology*, 53(9):2207–31, May 2008.

[18] Vinson Liu, Nicholas R. Lariviere, and Ge Wang. X-ray micro-CT with a displaced detector array: Application to helical cone-beam reconstruction. *Medical Physics*, 30(10):2758, 2003.

[19] Clemens Maaß, Michael Knaup, and Marc Kachelrieß. New approaches to region of interest computed tomography. *Medical Physics*, 38(6):2868, 2011.

[20] Brian D Metscher. MicroCT for comparative morphology: simple staining methods allow high-contrast 3D imaging of diverse non-mineralized animal tissues. *BMC physiology*, 9:11, January 2009.

[21] S. Mishra, Kriti Sen Sharma, S. J. Lee, E. A. Fox, and G. Wang. SLATE: Virtualizing multiscale CT training. *Journal of X-ray Science and Technology*, 20(3):383, 2012.

[22] O. Nalcioglu, ZH Cho, and RY Lou. Limited Field of View Reconstruction in Computerized Tomography. *Nuclear Science, IEEE Transactions on*, 26(1):546–551, 1979.

[23] Frank Natterer. *The mathematics of computerized tomography*. SIAM, 2001.

[24] Brian E Nett, Robert Brauweiler, Willi Kalender, Howard Rowley, and Guang-Hong Chen. Perfusion measurements by micro-CT using prior image constrained compressed sensing (PICCS): initial phantom results. *Physics in medicine and biology*, 55(8):2333–50, April 2010.

[25] D. Pak-Kong Lun and T.C. Hsung. Region-of-interest tomography using multiresolution interpolation. In *Acoustics, Speech, and Signal Processing, 1997. ICASSP-97., 1997 IEEE International Conference on*, pages 2825–2828, 1997.

[26] Xiaochuan Pan, Emil Y Sidky, and Michael Vannier. Why do commercial CT scanners still employ traditional, filtered back-projection for image reconstruction? *Inverse problems*, 25(12):1230009, January 2009.

[27] M J Paulus, S S Gleason, S J Kennel, P R Hunsicker, and D K Johnson. High resolution X-ray computed tomography: an emerging tool for small animal cancer research. *Neoplasia (New York, N.Y.)*, 2(1-2):62–70, 2008.

[28] Ludwig Ritschl, Frank Bergner, Christof Fleischmann, and Marc Kachelriess. Improved total variation-based CT image reconstruction applied to clinical data. *Physics in medicine and biology*, 56(6):1545–61, March 2011.

[29] B Sahiner and a E Yagle. Region-of-interest tomography using exponential radial sampling. *IEEE transactions on image processing : a publication of the IEEE Signal Processing Society*, 4(8):1120–7, January 1995.

[30] Alexander Sasov. Desktop x-ray micro-CT instruments. *Developments in X-Ray Tomography III. Edited by Bonse, Ulrich. Proceedings of the SPIE*, 4503(282–290), 2002.

[31] J. D. Schiffbauer, S. Xiao, Kriti Sen Sharma, and G. Wang. The origin of intracellular structures in Ediacaran metazoan embryos. *Geology*, 40(3):223–226, January 2012.

[32] James D Schiffbauer, Shuhai Xiao, Kriti Sen Sharma, and Ge Wang. The origin of intracellular structures in Ediacaran metazoan embryos. *Geology (in press)*, 2012.

[33] Kriti Sen Sharma, T Andric, L D Wright, J W Freeman, C L Wyatts, and G Wang. Micro-CT for osteon-like scaffolds. In *11th Annual Conference of the North Carolina Tissue Engineering and Regenerative Medicine Society*, Winston-Salem, NC, 2009.

[34] Emil Y Sidky, Chien-min Kao, and Xiaochuan Pan. Accurate image reconstruction from few-views and limited-angle data in divergent-beam CT. *Journal of X-Ray Science and Technology*, 14:119–139, 2006.

[35] Emil Y Sidky and Xiaochuan Pan. Image reconstruction in circular cone-beam computed tomography by constrained, total-variation minimization. *Physics in medicine and biology*, 53(17):4777–807, September 2008.

[36] Jiayu Song, Qing H. Liu, G. Allan Johnson, and Cristian T. Badea. Sparseness prior based iterative image reconstruction for retrospectively gated cardiac micro-CT. *Medical Physics*, 34(11):4476–4483, July 2007.

[37] Stuart R. Stock. *MicroComputed Tomography: Methodology and Applications*. CRC Press, 2008.

[38] Jie Tang, Brian E Nett, and Guang-Hong Chen. Performance comparison between total variation (TV)-based compressed sensing and statistical iterative reconstruction algorithms. *Physics in medicine and biology*, 54(19):5781–804, October 2009.

[39] G. Tisson, P. Scheunders, and D. Van Dyck. 3D region of interest x-ray CT for geometric magnification from multiresolution acquisitions. In *2004 2nd IEEE International Symposium on Biomedical Imaging: Macro to Nano (IEEE Cat No. 04EX821)*, volume 2, pages 567–570. Ieee, 2004.

[40] Patrick Vandewalle, Jelena Kovacevic, and Martin Vetterli. Reproducible research in signal processing. *IEEE Signal Processing Magazine*, 26(3):37–47, May 2009.

[41] Dragos M Vasilescu, Zhiyun Gao, Punam K Saha, Leilei Yin, Ge Wang, Beatrice Haefeli-Bleuer, Matthias Ochs, Ewald R Weibel, and Eric a Hoffman. Assessment of morphometry of pulmonary acini in mouse lungs by nondestructive imaging using multiscale microcomputed tomography. *Proceedings of the National Academy of Sciences of the United States of America*, 109(42):17105–10, October 2012.

[42] Dong Wang. *A micro-scale method to associate the fatigue properties of asphalt binder, mastic and mixture*. PhD thesis, Virginia Polytechnic Institute and State University, 2011.

[43] Ge Wang. X-ray micro-CT with a displaced detector array. *Medical Physics*, 29(7):1634, 2002.

[44] Ge Wang and Ming Jiang. Ordered-subset simultaneous algebraic reconstruction techniques (OS-SART). *Journal of X-ray Science and Technology*, 12:169–177, 2004.

[45] Ge Wang, Tein-Hsiang Lin, Ping-chin Cheng, and Douglas M. Shinozaki. A General Cone-Beam Reconstruction Algorithm. *Ieee Transactions on Medical Imaging*, 12(3):486–496, 1993.

[46] Jing Wang, Tianfang Li, and Lei Xing. Iterative image reconstruction for CBCT using edge-preserving prior. *Medical Physics*, 36(1):252, 2009.

[47] Fang Xu and Klaus Mueller. Real-time 3D computed tomographic reconstruction using commodity graphics hardware. *Physics in medicine and biology*, 52(12):3405–19, June 2007.

[48] Qiong Xu, Xuanqin Mou, Ge Wang, Jered Sieren, Eric a Hoffman, and Hengyong Yu. Statistical interior tomography. *IEEE transactions on medical imaging*, 30(5):1116–28, May 2011.

[49] Wei Xu and Klaus Mueller. A Performance-Driven Study of Regularization Methods for GPU-Accelerated Iterative CT. In *2nd High Performance Image Reconstruction Workshop*, Beijing, China, 2009.

[50] Wei Xu and Klaus Mueller. Evaluating popular non-linear image processing filters for their use in regularized iterative CT. In *Nuclear Science Symposium Conference Record (NSS/MIC), 2010 IEEE*, pages 2864—-2865. IEEE, 2010.

[51] Yangbo Ye, Hengyong Yu, and Ge Wang. Exact interior reconstruction with cone-beam CT. *International journal of biomedical imaging*, 2007(1):10693, January 2007.

[52] Yangbo Ye, Hengyong Yu, and Ge Wang. Exact interior reconstruction from truncated limited-angle projection data. *International journal of biomedical imaging*, 2008:427989, January 2008.

[53] H Yu and G Wang. Compressed sensing based interior tomography. *Physics in medicine and biology*, 54(9):p2791–2805, 2009.

[54] Lifeng Yu, Charles Pelizzari, and Xiaochuan Pan. Application of asymmetric cone-beam CT in radiotherapy. In *Nuclear Science Symposium Conference Record, 2004 IEEE*, volume 5, pages 3249—-3252, 2004.

[55] G.L. Zeng. *Medical Image Reconstruction: A Conceptual Tutorial*. Springer, 2010.

Chapter 2

Experimental results on few-view micro-CT

Publication information

The contents of this chapter were published as:
Kriti Sen Sharma, Xin Jin, Christian Holzner, Shree Narayanan, Baodong Liu, Dong Wang, Masoud Agah, Linbing Wang, Hengyong Yu, Ge Wang,"Experimental Studies on Few-view Reconstruction for High-resolution micro-CT", *Journal of X-ray Science and Technology*, 21, no. 1 (January 1, 2013): 2542 http://www.ncbi.nlm.nih.gov/pubmed/23507850.

Author contributions

The contributions of the various authors are listed below:

- *Kriti Sen Sharma*[1]: Implementation of FBP algorithm and modifications to FBP and SART-TV for micro-CT geometry (e.g. short-scan, center-shift etc.), numerical simulation, phantom fabrication and scans, experimental design, manuscript writing
- *Xin Jin*[2]: Coding framework for SART-TV, code debugging
- *Christian Holzner*[3]: Phantom fabrication, experimental design, manuscript writing
- *Shree Narayanan*[1] and *Masoud Agah*[1]: Phantom fabrication, manuscript writing
- *Baodong Liu*[4]: Code debugging, selection of parameters to characterize image reconstruction, manuscript writing
- *Dong Wang*[5] and *Linbing Wang*[5]: Scan of asphalt sample, analysis of reconstruction results

- *Hengyong Yu*[4] and *Ge Wang*[4,6]: Experimental design, manuscript writing

All authors contributed in terms of revising and improving the manuscript.

Author affiliations

1. Dept. of Elec. & Comp. Eng., Virginia Tech, Blacksburg, VA 24061, USA
2. Dept. of Eng. Phys., Tsinghua Univ., Beijing 100084, China
3. Xradia Inc., Pleasanton, CA 94588, USA
4. Biomedical Imaging Division, VT-WFU School of Biomedical Eng. & Sciences, Wake Forest Univ. Health Sciences, Winston-Salem, NC 27157, USA
5. Dept. of Civil Eng., Virginia Tech, Blacksburg, VA 24061, USA
6. Biomedical Imaging Division, VT-WFU School of Biomedical Eng. & Sciences, Virginia Tech, Blacksburg, VA 24061, USA

2.1 Abstract

High-resolution micro-CT offers 3D non-destructive imaging but scan times are prohibitively large in many cases. Advancements in image reconstruction offer great reduction in number of views while maintaining reconstruction accuracy; yet filtered back projection remains the *de facto* standard. An extensive study of few-view reconstruction using compressed-sensing based iterative techniques is carried out. Also, a novel 3D micro-CT phantom is proposed, and used for analyzing reconstruction accuracy. Numerical tests, and studies on real micro-CT data show that if measurement noise in projections is not extremely high, the number of views may be reduced to $1/8^{th}$ of the typically acquired view numbers. The study motivates the adoption of advanced reconstruction techniques to allow faster scanning, lower dosage, and reduced data size in high-resolution micro-CT.

2.2 Introduction

High-resolution micro computed tomography (micro-CT) scanners employ projection x-ray imaging using laboratory sources to achieve resolution on the order of 1 μm [26, 20, 8]. The resolution capability of 1 μm is higher than in clinical CT (resolution: 1 mm) and traditional micro-CT for small animal imaging (resolution: 50–100 μm). High-resolution micro-CT scanners are increasingly being used in universities, research organizations and industries for day-to-day imaging like well-established electron microscopy techniques (SEM/TEM). Also

while TEM, SEM are limited to thin samples, or surface imaging, micro-CT allows 3D non-destructive imaging of internal features [15, 21, 33]. However tomographic acquisition times on the scanners are quite high, ranging anywhere from 30 minutes to $>$ 6 hours [8, 15, 21]. Total scan time is mainly governed by 2 factors: exposure time per view, and total number of views (though additional time is also required for tasks like mechanical rotation between projections, reference collection, etc.) While exposure time is limited by factors like source flux, size of sample, and imaging mode [3], the total number of views may be selected by the user but directly affects reconstruction quality. A reduction in number of views by using an alternative reconstruction algorithm (while maintaining image quality) is the main focus of this paper.

Large number of views (and consequently, long scan duration) is especially problematic in applications where many samples have to be scanned as part of a research study, or in a routine process like failure analysis. Dose is usually not a major concern in high-resolution micro-CT as living organisms are not scanned. Yet, x-ray exposure can influence the sample in certain ways e.g. chemical bond-scissioning and cross-linking (i.e. changing the materials chemistry), heating, mass loss, etc. These effects are too small to be detected by the 1 μm resolution limit of micro-CT. Yet, the same effects may be important in studies where other analysis techniques besides imaging are involved (e.g. chemical composition measurements). Thus minimizing x-ray exposure by acquiring a lower number of views is beneficial to avoid exposure related effects. Finally, tomography datasets are usually stored in uncompressed formats and their sizes range anywhere from 1–15 GB. Even though high-capacity memory disks are relatively inexpensive these days, any reduction in number of views (especially if the reduction factor is $>$ 2) can have significant impact on digital storage costs and manageability.

Number of views in high-resolution micro-CT is typically selected between 1200–3000, though as many as 6000 views are also collected in certain cases. The large number is selected because reconstruction quality improves with number of views [12, 13, 37]. Filtered cone-beam back projection (FBP) is the *de facto* standard for reconstruction in high-resolution micro-CT [26, 8]. FBP is widely understood and easily implemented. However it is limited in its ability to handle special acquisition conditions e.g. smaller number of views, noise, and limited angle tomography [23].

Huge advances have been made in the solution of inverse problems, including tomographic reconstruction [6, 7, 36]. Based on compressed sensing (CS) theory, several groups have reported the ability to reconstruct CT images using far smaller dataset sizes than required by FBP [23, 36, 27]. The advantage of CS-based iterative techniques has been demonstrated in traditional (lower resolution) micro-CT, especially for small animal imaging [2, 17, 25], in solving the exterior reconstruction problem [38], for spectral CT [11] etc. Yet, algorithmic advances are rarely translated to the field and FBP remains the reconstruction algorithm of choice in all manufactured micro-CT scanners. The gap is attributable to many reasons, some of which are: (i) the proprietary nature of CT technology which makes it difficult for open-source developers to port their solutions to manufactured scanners, (ii) unavailability

of corrected raw projection datasets (since there are no DICOM like standards for CT data, data sharing is difficult), (iii) lack of easily adaptable (plug and play) image reconstruction software in the public domain, (iv) familiarity of manufacturers/users with FBP, and lack of immediate economic motivation to change [18].

In this paper, we report an extensive study on CS based few-view reconstruction in high-resolution micro-CT. No similar study has been reported before. Numerical tests were carried out on the Shepp-Logan phantom at various noise levels. A novel 3D micro-CT phantom was designed, and used in comparative analysis between FBP and CS-based iterative techniques. The 3D phantom is a novel contribution of this paper because currently only 2D phantoms, with sub-1 μm features etched on semiconductor, are used. The 2D phantoms provide important resolution information in the projection domain but the 3D phantom introduced here allowed analysis and quantification in reconstructed slices. Finally, few-view reconstruction results are reported on microstructure characterization of asphalt, as an example of a typical application for high-resolution micro-CT.

The remainder of the paper is organized as follows. First, the motivation for a new 3D micro-CT phantom, and its fabrication process is detailed in Sec. 2.3. In Sec. 2.4, we describe numerical tests, micro-CT samples and data acquisition. Sec. 2.5 describes image reconstruction algorithms, and metrics used to measure reconstruction accuracy. In Sec. 2.6, we discuss results obtained on the Shepp-Logan phantom, 3D micro-CT phantom and asphalt mastic. Finally we conclude the paper with discussion and future research directions in Sec. 2.7.

2.3 Micro-CT 3D Phantom

2.3.1 Motivation

Image resolution in sub-micrometer x-ray tomography is typically quantified by thin test patterns prepared using techniques similar to semiconductor fabrication. These contain a variety of structures that can be used for measuring image resolution, modulation transfer function etc. [22]. However due to the thin nature of the test patterns, the measurement is restricted to the projection domain. The level of detail inscribed in the test patterns is difficult to replicate in a three-dimensional phantom. However a 3-dimensional phantom would be useful for quantifying image resolution in the reconstructed slices.

Mizutani et al. described focused ion-beam (FIB) based fabrication of a sub-micrometer test object for quantification of image resolution in reconstructed slices [16]. Their test object consisted of a series of square wells carved on a flat surface — the pitches of square wave patterns ranged from 0.4 μm to 2 μm. While these features allow direct observation of resolution by examining which square wave patterns are resolved, the measurement is local. Measuring resolution at different locations in field-of-view would require repeated scanning

and reconstruction - and hence would be very time consuming.

Also, FIB is an analytical tool suitable for rapid prototyping and manipulation of materials at sub micrometer dimensions. From a production standpoint, it is more preferable to develop phantoms using conventional lithography. This allows batch fabrication through wafer-level processing, as against FIB, which operates spot by spot, in sequence. Recently a specific etch technique called deep reactive ion etching (DRIE) was developed which is more suited for high aspect ratios of 40 and above (FIB is capable of reaching aspect ratio of 10, but only under some exotic conditions) [4, 9].

In clinical CT where resolution is in the millimeter range, it is quite common to measure resolution using line spread functions across geometrically well-defined structures e.g. wire, spherical, and square phantoms [14]. A phantom containing an array of regular pillar like structures was fabricated for this study. Edge spread function was calculated as described in Sec. 2.5.3.

2.3.2 Fabrication

The fabrication method was adapted from a DRIE based technique to prepare micro-gas chromatography devices [1]. Specifically, a 4-inch <100> p-type silicon substrate of resistivity 0-100 ohm-cm was spun-coated with a photo-resist, AZ9260. This was then patterned and etched in an AMS-100 i-Speeder (Alcatel Inc., France) using an anisotropic silicon etch recipe to a depth of 330 μm. The patterned posts were a square of side 50 μm— these form the regular structures suitable for quantification using the line spread function technique. Following etching, the wafer was dipped in acetone and the residual photo-resist was stripped off in oxygen plasma. Fig. 2.1A is the scanning electron microscope image of a micro-pillar array created in this fashion. The wafer was then diced right through the devices into thin strips of $\sim$ 300 μm, using an MA-1006 dicing saw. The thin strip fit within the field-of-view of high-resolution micro-CT scanners, and was used as an edge phantom. Fig. 2.1B is a volume rendered image of the micro-CT scan of the 3D phantom.

2.4 Numerical Tests and Micro-CT Samples

All scans in this study were carried out on an Xradia MicroXCT-400 scanner (Xradia Inc., CA). Number of views was either 1200 or 1500. In numerical tests using the Shepp-Logan phantom, 1500 projections were generated to mimic real acquisition. Few-view datasets were generated from the 'many-view' datasets, by discarding all but every 2^{nd}, 4^{th}, 8^{th} or 16^{th} view (yielding datasets of size: 750, 375, 188, or 94 views respectively for the 1500 view datasets; and size: 600, 300, 150, 75 views for the 1200 view dataset). Image reconstruction was carried out on the original many-view sinogram and the different few-view sinograms using algorithms described in Sec. 2.5.

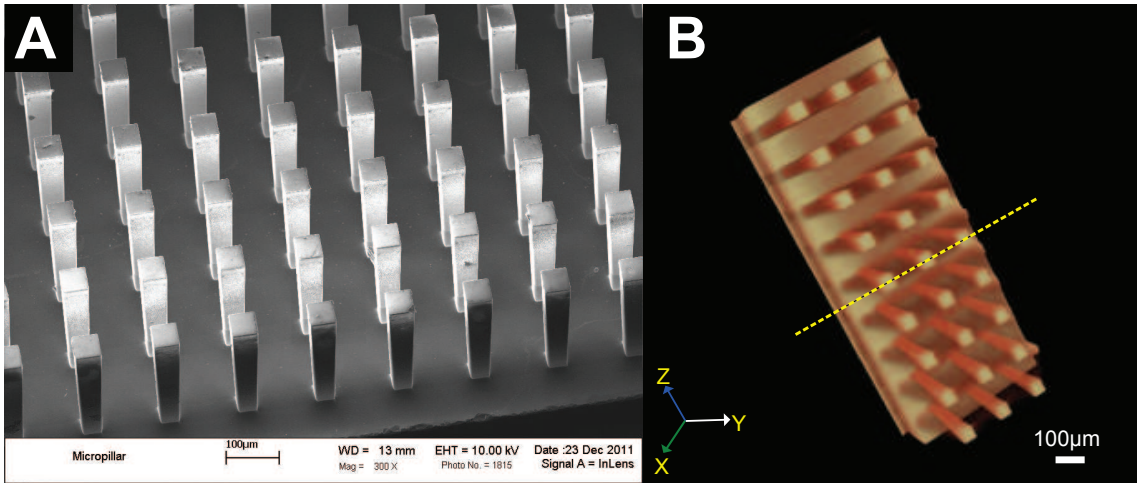

Figure 2.1: The 3D micro-CT phantom. (A) SEM image of micro-pillar array; the wafer was diced into thin strips and used as edge phantom. (B) Volume rendered image of a micro-CT scan of the 3D phantom: XYZ axes (where Z axis is rotation axis for tomography) are shown at bottom left. Yellow dotted line marks central slice of cone-beam geometry.

2.4.1 Tests on Shepp-Logan Phantom

Image reconstruction algorithms were initially tested on a Shepp-Logan phantom (of dimensions 256×256). Projection sinograms were generated from the numerical phantom by using scanning configuration values mimicking the experimental data collection on the micro-CT 3D phantom (see Table 2.1)

Noise Levels

The Poisson noise model is said to closely match statistics related to x-ray photons [12, 13]. To simulate real acquisition conditions, Poisson noise was added to the projection data generated from the Shepp-Logan phantom. Signal to noise ratio in the projections (Proj-SNR) was calculated as $\frac{<P_{noisy}>}{\sigma}$, where σ is the standard deviation of the difference sinogram ($P_{noisy} - P_{orig}$), and the $<>$ operator stands for the arithmetic mean. Using this quantification strategy, three different noise levels (with the levels roughly corresponding to low, medium and high noise) were considered. These are tabulated in Table 2.2.

2.4.2 Micro-CT Scans

The 3D micro-CT phantom was mounted on an Xradia micro-CT vise holder and scanned with the settings listed in Table 2.1. In this scan, a beam-hardening correction filter (Xradia

Table 2.1: Scan settings for study on few-view reconstruction. Scans were acquird on the Xradia MicroXCT-400 scanner and for 3D micro-CT phantom and asphalt mastic sample (RA = rotation axis).

Scan Parameter	**3D Phantom**	**Asphalt mastic**
Source setting	80 kV, 100 μA	80 kV, 100 μA
Source-RA distance	18.9951 mm	36.2326 mm
Detector-RA distance	14.9951 mm	6.9801 mm
Pixel size	1.4908 μm	2.2368 μm
Magnification objective	10X	10X
Exposure time	2.0 sec	8.0 sec
Camera binning	2	2
Start-angle	-93.0°	-93.0°
End-angle	93.0°	93.0°
Number of projections	1500	1200

Table 2.2: Projection noise levels in numerical simulations. Three projection noise-levels were used for numerical simulation using the Shepp-Logan phantom. Corresponding projection-SNR values are also noted.

Noise-level	N1	N2	N3
Proj-SNR	150	100	50

Inc., CA) was placed after the source to pre-harden the beam. The other sample scanned on the micro-CT scanner was an asphalt mix as part of a study on asphalt concrete pavements [29]. For scanning, the asphalt mastic was reshaped and put into a conical plastic holder with a tapering tip; scan parameters are detailed in Table 2.1.

2.5 Image Reconstruction

The Xradia MicroXCT-400 scanner used in this study has a cone-beam scanning geometry [8]. The central slice of the cone-beam (which is in fan-beam geometry) is focused on for our analyses, as this limits the problem to 2D and allows faster execution [5]. The primary motivation for this study is to compare different reconstruction algorithms, and the fan-beam image reconstruction algorithms described here can be extended to the cone-beam case. It is well known that practical Feldkamp-type cone-beam reconstruction methods are based on modified fan-beam reconstruction formulas [31]. In Fig. 2.1B, a yellow dotted line marks the central slice of scanned object.

Image reconstruction was carried out using FBP and CS-based iterative techniques. Reconstructed image size was 256×256 in case of numerical tests, and 1024×1024 in case of real datasets. In case of the Shepp-Logan phantom, the 'ground truth' (i.e. the exact values of the object attenuation coefficients) is known. In numerical tests, the ground truth was utilized for 3 purposes – (i) visual comparison, (ii) comparison of line profiles, and (iii) calculation of noise in reconstructed slices. In studies involving real data, FBP reconstruction of the many-view dataset (1200 or 1500 views) was taken as best estimate of ground truth. However, this best estimate was used for purposes (i) and (ii) above. For calculating reconstruction noise, a different approach was used (explained below in Sec. 2.5.3).

In this section, the implementation of FBP and CS-based iterative techniques is described in brief with references to relevant literature. For sake of completeness, and to provide a unified formulation of the reconstruction algorithms used in this study, a detailed appendix 2.9 has been added.

2.5.1 Filtered Back Projection

High-resolution micro-CT scanners acquire projection data in half-scan mode i.e. angular range equals (180°+ fan-angle). Consequently, half-scan fan-beam FBP algorithm [19] was implemented.

Xradia micro-CT scanner used in this study has a fixed source-detector configuration. Initial sample stage alignment was done to bring the center of mechanical rotation to the mid-line of the fan-beam [26]. However despite best efforts using visual analysis, the center of rotation may be displaced by a few image pixels. Our FBP implementation was modified to adjust

for displaced center of rotation[10]; without this, reconstruction images suffered from loss of resolution and structured artifacts.

2.5.2 Iterative Reconstruction

The imaging model may be described by a discrete-to-discrete linear transform,

$$\overrightarrow{p} = \mathbf{W}\overrightarrow{f}, \tag{2.1}$$

where $\overrightarrow{p} = \{p_i\}$ is the measured projection data, $\overrightarrow{f} = \{f_j\}$ is the set of sampled image pixels, and $\mathbf{W}$ is the system matrix. Individual elements of the system matrix are w_{ij} which signify the contribution of the j^{th} pixel to the i^{th} detector bin — these are calculated as described in [23]. The reconstruction problem involves the determination of unknown image pixels $\overrightarrow{f}$, using measured $\overrightarrow{p}$, and knowledge of $\mathbf{W}$. CS based iterative techniques have been found to be very effective in providing high quality reconstruction [36, 27]. Specifically, the total variation (TV) of the image is minimized while imposing data-consistency, i.e.

$$\min||\overrightarrow{f}||_{TV} \quad \text{such that } \mathbf{W}\overrightarrow{f} = \overrightarrow{p} \tag{2.2}$$

where, TV is defined as the sum over all pixels of the image gradient at each point. This may be approximated as:

$$||f||_{TV} = \sum_{x,y} |\overrightarrow{\nabla} f_{x,y}| = \sum_{x,y} \sqrt{(f_{x,y} - f_{x-1,y})^2 + (f_{x,y} - f_{x,y-1})^2} \tag{2.3}$$

Briefly, the iterative reconstruction algorithm used in this study may be summarized as follows:

Step 1: Imposition of data-consistency condition $\mathbf{W}\overrightarrow{f} = \overrightarrow{p}$ by 1 iteration of simultaneous algebraic reconstruction technique (SART) [13]. In the context of ordered subset SART defined in [30], each ordered subset in our implementation consisted of only 1 projection.

Step 2: Calculation of TV gradient [23], and TV minimization by gradient descent technique, i.e. $\min||\overrightarrow{f}||_{TV}$. After 1 iteration of SART, TV minimization was carried out (with multiple sub-iterations, as explained in Sec. 2.5.2).

Step 3: Steps 1 and 2 together form 1 iteration of SART-TV. Till maximum number of SART-TV iterations is reached **or** residual error falls below a pre-decided threshold, go to Step 1 and repeat.

100 iterations of SART-TV were used for all results in this study. For noisy data, iterative reconstruction algorithms tend to diverge if too many iterations are carried out. Hence early stopping is advisable in such cases [13]. While we found the reconstruction to diverge if we used SART alone, SART-TV did not diverge within 100 iterations.

A more detailed description of the algorithm is available at [23]. However our implementation differed in certain ways that are described here. First, we employed SART instead of ART [13]. Second, we skipped the enforcement of positivity constraint of [23] — enforcing the constraint led to artifacts in reconstructed image. Third, instead of using a zero image for initializing the iterative reconstruction process, we utilized a Gaussian blurred version of the few-view FBP reconstructed image (with $\sigma_{\text{blur}} = 5$ pixels). This choice of the initial image allowed faster convergence. Finally, we used a different set of reconstruction parameters.

Choice of reconstruction parameters

Parameters for SART and TV are explained in detail in Appendix 2.9; briefly, relaxation parameter λ of SART was fixed at 0.8, and the α parameter for TV minimization was set at 0.2. After trying various combinations of λ and α, we selected this particular combination as it gave visually good results for both our real datasets. Then we proceeded to use these parameter values in our numerical tests — we were motivated to observe how these SART-TV parameters perform at different noise conditions. A more rigorous selection procedure for iterative reconstruction parameters is possible (at least in numerical tests) and may improve the results for high-noise conditions [32]; but this requires large computational effort.

Within the TV minimization step, multiple iterations are carried out. Number of TV iterations is an important parameter — higher number of TV minimization iterations leads to smoother images. For choosing the optimum number of TV iterations while reconstructing the few-view datasets, 1, 5, 10, 20, or 40 iterations were carried out. Subsequently, the final result after 100 SART-TV iterations was compared with the ground truth. TV iteration number that gave the closest match to the ground truth was selected. Closest match was ascertained by visually comparing images and line profiles.

For simulations on the Shepp-Logan phantom, it was found that 20 TV iterations yielded best reconstruction results. For real datasets acquired on the micro-CT scanner (the 3D phantom and asphalt mastic), 5 TV iterations gave best results.

The difference in TV iteration lengths may be explained by the nature of the TV minimization process, and the type of the image we want to retrieve. It is generally known that using higher number of TV iterations leads to higher image smoothing. The ground truth in case of the Shepp-Logan phantom is a piece-wise constant function with very few discontinuities; a higher TV iteration number is required to reach the piece-wise constancy of the phantom. In case of real datasets, there cannot be any established ground truth, and thus our aim was to retrieve images that appear similar to the many-view FBP reconstruction. Given the

general micro-CT practician's familiarity with FBP, this is a reasonable target. Using only 1 TV iteration led to extremely noisy images, while 10 or more iterations led to over-smooth images. The optimum number of TV iterations was found to be 5.

2.5.3 Image quality metrics

Reconstructed images were analyzed by visual comparison with the ground truth and by comparing line profiles across specific image features. Apart from this, following metrics were used.

Reconstruction SNR

In the Shepp-Logan phantom, the actual ground truth is known, and the entire image was used for calculating noise. For the 3D micro-CT phantom, 4 ROI-s (see Fig. 2.2B) were selected which had low variance in the many-view FBP. Each ROI was a square of 121 pixels within a total image size of 1024×1024. The mean (σ_{mean}) of standard deviation of pixel values in these regions gave a measure of the reconstruction noise. Signal to noise ratio in reconstructed images (Recon-SNR) was then calculated as $\frac{<\text{Reconstructed image}>}{\sigma_{\text{mean}}}$.

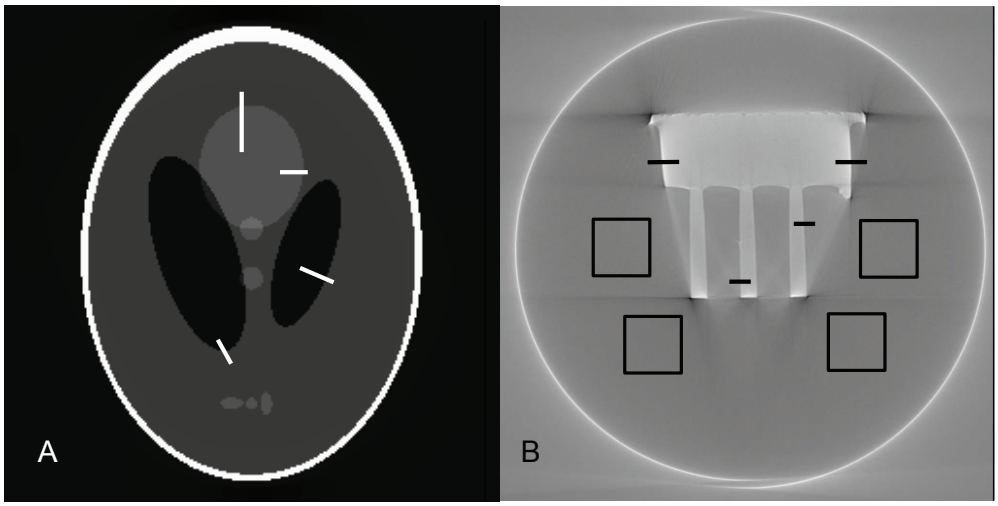

Figure 2.2: Noise and resolution measurement in reconstructed images. (A) The Shepp-Logan phantom — noise was measured by comparing with the ground truth across entire image. (B) The 3D micro-CT phantom — ROI-s used for measuring standard deviation of noise are marked by boxes. For both images, FWHM was measured across the selected line profiles; subsequently, the mean FWHM along with standard deviation among measurements was reported.

Image resolution

To quantify image resolution, the point spread function (PSF) of the reconstructed image was estimated. Lines were drawn across selected distinct edges as shown in Fig. 2.2 — the line profiles yield an estimate of the edge-spread function (ESF). The line spread function (LSF) was calculated respectively as the derivative of ESF. Assuming a PSF which is symmetric in both x and y directions, an inverse radon transform was utilized to determine the PSF [24]. Subsequently the width of the PSF was expressed by its full-width-at-half-maximum (FWHM) — higher FWHM signifies lower resolution.

The assumption of x-y symmetry may not lead to exact PSF estimation. However, our FWHM determination method is sufficient for our purpose of comparing reconstruction algorithms. For both numerical and real phantom, the FWHM was calculated at 4 locations in the image (marked in Fig. 2.2). The average FWHM, along with standard deviation among the different locations, was reported.

Sharpness

The most difficult to resolve feature in the Shepp-Logan phantom is the set of 3 small ellipses in the lower half of the phantom (see Fig. 2.3B). As we reduced the number of views, or increased projection noise, the corresponding decrease in reconstructed image quality was reflected very well at the 3 ellipses. For high quality reconstruction, these ellipses were clearly separated; for low quality reconstruction, it was difficult to visually distinguish the ellipses. To specifically quantify this behavior, and thus provide some more insights into reconstruction performance than provided by Recon-SNR and FWHM, we defined a new parameter called sharpness.

In subfigure 2.3C, a line profile through the reconstructed image is compared with an ideal line profile through the phantom. The set of pixel locations corresponding to crests and troughs in the original image is determined beforehand. Corresponding pixels in the reconstructed image are located, and average value in each set are separately calculated (c_1, c_2, c_3 for crests, and t_1, t_2, t_3, t_4 for troughs). The mean height of the undulations is calculated as the average of $(c_1 - t_1)$, $(c_1 - t_2)$ etc. In the numerical phantom, the height of undulation is always 0.1. Sharpness is then calculated as:

$$\text{Sharpness} = \frac{< (c_1 - t_1), (c_1 - t_2), \ldots >}{0.1} \times 100$$

where the <> operator stands for the arithmetic mean. As a general judgment criterion for sharpness, the closer sharpness value is to 100, the better the reconstruction accuracy.

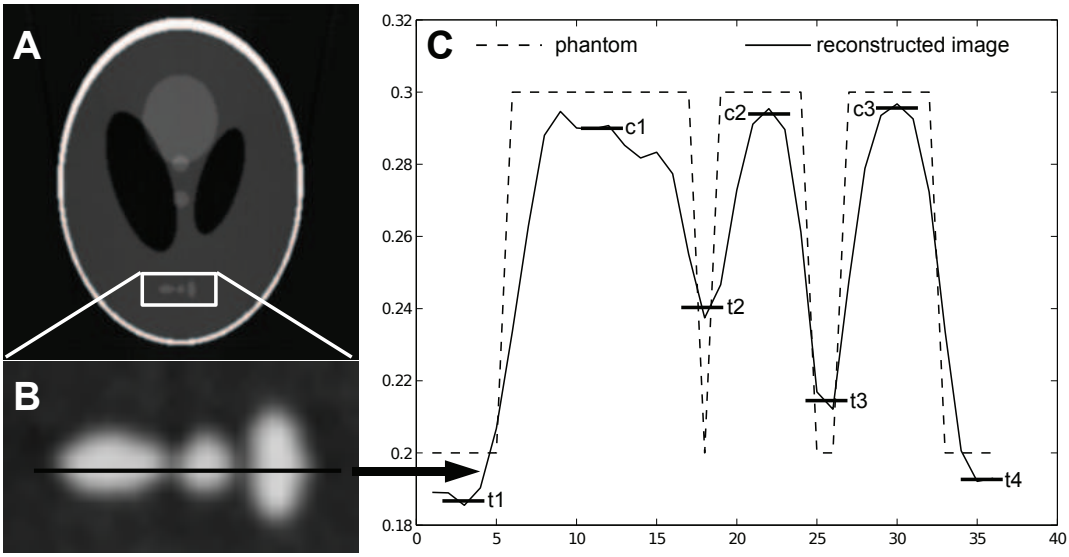

Figure 2.3: Procedure for calculating sharpness parameter. (A) Reconstruction of the Shepp-Logan phantom, and (B) zoomed in ROI containing the 3 small ellipses. (C) line profile is drawn across the 3 ellipses, and compared with line profile through original image. c_1, c_2, c_3 are average values of crest and t_1, t_2, t_3, t_4 are average value of troughs in reconstructed line profile.

2.6 Results

2.6.1 Simulations on Shepp-Logan Phantom

In Fig. 2.4, SART-TV reconstruction using 188 projections is compared with 1500 view FBP reconstruction at different noise levels. First, we note that FBP provides consistently good reconstruction quality at all noise levels when 1500 projections are used (subfigures B, G, L). The consistent performance across different noise levels is due to the fact that FBP contains a low-pass filter (in our implementation, a Hanning filter) that limits the effect of noise. However the reconstruction using FBP has severe artifacts at 188 projections (C, H, M) — there are lines visible in the background for insufficient angular sampling; also the sharpest feature (as seen in zoomed in ROI-s in C′, H′, M′) is not resolved well. Thus FBP is not a suitable technique for few-view reconstruction.

In subfigures D, I, N, it is visible that 188 view SART-TV reconstruction is as good as 1500 view FBP reconstruction. Only at the high noise level N3, SART-TV fails to resolve the set of 3 ellipses as well as 1500 view FBP (see subfigure N′). However overall reconstruction by SART-TV is still better than few-view FBP.

In Fig. 2.4, in order to highlight the efficacy of the SART-TV algorithm, we also compare results by FBP-TV (FBP followed by TV minimization, subfigures E, J, O) and SART without TV minimization (subfigures F, K, P). In FBP-TV reconstruction, the α parameter for TV minimization was set at 0.01, and 20 TV iterations were carried out. Comparing all results, SART-TV clearly has the best reconstruction results.

Metrics described in Sec. 2.5.3 – Recon-SNR, FWHM and sharpness were measured for the Shepp-Logan phantom and are plotted in Fig. 2.5. Metrics for SART-TV are plotted at the 3 different noise levels described in Table 2.2. In plots corresponding to FBP Recon-SNR and FBP sharpness, the standard deviation across various noise levels is plotted as error bars. The error bars are extremely small (not visible for the Recon-SNR plot at the considered scale). A similar value for FBP at all noise levels reiterates our previous observation that FBP has consistent results over different noise levels. In subfigure A, it is seen that Recon-SNR for SART-TV is higher than that for FBP at all noise levels. Similarly FWHM is lower (i.e. resolution is higher) for SART-TV (see subfigure B). In subfigure C, sharpness value for SART-TV is higher at all noise-levels except level N3. However, no one metric can be considered alone, and for few-view FBP, the lower Recon-SNR (i.e. higher noise) undermines a favorable sharpness parameter. For example, at 188 views, FBP-sharpness value is higher than SART-TV; yet zoomed-in ROI in Fig. 2.4M′ shows that the image is too noisy.

Considering all the results in this section, the following prediction can be made: for low to moderate projection noise levels, SART-TV can achieve reconstruction quality similar to many-view FBP, but using significantly lower data (as low as $1/8^{th}$ of the view numbers required by FBP).

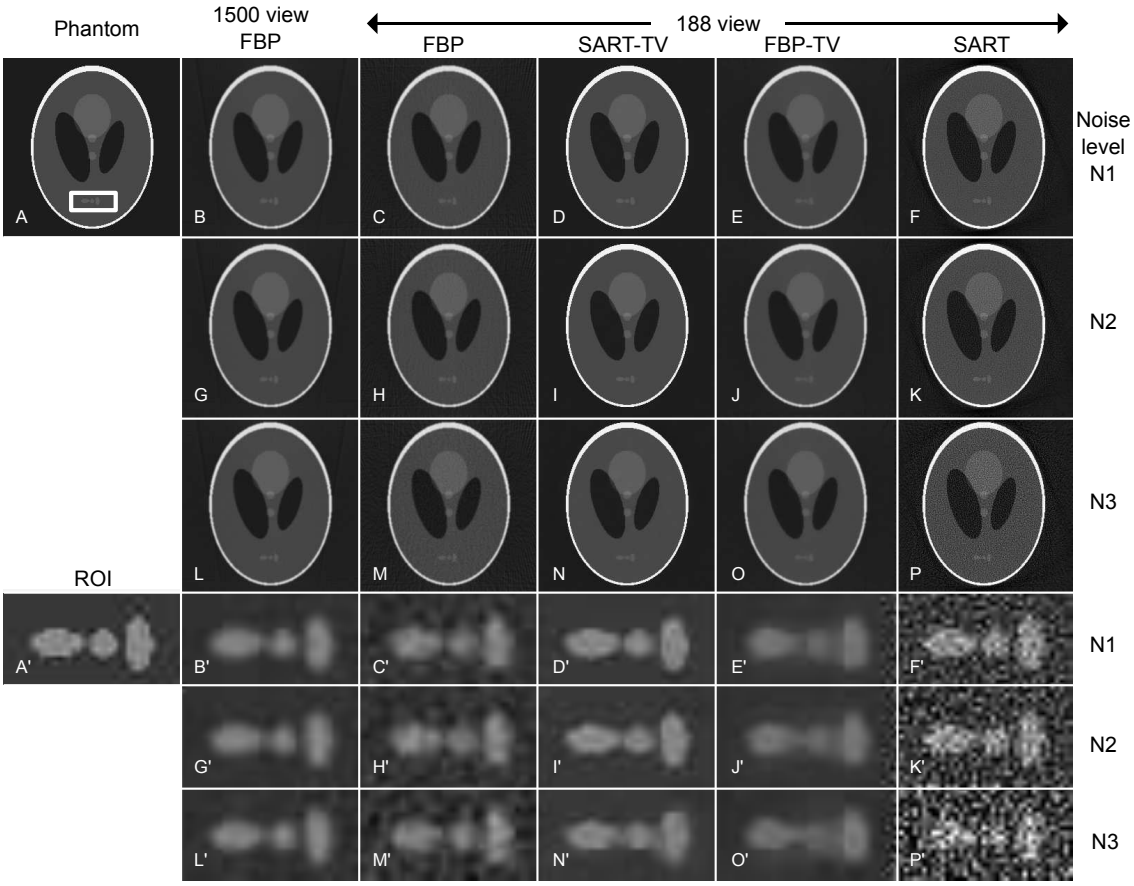

Figure 2.4: Few-view reconstruction at different noise levels. Few-view (188 views) reconstruction was compared with many-view (1500 views) reconstruction at 3 different noise levels. ROI containing 3 small ellipses marked in subfigure A. Reconstruction was carried out at 3 different noise levels – N1 (B-F), N2 (G-K), and N3 (L-P). Number of views and reconstruction algorithms: 1500 view FBP (B, G, L), 188 view FBP (C, H, M), 188 view SART-TV (D, I, N), 188 view FBP-TV (E, J, O), 188 view SART (F, K, P). For each reconstruction, corresponding zoomed-in ROI-s are in (A′) – (P′).

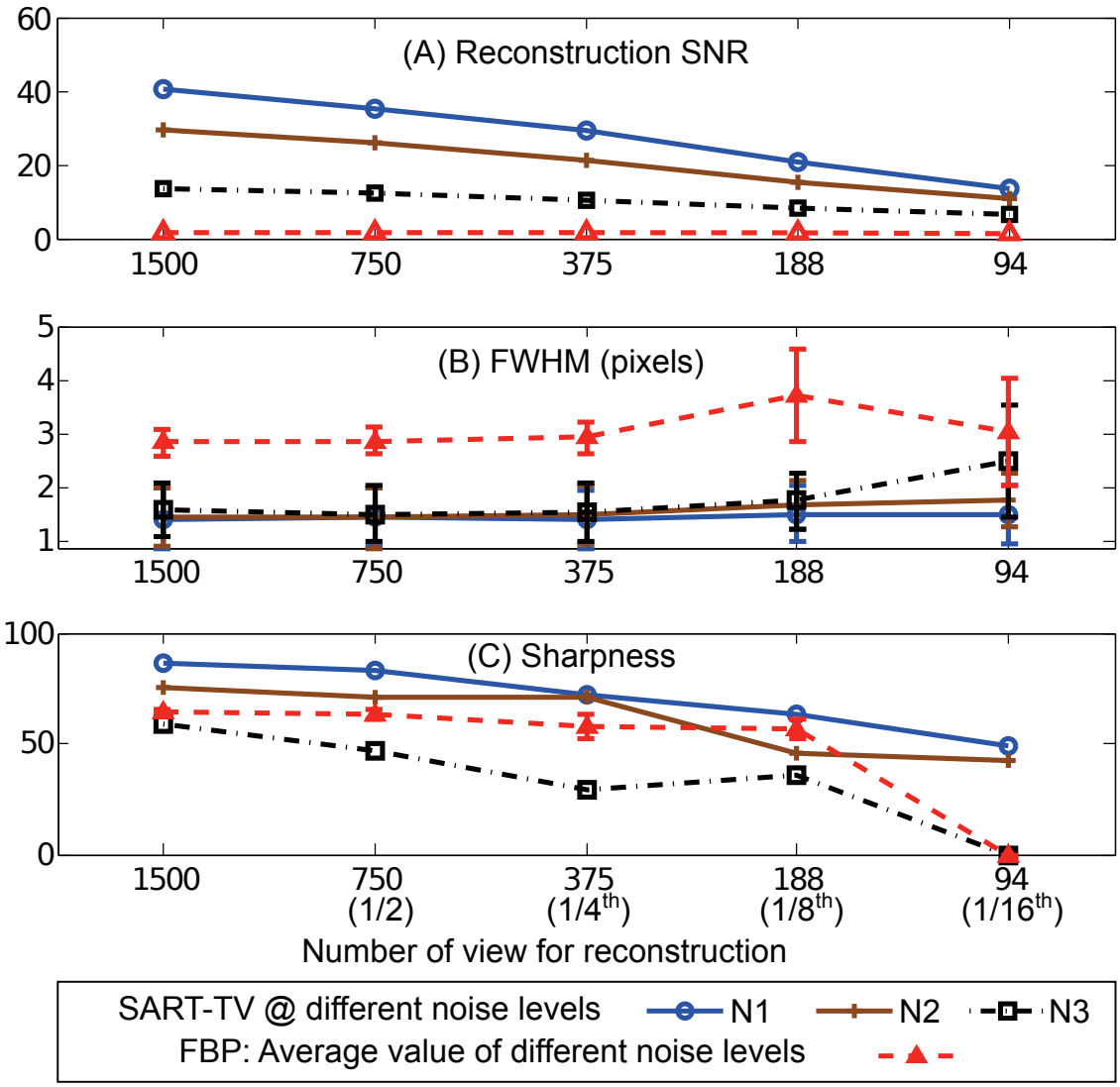

Figure 2.5: Reconstruction metrics for the Shepp-Logan phantom. (A) Reconstruction-SNR (or Recon-SNR), (B) FWHM, and (C) sharpness. Number of views used for reconstruction is plotted on x-axis.

2.6.2 Results on 3D micro-CT phantom

Fig. 2.6 contains reconstructed images for the 3D micro-CT phantom and line profiles across a chosen feature. In subfigures A–C, it is seen that FBP image worsens significantly as the projection dataset sizes decreases from 1500 to 94. However SART-TV reconstruction is consistently good at all dataset sizes (as seen in subfigures D–F). Subfigure G graphs the line profiles across selected feature corresponding to reconstructions in A–C. It is seen that line profiles for FBP becomes increasingly noisy for few-view FBP reconstruction. In contrast to this, SART-TV line profiles in subfigure H match up well across different number of views. All the SART-TV line profiles also match up well with line profile for 1500 view FBP.

Metrics of Recon-SNR and FWHM were calculated for 3D micro-CT phantom and the plots are shown in Fig. 2.7. Reconstruction-SNR is higher for SART-TV when compared with FBP; simultaneously, FWHM is lower (i.e. resolution is higher) for SART-TV. When we go as low as 94 views, the improvement in FWHM for SART-TV is not significant because the error-bars overlap. The overall trend in metrics is similar to the trend seen for simulations using the Shepp-Logan phantom. Considering the results in Figs. 2.6 and 2.7, it is clear that that SART-TV allows good few-view reconstruction using only 188 views whereas FBP required 1500 views. Thus SART-TV allows an 8-fold reduction in micro-CT data acquisition time, dosage and dataset size.

2.6.3 Results on asphalt mastic

Fig. 2.8 contains reconstructed images for asphalt mastic and line profiles across a chosen feature. For this sample, SART-TV was able to give accurate reconstruction with 150 or more projections (as seen in subfigures D–F). For the few-view datasets consisting of 150 or 300 projections, FBP reconstructions in subfigures A–C were considerably affected by noise and streaking artifact. The artifacts in FBP reconstruction are most evident by comparing the line profiles through these images (subfigure G) — there is significant change in the line profiles as the number of views decreases. In contrast, line profiles for SART-TV reconstruction in subfigure H have a lesser degree of variation. Also, the SART-TV line-plots plots match up well with the line-plot for 1200 view FBP. Again, an 8-fold reduction in the number of views was achieved.

2.7 Conclusions and Discussion

In this study, CS-based iterative reconstruction has been used for an extensive analysis of few-view reconstruction in high-resolution micro-CT. Tests were carried out on a Shepp-Logan phantom at various noise levels. The tests show that few-view SART-TV has reconstruction accuracy similar to many-view FBP, except at high noise level. A novel 3D micro-CT

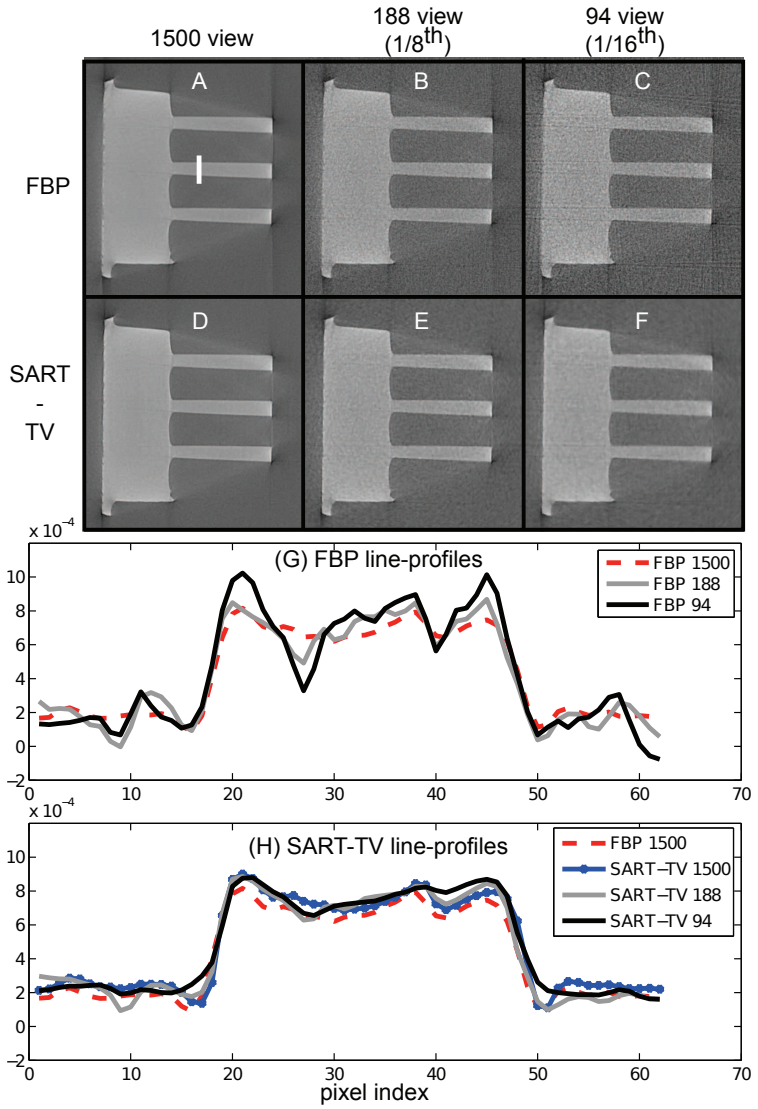

Figure 2.6: Few view reconstruction on the 3D micro-CT phantom. Reconstructed images using 1500, 188 ($1/8^{th}$) and 94 ($1/16^{th}$) views respectively for FBP (A–C) and SART-TV (D–F). Plots compare line profiles (line marked in subfigure A) across different number of projection views for FBP (G) and SART-TV (H). Subfigure H also contains 1500 view FBP line-plot for reference. x axis is pixel index along selected line.

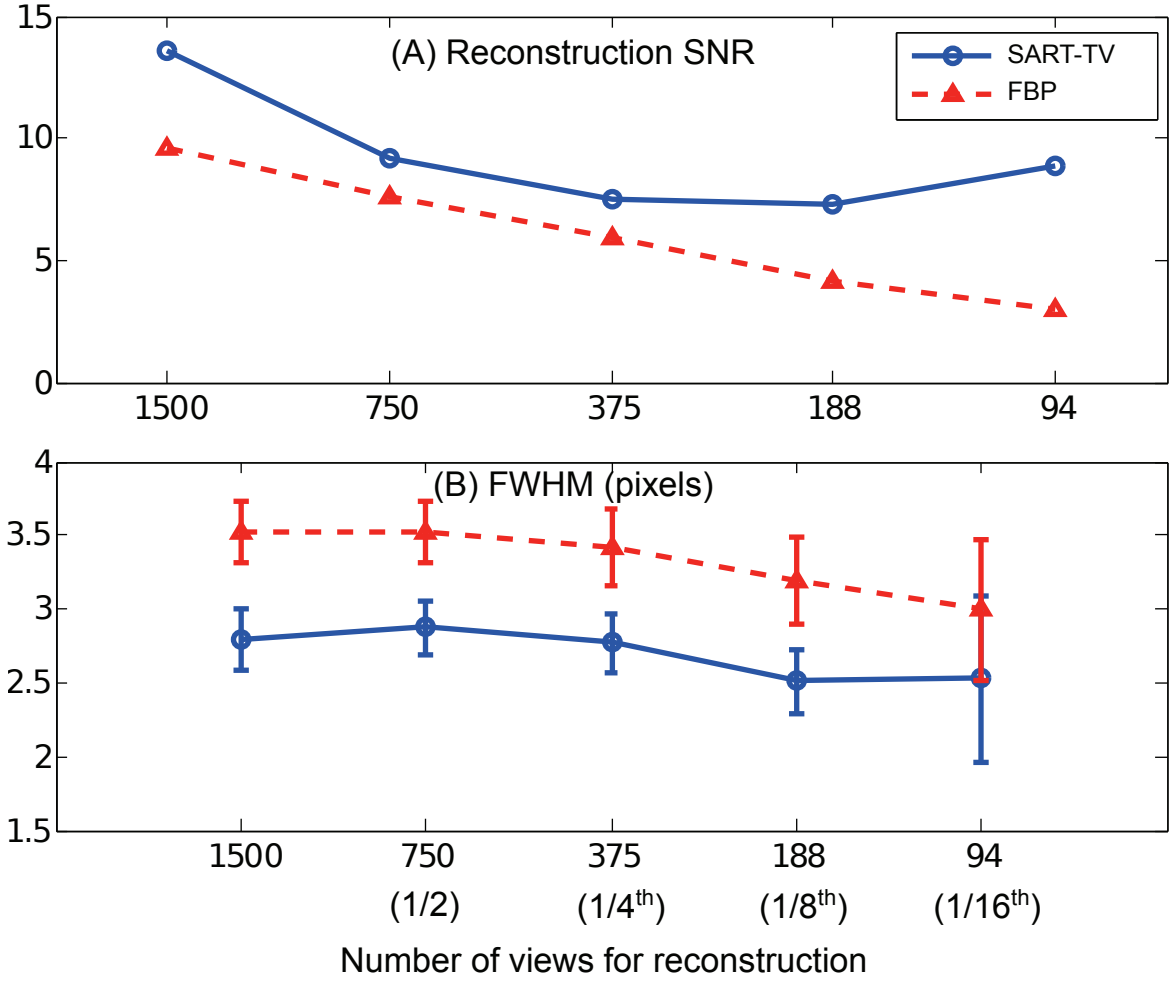

Figure 2.7: Reconstruction metrics for the 3D micro-CT phantom. (A) Recon-SNR, and (B) FWHM. Number of views used for reconstruction is plotted on x-axis.

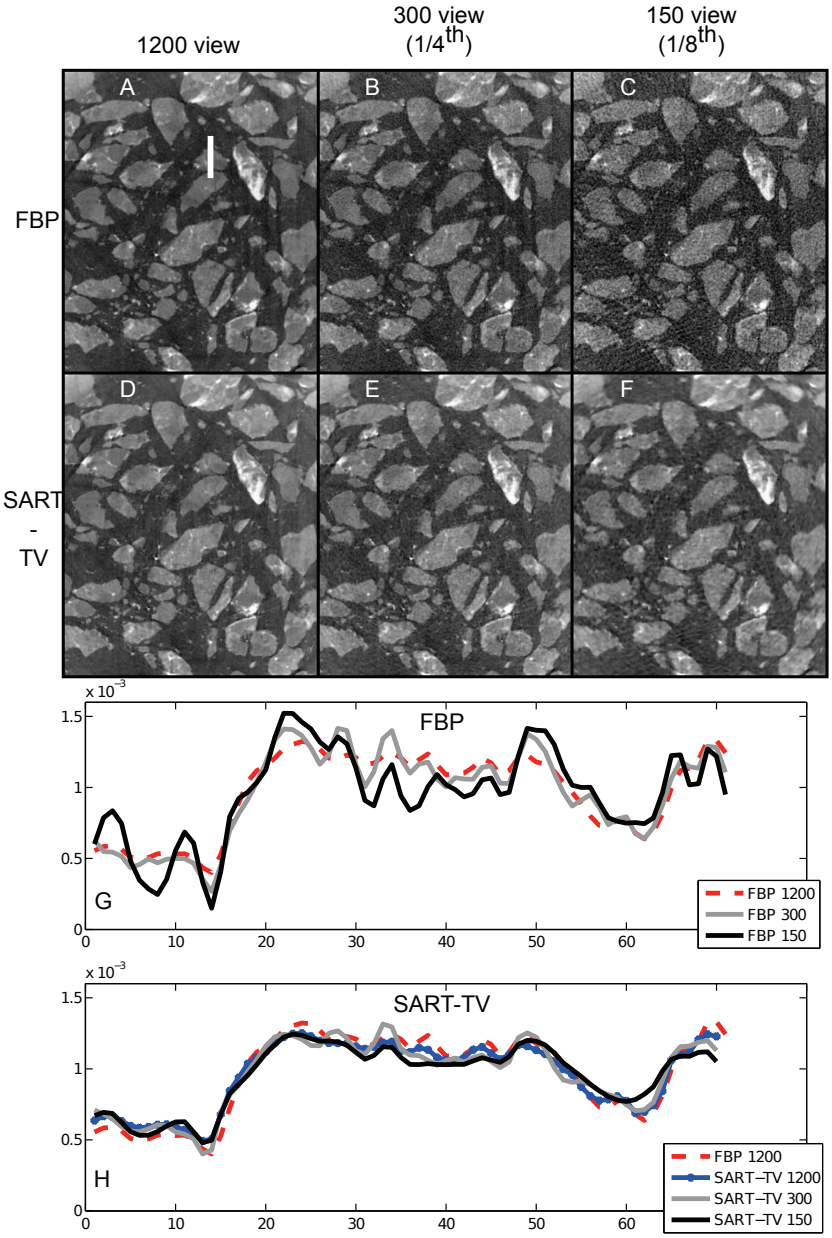

Figure 2.8: Few view reconstruction on asphalt dataset. Reconstructed images using 1200, 300 ($1/4^{th}$) and 150 ($1/8^{th}$) views respectively for FBP (A–C) and SART-TV (D–F). Plots compare line profiles (line marked in subfigure A) across different number of projection views for FBP (G) and SART-TV (H). Subfigure H also contains 1200 view FBP line-plot for reference. x axis is pixel index along selected line.

phantom was fabricated and used to compare reconstruction accuracy between FBP and CS based reconstruction techniques. The 3D phantom allows resolution quantification in reconstructed slices, whereas earlier 2D micro-CT phantoms offered information in projection domain alone. Finally, a typical micro-CT sample consisting of asphalt mastic was studied. The two real datasets provided significantly different test cases — while the 3D micro-CT phantom is a homogeneous sample with regular well-defined structures, the asphalt mastic is a more complex sample with irregular structures. It was found that high quality images could be reconstructed using as less as $1/8^{th}$ the number of views required by a comparable FBP reconstruction. Overall, the results provide sufficient motivation for adopting iterative reconstruction techniques to reduce number of views acquired (and consequently data acquisition time, dosage) in high-resolution micro-CT.

Future research directions include a study of the noise model in high-resolution micro-CT, incorporation of other CS based mathematical models, implementation of GPU based reconstruction [34], and comparison with recently reported methods that improve CT scan efficiency [28, 35].

2.8 Acknowledgments

The authors thank Michael Feser and Tom Case for their advice about raw-data corrections before reconstruction, reconstruction performance metrics, manuscript write-up, etc. The authors thank Christopher Wyatt for his suggestions about the 3D phantom. The CT studies were performed in the SBES Advanced Multiscale Computed Tomography Facility (SAMCT), supported by an NIH SIG grant (RR025667), an NSF MRI grant (CMMI0923297) as well as internal funding from ICTAS and SBES at Virginia Tech.

2.9 Appendix: Details of Image Reconstruction

Image Model

As shown in Fig. 2.9, two different notations are used for describing the image model. These can be used interchangeably i.e. the image basis function can be described equivalently by both:

$$f(x, y), \quad \text{with } x = 1, 2, \ldots W, y = 1, 2, \ldots H$$

where W is the width and H is the height of the image), and by

$$\overrightarrow{f} = \{f_j\} \quad \text{where } j = 1, 2 \ldots N, (N = W \times H)$$

Similarly, the projection data can be represented by either the form

$$R(\beta, s)$$

where β is the projection angle and s is the detector index, or the form

$$\overrightarrow{p} = \{p_i\} \quad \text{where } i = 1, 2 \ldots M \tag{2.4}$$

The mid-line of the fan-beam is shifted from the center of rotation by an amount τ. The distance from source-to-center is D, while it is assumed for mathematical purposes that the source-to-detector distance D' is equal to D.

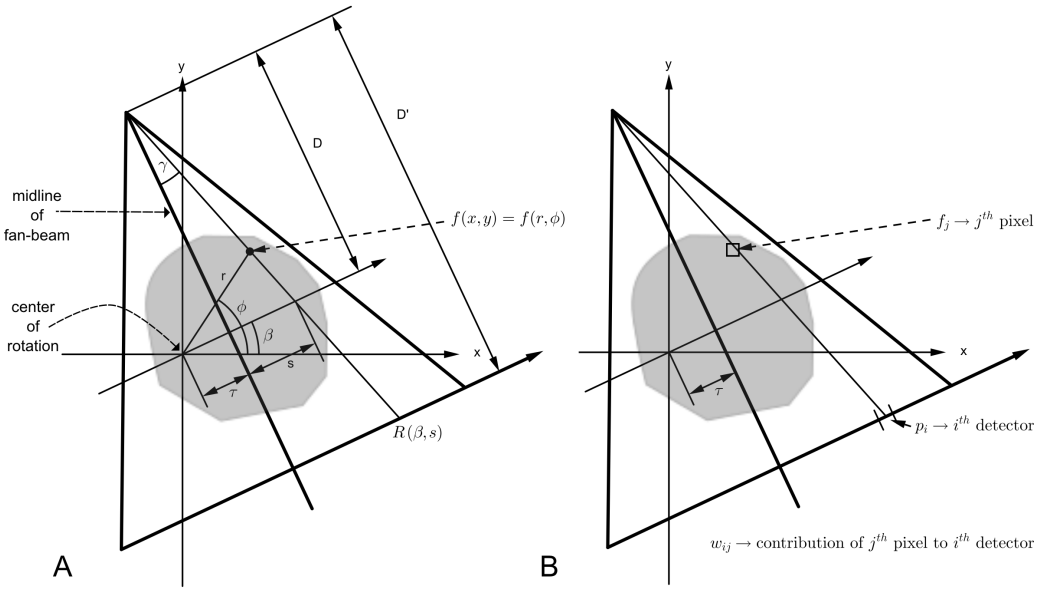

Figure 2.9: Imaging model for few-view reconstruction. Two different notations are used for (A) filtered back-projection and TV minimization, and (B) simultaneous algebraic reconstruction technique (SART).

Filtered Back Projection

Fan-beam filtered back-projection algorithm was implemented along with modifications for short scan and displaced center of rotation. The complete algorithm is as follows:

(A) Angle subtended by each detector bin calculated as

$$\gamma = \tan^{-1}\left(\frac{s}{D}\right) \tag{2.5}$$

(B) Weighting for short scan [13, 19]

$$R'(\beta,\gamma) = R(\beta,\gamma) \times w_\beta(\gamma) \tag{2.6}$$

where

$$w_\beta(\alpha) = \begin{cases} \sin^2\left(\frac{\pi}{4}\frac{\beta}{\gamma_m-\gamma}\right), & 0 \le \beta \le 2\gamma_m - 2\gamma \\ 1, & 2\gamma_m - 2\gamma \le \beta \le \pi - 2\gamma \\ \sin^2\left(\frac{\pi}{4}\frac{\pi+2\gamma_m-\beta}{\gamma+\gamma_m}\right), & \pi - 2\gamma \le \beta \le \pi + 2\gamma_m \end{cases} \tag{2.7}$$

and γ_M is the angle subtended by the outermost detector bin at the fan-beam mid-line.

(C) Weighting for displaced center of rotation [10].

$$R''(\beta,s) = R'(\beta,s) \times \frac{D - \frac{\tau s}{D}}{\sqrt{D^2+s^2}} \tag{2.8}$$

(D) Convolution of $R''(\beta,s)$ with the smoothed Ram-Lak filter $h(s)$ [13] to get $Q_{\beta_i}(s)$. We used a Hanning filter as the smoothing filter.

(E) Weighted back projection to yield the reconstructed image $f(x,y)$

$$f(x,y) = \Delta\beta \sum_{i=1}^{M} \frac{1}{U^2(x,y,\beta_i)} Q_{\beta_i}(s') \tag{2.9}$$

where

$$U = \frac{r sin(\beta-\phi) + D}{D} \tag{2.10}$$

and s' denotes the ray that passes through the image point (x,y) at the angle β_i. The value of Q_{β_i} at the point s' is interpolated from the measured projection at discrete data points.

CS-based iterative reconstruction

As described in Sec. 2.5.2, the CS-based iterative reconstruction employed in this study is similar to the implementation in [23]. Data consistency was enforced by the SART algorithm using the formula below [30]:

$$f_j^{(k+1)} = f_j^{(k)} + \lambda \sum_{i \in P(\psi)} \frac{w_{ij}}{\sum_{i \in P(\psi)} w_{ij}} \left(\frac{p_i - \mathbf{W}_i \overrightarrow{f^{(k)}}}{w_{i+}} \right)$$

where

$$w_{i+} = \sum_{j=1}^{N} w_{ij}, \tag{2.11}$$

k is iteration number, and $\mathbf{W}_i$ is a row of the system matrix composed of weight elements w_{ij}. $\mathbf{W}_i\overrightarrow{f^{(k)}}$ yields the forward-projected result at the i^{th} detector bin. The summation over i, i.e. $\sum_{i \in P(\psi)} w_{ij}$ is over all rays intersecting j^{th} pixel at fixed angle ψ. The parameter λ was chosen to be 0.8.

Also, the gradient descent step for TV-minimization [23] was controlled by the parameter α.

Bibliography

[1] Bassam Alfeeli, Daniel Cho, Mehdi Ashraf-Khorassani, Larry T. Taylor, and Masoud Agah. MEMS-based multi-inlet/outlet preconcentrator coated by inkjet printing of polymer adsorbents. *Sensors and Actuators B: Chemical*, 133(1):24–32, July 2008.

[2] T M Benson and J Gregor. Three-dimensional focus of attention for iterative cone-beam micro-CT reconstruction. *Physics in medicine and biology*, 51(18):4533–46, September 2006.

[3] M. Boone, Y. De Witte, M. Dierick, J. Van Den Bulcke, J. Vlassenbroeck, and L. Van Hoorebeke. Practical use of the modified Bronnikov algorithm in micro-CT. *Nuclear Instruments and Methods in Physics*, 267(7):1182–1186, April 2009.

[4] V. Callegari, P. M. Nellen, J. Kaufmann, P. Strasser, F. Robin, and U. Sennhauser. Focused ion beam iodine-enhanced etching of high aspect ratio holes in InP photonic crystals. *Journal of Vacuum Science and Technology B: Microelectronics and Nanometer Structures*, 25(6):2175, 2007.

[5] Bruno De Man, Samit Basu, JB Thibault, J. Hsieh, JA Fessier, C. Bouman, and K. Sauer. A study of four minimization approaches for iterative reconstruction in X-ray CT. In *Nuclear Science Symposium Conference Record*, volume 5, pages 2708–2710, 2005.

[6] D.L. Donoho. Compressed sensing. *Information Theory, IEEE Transactions on*, 52(4):1289–1306, 2006.

[7] Michael Elad and Michal Aharon. Image denoising via sparse and redundant representations over learned dictionaries. *IEEE transactions on image processing : a publication of the IEEE Signal Processing Society*, 15(12):3736–45, December 2006.

[8] M Feser, J Gelb, H Chang, H Cui, F Duewer, S H Lau, A Tkachuk, and W Yun. Sub-micron resolution CT for failure analysis and process development. *Measurement Science and Technology*, 19(9):094001, September 2008.

[9] Y. Q. Fu, A. Colli, A. Fasoli, J. K. Luo, a. J. Flewitt, a. C. Ferrari, and W. I. Milne. Deep reactive ion etching as a tool for nanostructure fabrication. *Journal of Vacuum Science*

and Technology B: Microelectronics and Nanometer Structures Technology, 27(3):1520, 2009.

[10] G T Gullberg, C R Crawford, and B M Tsui. Reconstruction Algorithm for Fan Beam with a Displaced Center-of-Rotation. *IEEE transactions on medical imaging*, 5(1):23–9, January 1986.

[11] Peng He, Hengyong Yu, Patrick Thayer, Xin Jin, Qiong Xu, James Bennett, Rachael Tappenden, Biao Wei, Aaron Goldstein, Peter Renaud, Anthony Butler, Phillip Butler, and Ge Wang. Preliminary experimental results from a MARS Micro-CT system. *Journal of X-ray science and technology*, 20(2):199–211, January 2012.

[12] Jiang Hsieh. *Computed tomography: principles, design, artifacts, and recent advances.* SPIE Publications, 2003.

[13] A.C. Kak and M. Slaney. *Principles of Computerized Tomographic Imaging.* Society of Industrial and Applied Mathematics, 2001.

[14] Willi A. Kalender. *Computed tomography: fundamentals, system technology, image quality, applications.* Wiley-VCH, 2011.

[15] Brian D Metscher. MicroCT for comparative morphology: simple staining methods allow high-contrast 3D imaging of diverse non-mineralized animal tissues. *BMC physiology*, 9:11, January 2009.

[16] Ryuta Mizutani, Akihisa Takeuchi, R Yoshiyuki Osamura, Susumu Takekoshi, Kentaro Uesugi, and Yoshio Suzuki. Submicrometer tomographic resolution examined using a micro-fabricated test object. *Micron*, 41(1):90–5, January 2010.

[17] Brian E Nett, Robert Brauweiler, Willi Kalender, Howard Rowley, and Guang-Hong Chen. Perfusion measurements by micro-CT using prior image constrained compressed sensing (PICCS): initial phantom results. *Physics in medicine and biology*, 55(8):2333–50, April 2010.

[18] Xiaochuan Pan, Emil Y Sidky, and Michael Vannier. Why do commercial CT scanners still employ traditional, filtered back-projection for image reconstruction? *Inverse problems*, 25(12):1230009, January 2009.

[19] D.L. Parker. Optimal short scan convolution reconstruction for fanbeam CT. *Medical Physics*, 9:254, 1982.

[20] Erik L Ritman. Micro-computed tomography-current status and developments. *Annual review of biomedical engineering*, 6:185–208, January 2004.

[21] J. D. Schiffbauer, S. Xiao, Kriti Sen Sharma, and G. Wang. The origin of intracellular structures in Ediacaran metazoan embryos. *Geology*, 40(3):223–226, January 2012.

[22] K. Sen Sharma, S. Seshadri, M. Feser, and G. Wang. Accurate Resolution Measurement for X-Ray Micro-CT Systems. In *AIP Conference Proceedings*, volume 1365, pages 337–340, 2011.

[23] Emil Y Sidky, Chien-min Kao, and Xiaochuan Pan. Accurate image reconstruction from few-views and limited-angle data in divergent-beam CT. *Journal of X-Ray Science and Technology*, 14:119–139, 2006.

[24] S.W. Smith. *Digital signal processing: a practical guide for engineers and scientists*. Newnes, 2003.

[25] Jiayu Song, Qing H. Liu, G. Allan Johnson, and Cristian T. Badea. Sparseness prior based iterative image reconstruction for retrospectively gated cardiac micro-CT. *Medical Physics*, 34(11):4476–4483, July 2007.

[26] Stuart R. Stock. *MicroComputed Tomography: Methodology and Applications*. CRC Press, 2008.

[27] Jie Tang, Brian E Nett, and Guang-Hong Chen. Performance comparison between total variation (TV)-based compressed sensing and statistical iterative reconstruction algorithms. *Physics in medicine and biology*, 54(19):5781–804, October 2009.

[28] Xiangyang Tang, Suresh Narayanan, Jiang Hsieh, Jed D Pack, Scott M Mcolash, Paavana Sainath, Roy a Nilsen, and Basel Taha. Enhancement of in-plane spatial resolution in volumetric Computed Tomography with focal spot wobbling - overcoming the constraint on number of projection views per gantry rotation. *Journal of X-ray science and technology*, 18(3):251–65, January 2010.

[29] Dong Wang. *A micro-scale method to associate the fatigue properties of asphalt binder, mastic and mixture*. PhD thesis, Virginia Polytechnic Institute and State University, 2011.

[30] Ge Wang and Ming Jiang. Ordered-subset simultaneous algebraic reconstruction techniques (OS-SART). *Journal of X-ray Science and Technology*, 12:169–177, 2004.

[31] Ge Wang, Tein-Hsiang Lin, Ping-chin Cheng, and Douglas M. Shinozaki. A General Cone-Beam Reconstruction Algorithm. *Ieee Transactions on Medical Imaging*, 12(3):486–496, 1993.

[32] Wei Xu and Klaus Mueller. Learning effective parameter settings for iterative CT reconstruction algorithms. In *Fully 3D Image Reconstruction in Radiology and Nuclear Medicine Conference*, number Cc, pages 251–4, Beijing, China, 2009.

[33] T Yamashita, Y Nabeshima, and M Noda. High-resolution micro-computed tomography analyses of the abnormal trabecular bone structures in klotho gene mutant mice. *The Journal of endocrinology*, 164(2):239–45, February 2000.

[34] Jiansheng Yang, Hengyong Yu, Ming Jiang, and Ge Wang. High-order total variation minimization for interior tomography. *Inverse Problems*, 26(3):035013, 2010.

[35] Wanneng Yang, Xiaochun Xu, Kun Bi, Shaoqun Zeng, Qian Liu, and Shangbin Chen. Adaptive region of interest method for analytical micro-CT reconstruction. *Journal of X-ray science and technology*, 19(1):23–33, January 2011.

[36] H Yu and G Wang. Compressed sensing based interior tomography. *Physics in medicine and biology*, 54(9):p2791–2805, 2009.

[37] G.L. Zeng. *Medical Image Reconstruction: A Conceptual Tutorial*. Springer, 2010.

[38] Li Zeng, Baodong Liu, Linghui Liu, and Caibing Xiang. A new iterative reconstruction algorithm for 2D exterior fan-beam CT. *Journal of X-ray science and technology*, 18(3):267–77, January 2010.

Chapter 3

Scout-view assisted interior micro-CT

Publication information

The manuscript: *Kriti Sen Sharma*, Christian Holzner, Dragoş M Vasilescu, Jin Xin, Shree Narayanan, Masoud Agah, E. A. Hoffman, Hengyong Yu, Ge Wang, "Scout-view assisted interior micro-CT", is slated to appear in the journal *Physics in Medicine and Biology*.

Author contributions

The contributions of the various authors are listed below:

- *Kriti Sen Sharma*[1]: Design and implementation of all reconstruction algorithms, phantom fabrication and scans, experimental design, manuscript writing
- *Christian Holzner*[2]: Phantom fabrication, scan of rock sample, experimental design, manuscript writing
- *Dragoş M Vasilescu*[3]: Scan of lung sample, experimental design, manuscript writing
- *Xin Jin*[4]: Coding framework for SART-TV
- *Shree Narayanan*[1] and *Masoud Agah*[1]: Phantom fabrication
- *E. A. Hoffman*[5]: Scan of lung sample, analysis of lung sample results
- *Hengyong Yu*[6] and *Ge Wang*[7]: Experimental design, manuscript writing

All authors contributed in terms of revising and improving the manuscript.

Author affiliations

1. Dept. of Elec. & Comp. Eng., Virginia Tech, Blacksburg, VA 24061, USA

2. Xradia Inc., Pleasanton, CA 94588, USA

3. UBC James Hogg Research Centre at the Heart & Lung Institute, St Paul's Hospital, Vancouver, B.C., V6Z 1Y6, Canada

4. Dept. of Eng. Phys., Tsinghua Univ., Beijing 100084, China

5. Dept. of Radiology, Univ. of Iowa, Iowa City, IA 52242, USA

6. Biomedical Imaging Division, VT-WFU School of Biomedical Eng. & Sciences, Wake Forest Univ. Health Sciences, Winston-Salem, NC 27157, USA

7. Biomedical Imaging Center, Rensselaer Polytechnic Institute, Troy, NY 12180, USA

3.1 Abstract

Micro computed tomography (micro-CT) is a widely-used imaging technique. A challenge of micro-CT is to quantitatively reconstruct a sample larger than the field-of-view (FOV) of the detector. This scenario is characterized by truncated projections and associated image artifacts. However, for such truncated scans, a low resolution scout scan with an increased FOV is frequently acquired so as to position the sample properly. This study shows that the otherwise discarded scout scans can provide sufficient additional information to uniquely and stably reconstruct the interior region of interest. Two interior reconstruction methods are designed to utilize the multi-resolution data without a significant computational overhead. While most previous studies used numerically truncated global projections as interior data, this study uses truly hybrid scans where global and interior scans were carried out at different resolutions. Additionally, owing to the lack of standard interior micro-CT phantoms, we designed and fabricated novel interior micro-CT phantoms for this study to provide means of validation for our algorithms. Finally, two characteristic samples from separate studies were scanned to show the effect of our reconstructions. The presented methods show significant improvements over existing reconstruction algorithms.

3.2 Introduction

A major limitation of computed tomography (CT) has been that the imaging field-of-view (FOV) needs to cover the entire sample. If this is not the case, i.e. the sample is larger than the FOV, projections are truncated in some or all of the views. Truncated projections have no unique reconstruction value [21]. Typically, the effect of truncated projections is seen in reconstructed images in the form of cupping artifacts at the edges (resulting in a loss of contrast in features), and a difference in CT numbers (a DC bias) when compared with global

reconstructions containing the whole sample in the FOV [5, 11, 42]. High-resolution micro-CT scanners employ projection x-ray imaging using laboratory sources to achieve resolution on the order of 1 μm [9, 27]. In such scanners, the FOV varies between 0.5 mm and 1 cm, with higher resolution at smaller FOV-s [32]. Hence truncated projections are a very common problem, particularly as interest in higher resolution imaging increases, and the option of trimming the sample to an appropriate size matching the FOV is not desirable.

Over the years, multiple techniques have been proposed to circumvent the interior tomography problem; some of which are listed here:

1. In the field, the most commonly used approach is based on sinogram extension techniques [14, 17, 37]. However the extension techniques are necessarily approximation methods, and do not achieve exact reconstruction.

2. A second group of techniques employ a combination of back projection of the first derivative and the 2D Hilbert transform [7, 22]; however they deal with a certain class of truncated projections only, and are unstable in case of completely interior truncation, where the region of interest (ROI) is fully inside the object [5].

3. Lambda tomography accurately locates discontinuities inside the ROI [8, 44], but does not provide CT number information.

4. A compressed sensing (CS) based technique [42] has been shown to achieve accurate interior reconstruction in many imaging modalities including cardiac CT [46], MRI [40], electron microscopy [10]. However the iterative procedure is highly time consuming and is not yet commercially viable [25].

This paper introduces two novel interior reconstruction methods, namely 'scout-interpolation' and 'scout-reconstruction' , that use only a handful of scout views as additional information. The new methods are compared with two previously reported methods – 'truncated-FBP', which is a sinogram extension technique [12], and 'sequence subsets SART-TV (SS-SART-TV)', a compressed sensing aided reconstruction algorithm [42, 23].

Scout views are global projections that encompass the entire object. Before any interior micro-CT scan, some scout projections are typically acquired as they help to place the sample within the FOV, and to align the sample along the axis of rotation. However the scout views are usually discarded. In this study, we show how the scout views may be used to mitigate interior reconstruction artifacts. Also a "scout tomography" consisting of just a few global views at low resolution may easily be acquired just for the purpose of accurate interior reconstruction.

Multi-resolution acquisition (or "zoom-in" tomography) uses a low resolution scan to fill up the incomplete information in high-resolution truncated projections [18, 20, 24, 28, 35]. Most previous multi-resolution approaches placed severe restrictions on the relative geometry of

the two scans, making them difficult to undertake experimentally [5, 16]. No such restrictions are required in this study. In [18], two multi-resolution methods were proposed and compared to the gold-standard (the "data-completion" method) – all three techniques had no restrictions on the relative geometries. Yet, like most multi-resolution techniques thus far, their methods required the low-resolution scan to be adequately sampled over the angular range. In contrast, we only require a minimal set of global or scout views, with no significant time impact. Of our two proposed methods, scout-interpolation is an extension of multi-resolution acquisition techniques, while scout-reconstruction enhances the data-completion method [18] by incorporating compressed sensing aided reconstruction in the low-resolution reconstruction step.

In [2, 43], reconstruction schemes were developed which used only two scout views to eliminate interior reconstruction artifacts. The reconstruction methods described in those two studies were purely iterative techniques. However, CT manufacturers tend to prefer the traditional filtered back projection (FBP) algorithm over iterative reconstruction algorithms [25]. Two important reasons for this preference are that, (1) users are familiar with FBP in terms of reconstruction parameters, achievable image quality etc., and (2) manufacturers have already developed optimized image reconstruction chains using FBP, and the migration to purely iterative reconstruction requires significant spending and engineering effort. The methods in this paper employ FBP for the final reconstruction, and thus, new user training is not required. Though one of the two algorithms in our paper employs an iterative reconstruction step, the additional computational burden is very low as shown in Sec. 3.5. Thus, the proposed algorithms may be easily integrated into existing reconstruction chains.

In most previous studies on interior reconstruction, interior scans were simulated by numerically truncating real global projections [28, 33, 42]. Such an approach is essential to verify new algorithms by comparison to the ground truth. The presented study goes one step further and investigates scans where the truncated projections and scout views were acquired in separate scans with two different magnification images using two different size detectors. For such multi-resolution scans, various factors come into play (e.g. registration, detector differences), that were handled by proposed interior reconstruction methods.

Furthermore, novel interior micro-CT phantoms were fabricated using conventional lithography techniques, and "off-the-shelf" items. Firstly, a phantom for interior scans should be larger than the FOV of the detector. Then it should have known geometric structures embedded within the interior ROI, so as to allow proper system characterization. In clinical CT where resolution is in the millimeter range, such geometrically well-defined structures (e.g. wire, spherical, and square phantoms) are commercially available [13]. In high-resolution micro-CT, the most commonly used phantoms are thin test patterns fabricated by semiconductor fabrication techniques, but they allow system characterization in the projection domain only [29]. 3D micro-CT phantoms allowing quantification in reconstructed slices [19] have been difficult to fabricate, or are not yet readily available [30]. Most importantly, previously reported micro-CT phantoms were not suitable for characterizing interior reconstruction, and thus, new phantoms were fabricated for this study.

The remainder of the paper is organized as follows. The micro-CT phantoms, micro-CT samples, scan protocols, and interior reconstruction algorithms are detailed in Sec. 3.3. Section 3.4 discusses the results obtained on micro-CT phantoms and samples. Finally, Sec. 3.5 concludes the paper with a discussion and summary.

3.3 Materials and Methods

3.3.1 Micro-CT scanner

All scans were carried out on a MicroXCT-400 scanner from Xradia Inc. (Pleasanton, CA). This scanner employs a commercially available microfocus x-ray source to achieve projection imaging. The x-rays are absorbed by a scintillator and converted to visible light – a microscope objective then focuses this light onto a 2048×2048 CCD [9]. Depending on the magnification lens used, the effective detector pixel size may be varied between 27 μm and 0.3 μm. Furthermore, the geometric magnification of the system may be modified by moving the source and detector stages according to the needs of the scanned specimen. The sample can be translated in the x-y-z directions on a high precision stage. The translation stage is mounted atop the rotation stage, and this allows the selection of any axis of rotation within a sample. The scan protocols used in this study are detailed in Sec. 3.3.3.

3.3.2 Micro-CT phantoms and samples

Two interior micro-CT phantoms, and two typical micro-CT samples were scanned as part of this study.

Interior micro-CT phantom I

Wafers of micro-gas chromatography devices consisting of an array of micro-pillars were first fabricated [1]. Next, ~ 300 μm wide strips were diced off to create structures that fit within FOV of a high resolution micro-CT [30]. These structures are marked by white arrows in Fig. 3.1A. To create an interior phantom, the micro-pillar strips were bundled with other sub-mm structures – specifically, PMMA micro-capillary tubes (Paradigm Optics, Inc., Vancouver, WA) of varying diameter and material (two such tubes are marked by black arrows with white borders in Fig. 3.1A). White duct tape and Scotch tape (3M Inc., Maplewood, MI) were used as packing material, and also provided additional attenuating material. The bundle of Fig. 3.1A has a diameter of ~ 6.7 mm that is considerably larger than the ~ 2.8 mm FOV of 1.4 μm pixel size detector used to acquire interior projections. This bundle is referred to as interior micro-CT phantom I. The phantom had a circular cross-section, and the objects of interest (i.e. the micro-pillar strips) were placed near the center of the phantom.

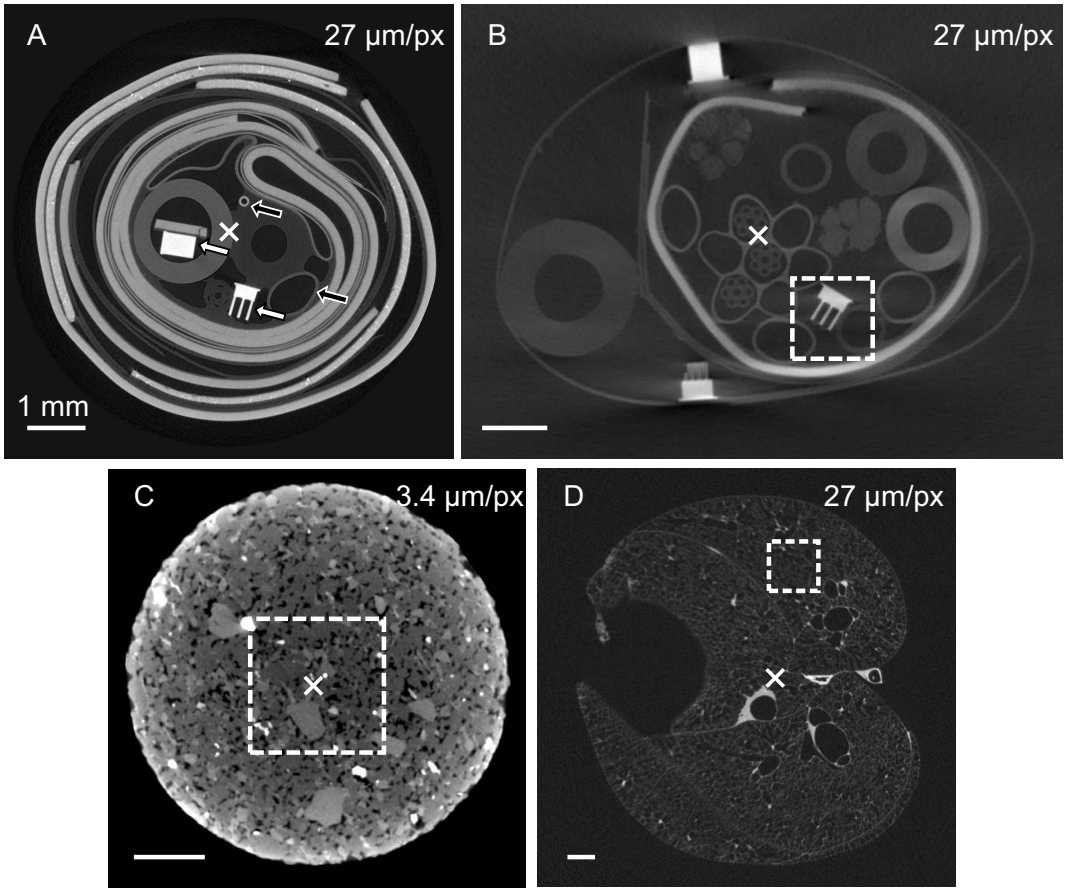

Figure 3.1: Samples used in characterizing interior micro-CT. (A) Interior micro-CT phantom I. White arrows mark angular structures prepared by semiconductor fabrication techniques, and black arrows with white borders mark two of many micro-capillary tubes. (B) Interior micro-CT phantom II. (C) Rock sample. (D) Mouse lung. Interior scan ROI-s are marked by white squares. White cross-hairs depict the axis of rotation of global scans, while axis of rotation of interior scan passes through center of the white squares. The used detector pixel sizes are marked for global scans at top-right corner. For samples B, C and D, interior scans were acquired using 1.4 μm pixel size detector. All scale bars are 1 mm.

Interior micro-CT phantom II

Using sub-mm structures described above in Sec. 3.3.2, duct tape, and Scotch tape, another bundle was created as shown in Fig. 3.1B. It had a non-circular cross-section, and a region of interest quite far from the geometric center of the phantom (marked by dotted white square in Fig. 3.1B). This bundle is referred to as interior micro-CT phantom II.

Rock sample

The characterization of carbonate rock pore structure is of importance in the sciences of natural resource extraction and carbon sequestration. From the pore structure, rock properties such as porosity, pore connectivity, permeability and capillary pressure can be derived and used in subsequent analysis. Results of such methods depend upon accurate 3D imaging and segmentation of rock samples, frequently acquired through interior tomography. Fig. 3.1C shows a reconstructed slice from a global scan of an exemplary carbonate rock sample.

Mouse lung

In recent morphometric studies of murine lungs, high-resolution micro-CT scans were carried out on perfusion fixed mouse lungs [38]. A complex imaging protocol was developed [39] in which the entire lung was first imaged with the 27 μm/px detector of the Xradia MicroXCT-400 scanner. A reconstructed slice is shown in Fig. 3.1D. At this magnification the entire lung fit in the FOV and enabled the precise selection of coordinates at which high resolution scans could be performed. The high-resolution interior scan was performed using the 1.4 μm/px detector, and enabled the 3D reconstruction and quantitative study of the acinar structures, the basic ventilatory units in the lung that consist of a complex grape like structure [38]. Such a multi-resolution study design is essential for imaging fragile biological sample where the morphometry of internal structures can be altered by physical dissection as traditionally done for histological studies.

3.3.3 Scan protocols

For all samples listed in Sec. 3.3.2, global scans were first carried out. Reconstructed slices for the four samples are shown in Fig. 3.1. The detector pixel size used in each such scan is marked at the top-right corner of all images in Fig. 3.1 (27 μm pixel size detector for all samples, except rock sample, where 3.4 μm pixel size detector was used). 1500-1800 projections were acquired for each global scan so as to allow sufficient projection sampling and low reconstruction noise – the exact number of projections used are listed in Tab. 3.1. Reconstructions of global scans were used as a ground truth for comparing interior reconstruction results.

Table 3.1: Scan settings for study on scout-view assisted interior tomography. Scans were acquired on Xradia MicroXCT-400 scanner (RA = rotation axis, meas. = measurement). Four samples (A) - (D) correspond to samples in Fig. 3.1.

Scan Parameters	**(A) Phantom I**	**(B) Phantom II**		**(C) Rock**		**(D) Lung**	
Global (***G***) / Interior (***i***)	***G***	***G***	***i***	***G***	***i***	***G***	***i***
Detector pixel size (μm)	27	27	1.4	3.4	1.4	27	1.4
Binning	2	2	2	1	1	1	2
Number of detector pixels	1024	1024	998	2022	2006	2048	998
Source-RA distance (mm)	26.0	26.0	26.0	19.0	8.0	59.9	55.0
Detector-RA distance (mm)	164.9	99.9	30.0	5.5	5.5	64.7	18.0
Field-of-meas. (dia., mm)	7.60	11.53	1.24	5.20	1.58	26.87	2.01
X-ray energy (kV)	40	60	60	70	65	40	40
Current (μA)	100	100	100	85	83	200	200
Exposure time (sec)	3.0	0.5	20.0	2.2	3.4	1.8	8.0
Start angle (degrees)	-101	-107	-92	-180	-180	-107	-92
End angle (degrees)	101	107	92	180	180	107	92
Number of projections	1500	1500	1500	1800	2700	1648	1228

Next, scans targeting an interior ROI were acquired. The interior scans were acquired using 1.4 μm pixel size detector each time, and the ROI is marked by white border in subfigures 3.1B-D.

Truncated sinogram

The global sinogram of the central slice of interior phantom I is shown in Fig. 3.2A. Global projections were truncated to simulate corresponding interior data, as shown in Fig. 3.2B. The truncated data are perfectly co-registered with global data and thus allow straightforward comparison of various interior reconstruction algorithms, and omit other sources of reconstruction differences. The truncation ratio (higher ratio signifying more truncation) was calculated as below:

$$\text{Truncation ratio} = 1 - \frac{\text{Length of truncated projection}}{\text{Length of global projection}} \tag{3.1}$$

For the other samples, interior scans provided already truncated views and sinograms.

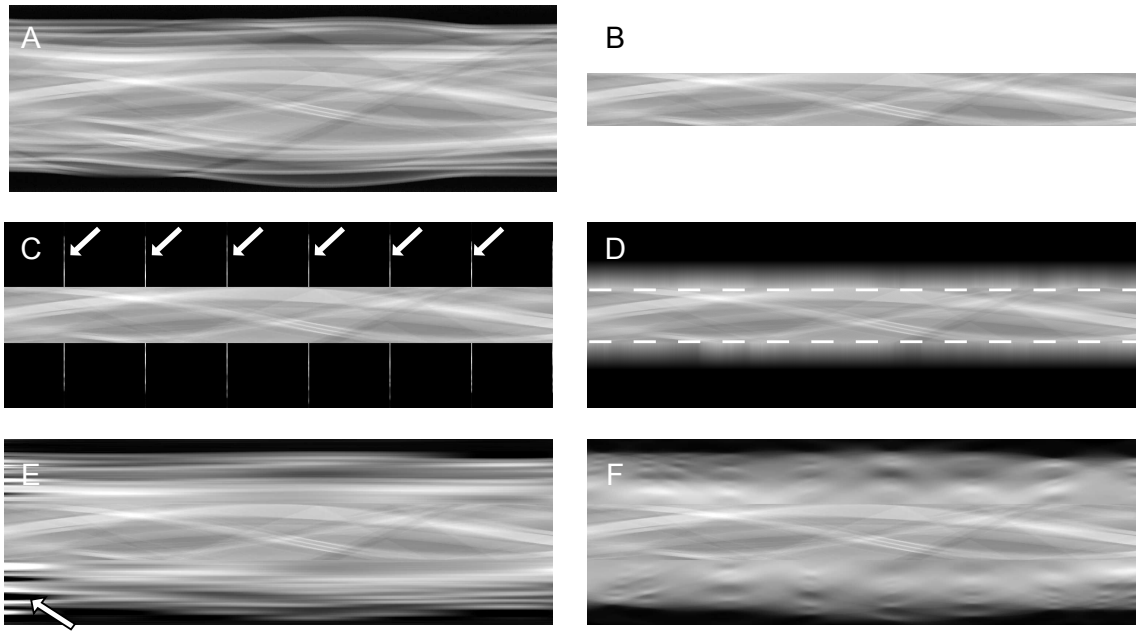

Figure 3.2: Sinograms demonstrating steps in interior reconstruction. Sinograms are those of interior micro-CT phantom I. (A) Global sinogram. (B) Truncated sinogram. (C) Truncated sinogram with six global scout views marked with white arrows. (D-F) Sinograms for the different reconstruction algorithms – (D) truncated-FBP (Sec. 3.3.4, borders of original sinogram marked by dotted lines), (E) scout-interpolation (Sec. 3.3.4), and (F) scout-reconstruction (Sec. 3.3.4). An example of erroneous extrapolation (Sec. 3.4.1) is marked by an arrow in subfigure E.

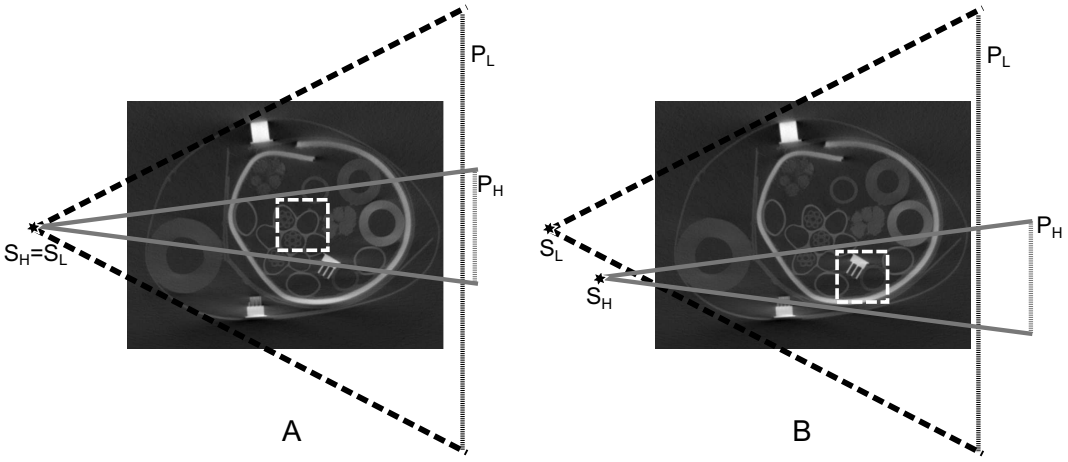

Figure 3.3: Two configurations of high-resolution interior projections. The high resolution interior projection (P_H) may have two configurations w.r.t. low-resolution scout views (P_L). (A) is a special configuration where only the detector changes between interior and scout projections i.e. source-position (S_H and S_L), detector to rotation-axis distance, axis of rotation all remain constant. (B) is a more general configuration where interior and scout projections are acquired independently.

Scout views

While the global scans were acquired at large number of projection angles, the entire global scan was not used as additional information for improved interior reconstruction. From the large set of global projections, two to eight views were selected as scout views and used as additional information. The scout views were selected at equal angular sampling as shown for the six scout view case in Fig. 3.2C. The small number of additional scout views do not represent an additional scan burden and yet significantly reduce interior reconstruction artifacts, as we will show subsequently.

There are two possible configurations for global scout views w.r.t. the interior scan, and these are depicted in Fig. 3.3. First, the global scout views may be acquired at the same scan geometry (i.e. same axis of rotation, source distance, detector distance etc.) as the interior scan. Such a scan is depicted in subfigure 3.3A, and occurs in real scans when the only change between the scans is the change of the detector. Second, the interior scan and global views may be acquired at completely different geometries. As depicted in subfigure 3.3B, the two source positions (S_H and S_L) and detector positions are different; also the axes of rotation are different. In our samples, the scan and subsequent truncated projections for sample A in Fig. 3.1 obey the former configuration, while the data acquisition for samples B, C, D in Fig. 3.1 obey the latter configuration.

3.3.4 Interior reconstruction algorithms

The Xradia MicroXCT-400 scanner used in this study employs scanning in cone-beam geometry. In the presented study, only the central slice of the cone-beam (which can be described by fan-beam geometry) was considered, so as to allow faster execution by limiting the problem to 2D [6]. The main motivation of this study was to introduce two new interior reconstruction algorithms and compare them with existing techniques; the extension to cone-beam was left as a future task. The trend in results observed by fan-beam reconstruction on the central slice is expected to be same for all slices when reconstructed by cone-beam reconstruction; it is well known that practical Feldkamp-type cone-beam reconstruction methods are based on modified fan-beam reconstruction formulas [41].

Four algorithms were used to reconstruct the truncated projections. The first two methods – truncated-FBP (Sec. 3.3.4) and sequence subsets SART-TV (Sec. 3.3.4) are previously reported methods that use only the truncated sinogram. Scout-interpolation (Sec. 3.3.4) and scout-reconstruction (Sec. 3.3.4) are two new methods introduced in this paper, and use truncated sinograms as wells as scout views. Further details of the algorithms are explained below.

Truncated-FBP

If FBP is directly applied on a truncated projection (where unknown projection values are replaced by zeros), the reconstructed image suffers from severe cupping artifacts, and a loss of contrast [5, 37]. To reduce this problem, a Gaussian extrapolation technique [12] was employed, where the border value of the truncated sinogram was rolled off to zero by a Gaussian function. Also, as the knowledge of actual object boundary is not provided to this algorithm, the extrapolation range is selected ad hoc. The resulting sinogram is shown in Fig. 3.2D. FBP was employed on the Gaussian extrapolated sinogram to yield the reconstructed image. This process of FBP after Gaussian extrapolation of the sinogram is henceforth referred to as 'truncated-FBP' in the paper.

Sequence subsets SART-TV (SS-SART-TV)

In [42], compressed sensing based SART-TV reconstruction was shown to provide higher accuracy for interior reconstruction as compared to FBP. Each iteration of SART-TV consists of one step of SART (simultaneous algebraic reconstruction technique), and one step of total variation (TV) minimization. In this study, while the TV minimization step was kept the same, the SART step was replaced by sequence subsets SART (SS-SART) [23, 36]. SS-SART allowed the image update to progress in a very stable fashion, and also achieved better image quality at a lower number of iterations [15].

The starting point for SS-SART-TV reconstruction is the truncated sinogram without any

extrapolation (as in Fig. 3.2B), and the initial image is composed of zeros. Only three parameters are required to be set in this process: relaxation parameter λ of SART at 0.8, α parameter for TV minimization at 0.2, and number of TV iterations at 5. In our tests, this combination or parameters yielded good results for all four datasets.

Scout-interpolation

For the scan configuration of Fig. 3.3A, global scout views and interior scan are acquired at identical source-detector positions and at the same axis of rotation (only the detector is changed). Reconstruction by 'scout-interpolation' is carried out as explained below.

1. Scout views $P_L(m\tau_L, \theta_i)$ $\{m = -M, \dots M; i = 1, 2, \dots N_{\text{Scouts}}\}$ are originally acquired at lower magnification detector pixel width τ_L. The scout views are up-sampled by cubic spline interpolation to the detector pixel width τ_H $(\tau_H < \tau_L)$ of the high-resolution interior scan. This yields $P'_{LH}(n\tau_H, \theta_i)$ $\{n = -N, \dots N;\ i = 1, 2, \dots N_{\text{Scouts}}\}$.

2. Next, since the scout views are acquired at only a few projection angles i.e. $N_{\text{Scouts}} << N_{\text{Proj}}$, a cubic spline interpolation and extrapolation step (MATLAB, The MathWorks, Inc., Natick, MA) estimates the projections at all angles of the interior projections. This yields $P_{LH}(n\tau_H, \phi_j)$ $\{n = -N, \dots N; j = 1, 2, \dots N_{\text{Proj}}\}$.

3. The portion of the sinogram corresponding to the ROI is replaced by the high-resolution interior scan $P_H(n\tau_H, \phi_j)$ $\{n = -P, \dots P; j = 1, 2, \dots N_{\text{Proj}}\}$, where $P < N$. This step yields a sinogram like that in Fig. 3.2E. To blend the sinograms without abrupt change in intensity, a sinogram equalization step is carried out as described in [4].

4. The resulting sinogram is reconstructed using FBP.

Scout-reconstruction

When the global scout views and interior scan do not share similar geometry (as in Fig. 3.3B), the scout-interpolation method cannot be applied. We developed a novel 'scout-reconstruction' method as explained below. Fig. 3.4 also provides a schematic of this algorithm (with the steps below being marked in the figure).

1. High-resolution interior scan P_H is acquired at source position S_H, and with detector pixel width τ_H.

2. Global scout views P_L are acquired from source position S_L, using a lower magnification (with detector pixel width τ_L, where $\tau_H < \tau_L$).

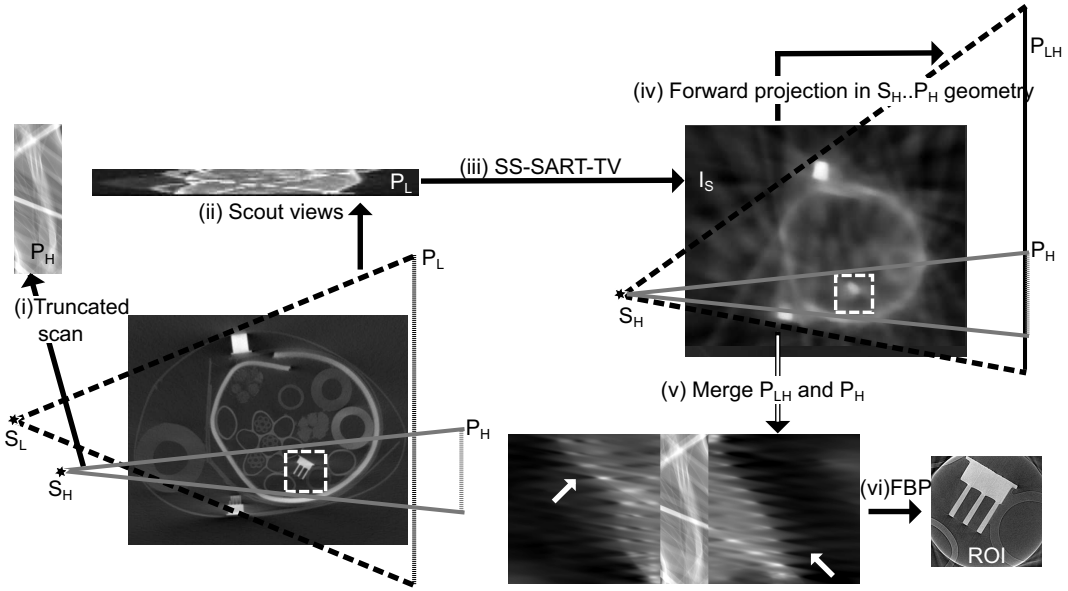

Figure 3.4: Graphic depicting scout-reconstruction method of Sec. 3.3.4. (i) High-resolution interior scan (P_H) is acquired from source position S_H. (ii) A set of scout views (P_L) is acquired from source position S_L. (iii) SS-SART-TV is carried out on scout views P_L. (iv) Reconstructed image is forward projected in high-resolution geometry to get sinogram P_{LH}. (v) P_{LH} and P_H are merged before (vi) final reconstruction step by FBP.

3. Using only sinogram P_L composed of scout views, SS-SART-TV is carried out (all parameters same as in Sec. 3.3.4 , except that 20 TV iterations are performed in each TV minimization step).

4. The resultant image I_S is forward projected from source position S_H in the high-resolution geometry (still at detector pixel width τ_L of low-resolution detector, but at all projection angles of the interior scan).

5. Each column of the forward projected sinogram P_{LH} is up-sampled to the high-resolution pixel width τ_H. The forward-projected and up-sampled sinogram contains some irregularities (e.g. striped patterns marked by white arrows in figure), but this does not affect final reconstruction adversely. Next, the region corresponding to the ROI is replaced by real interior projection data P_H. Sinogram equalization according to [4] is performed prior to blending of sinograms so as to avoid abrupt change in intensity.

6. Finally, the merged sinogram is reconstructed using FBP.

Step (4) requires an accurate registration between the global and interior scans. This is easily achieved as the Xradia MicroXCT-400 records the exact location of the iso-center in terms of world co-ordinates for both the scans.

3.4 Results

3.4.1 Results: Interior micro-CT phantom I

Reduction of interior reconstruction artifacts

Global projections were numerically truncated up to truncation ratios of 0.3, 0.4, 0.5, 0.6, 0.7 and 0.8, and then reconstructed using the four methods listed in Sec. 3.3.4. A line profile was drawn across the reconstructed slice as shown in Fig. 3.5C. The various line profiles at different truncation ratios and for each reconstruction algorithm are compared in Fig. 3.5. Subfigure A compares the line profiles for truncated-FBP with global FBP (the ground truth). It is easily seen that as the truncation increases, the DC bias and cupping around the edges also increases. In subfigure B comparing SS-SART-TV, it is observed that DC bias and cupping artifacts exist, but are much lower than truncated-FBP. In both subfigures C and D, scout-interpolation and scout-reconstruction results using seven scout views are shown. The reconstruction profiles for both scout-assisted methods match with the ground truth at all truncation ratios. Also the residuals for scout-interpolation and scout-reconstruction w.r.t. the ground truth were plotted in Figs. 3.5E and F respectively. The residuals for both these methods lie in the sub 1% range.

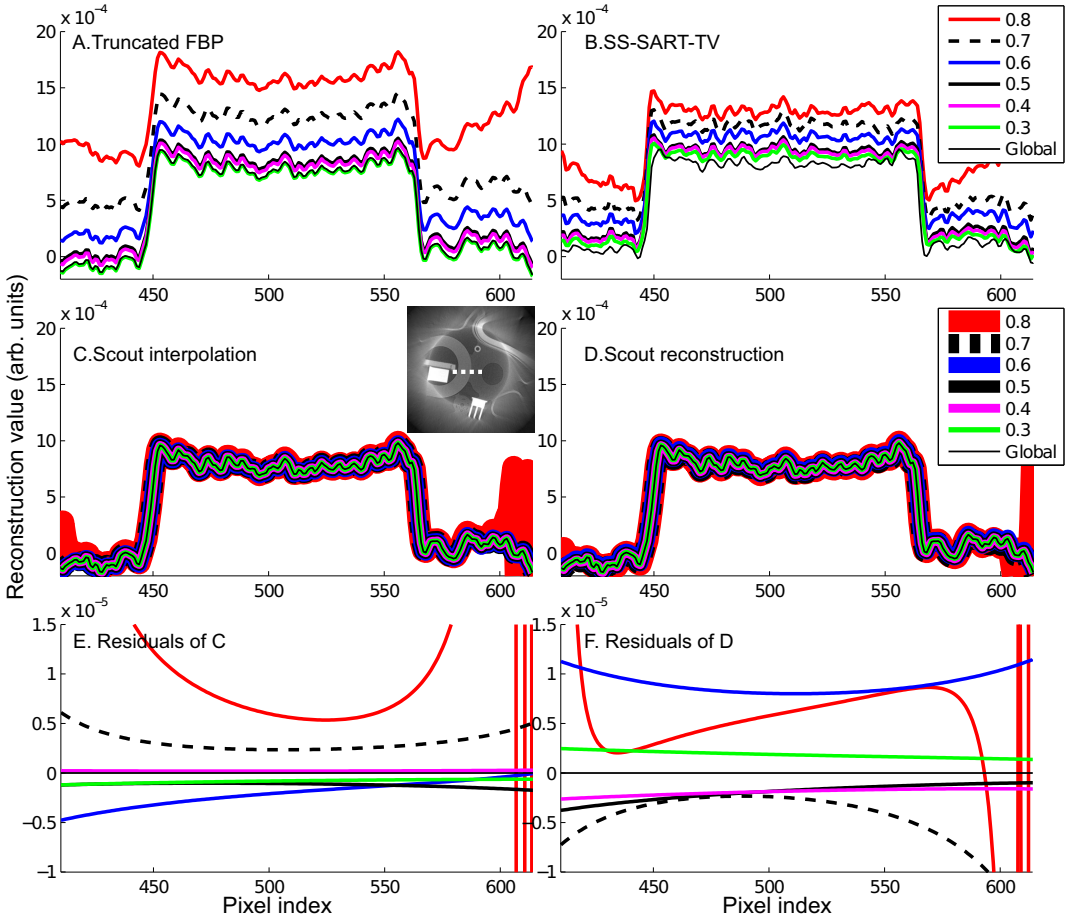

Figure 3.5: Line profiles for interior reconstruction algorithms. Horizontal line profiles are plotted across line marked in subfigure C, for various truncation ratios and for various interior reconstruction algorithms – (A) truncated-FBP, (B) SS-SART-TV, (C) scout-interpolation, and (D) scout-reconstruction. (E) and (F) plot residuals of subfigures C and D respectively, w.r.t. ground truth. Legend in B corresponds to A, B, E and F; legend in D corresponds to C and D (plots in C and D have been drawn thicker to highlight the fact that all profiles overlap).

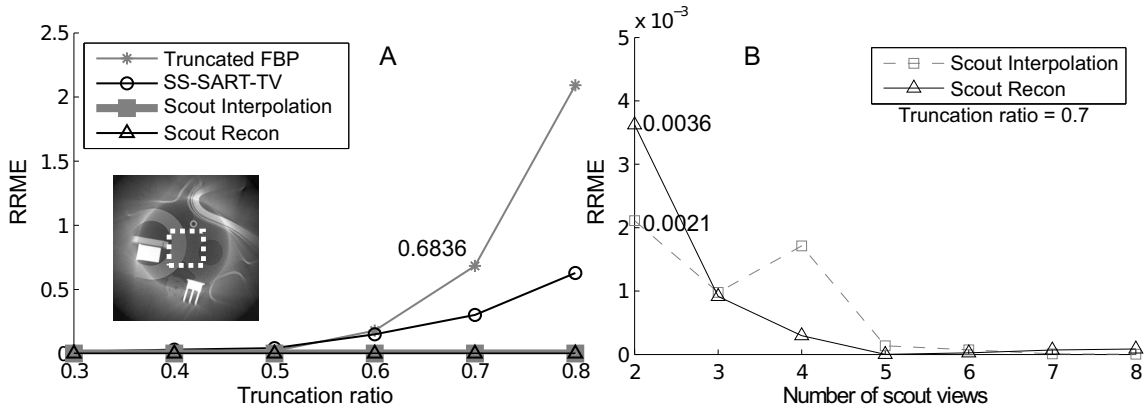

Figure 3.6: Relative root mean square error (RRME) for interior reconstruction. For the interior micro-CT phantom I, RRME w.r.t. global FBP was calculated across ROI marked by square. (A) RRME at different truncation ratios for different algorithms. Number of scout views used is seven in each case. (B) RRME with different number of scout views (at fixed truncation ratio of 0.7) for scout-interpolation and scout-reconstruction. The y-axis in two graphs are scaled differently.

Next the relative root mean square error (RRME) between reconstruction of truncated sinogram and ground truth was calculated according to [34]. The area in which RRME was calculated, corresponds to the ROI of sinogram truncation ratio of 0.8, and is shown in Fig. 3.6A inset. The error values were plotted in Fig. 3.6A. Among the four reconstruction algorithms, truncated-FBP has the highest error. While the error by truncated-FBP is low at smaller truncation ratios, RRME becomes significant when the truncation ratio is higher than 0.5. RRME for SS-SART-TV is always lower than for truncated-FBP. RRME is almost negligible when using scout-interpolation or scout-reconstruction, and this is true at all truncation ratios.

Within the scout-interpolation scheme, if the start-angle (or end-angle) of the scout views is higher than (or lesser than) the start-angle (or end-angle) of the interior scan, extrapolation needs to be carried out in Step (ii) of Sec. 3.3.4. It was observed that the extrapolation step is more prone to error (an example of erroneous extrapolation is marked by an arrow in Fig. 3.2E). In case of a tomography acquired over an angular range of 360°, the periodicity of the sinogram can be exploited to reduce such errors. However most scans in this study were acquired over a short-scan range [26] (see Tab. 3.1), and such periodicity could not be exploited. As a simple alternative to reduce the extrapolation errors, the start- and end-angles of the scout views may be selected as close to the corresponding values for the interior scan as possible.

Number of scout views

In the next study, the number of scout views was varied between two and eight, while keeping the truncation ratio constant at 0.7. RRME for scout-interpolation and scout-reconstruction methods are plotted in Fig. 3.6B. Even with two scout views, the RRME by scout-assisted methods (0.0021 for scout-interpolation, and 0.0036 for scout-reconstruction, see Fig. 3.6B) is far lower than the corresponding value for truncated-FBP (0.6836, see Fig. 3.6A).

For the scout-interpolation method, the RRME, in general, decreases with more scout views. But an abrupt change in this trend is observed at four scout views. This is attributed to the variability in interpolation depending on scout locations. For the scout-reconstruction method, the RRME always decreases when more scout views are available. This shows that scout-reconstruction method is more robust and stable than scout-interpolation. For both methods, though two scout views significantly reduce the RRME when compared with truncated-FBP, the RRME falls by another degree of magnitude when five or more scout views are used.

3.4.2 Results: Interior micro-CT phantom II

The scan of the second interior micro-CT phantom of Fig. 3.1B provides real interior projections. In this case, the center of rotations of interior and global scans are completely different. Thus, the scout-interpolation method of Sec. 3.3.4 is not applicable here. Only the scout-reconstruction method was tested for this sample.

Firstly, the reconstruction of the global scan cropped to the ROI of the interior scan is show in Fig. 3.7A. The image was up-sampled at the pixel width of high-resolution interior scan to allow easier comparison. Using the truncated-FBP algorithm, interior projections were reconstructed to yield Fig. 3.7B. A cupping artifact around the edges is easily observed. Finally, scout-reconstruction method of Sec. 3.3.4 was applied using 2, 4, 7, or 100 global scout views. Fig. 3.7C is reconstructed by using seven global scout views – there is almost no cupping artifact.

Line profiles across the dotted line in Fig. 3.7A are plotted in Fig. 3.7D for global FBP, truncated-FBP, and scout-reconstruction using 2, 4, 7, and 100 global scout views. The line plots show that truncated-FBP does not match global FBP, while scout-reconstruction does. This plot also demonstrates the variation in scout-reconstruction results when using different number of scout views. Even with two scout views, the line profile is almost identical to global FBP value. There is a minor change in the line profile as number of scouts is increased to four. When seven scout views are used, the line profile stabilizes, and is identical to scout-reconstruction result using 100 scout views.

In the following studies (sections 3.4.3 and 3.4.4), seven scout views are used as additional information. As seen in Fig. 3.7D, this allows reduction of DC bias and cupping artifact,

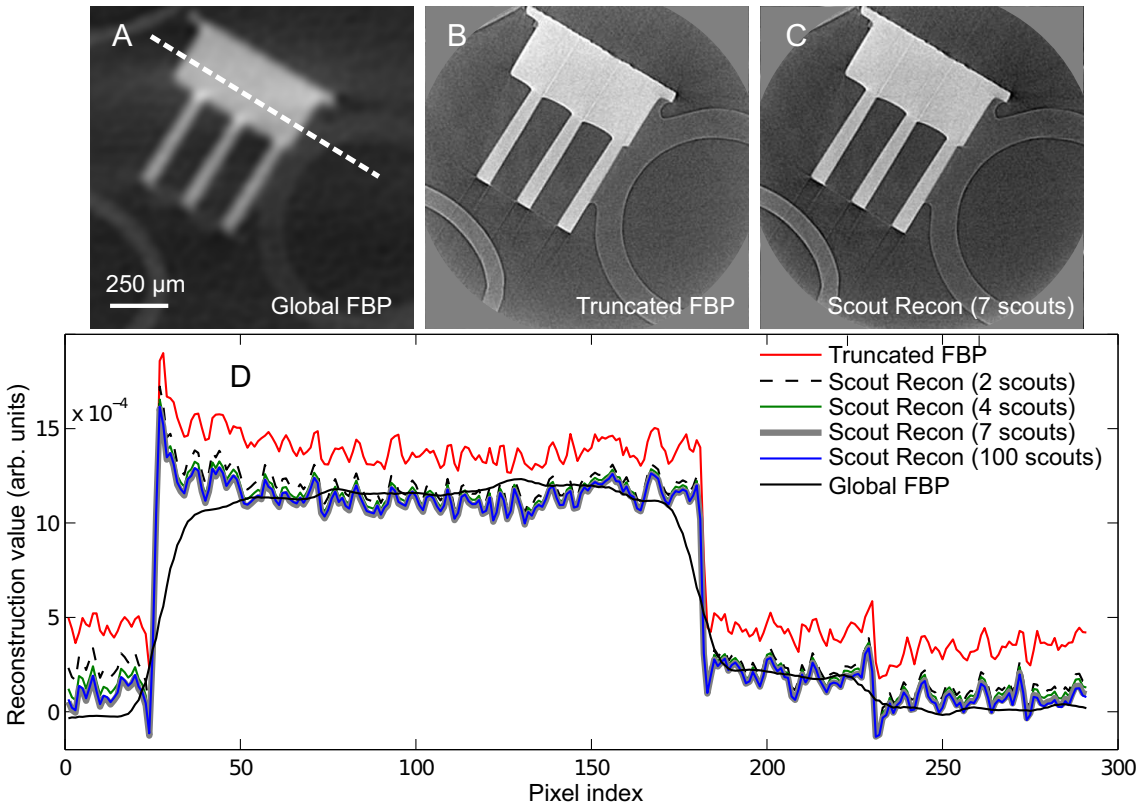

Figure 3.7: Interior reconstruction results of interior micro-CT phantom II. (A) Interior ROI from FBP of low-resolution global scan is up-sampled to pixel-size of high-resolution interior scan, and serves as a reference. Interior ROI reconstructed by (B) truncated-FBP, and (C) scout-reconstruction method. (D) Line plots comparing truncated-FBP, scout-reconstruction, and global FBP. Line plots also show variation in scout-reconstruction result when available number of scout views is 2, 4, 7, or 100.

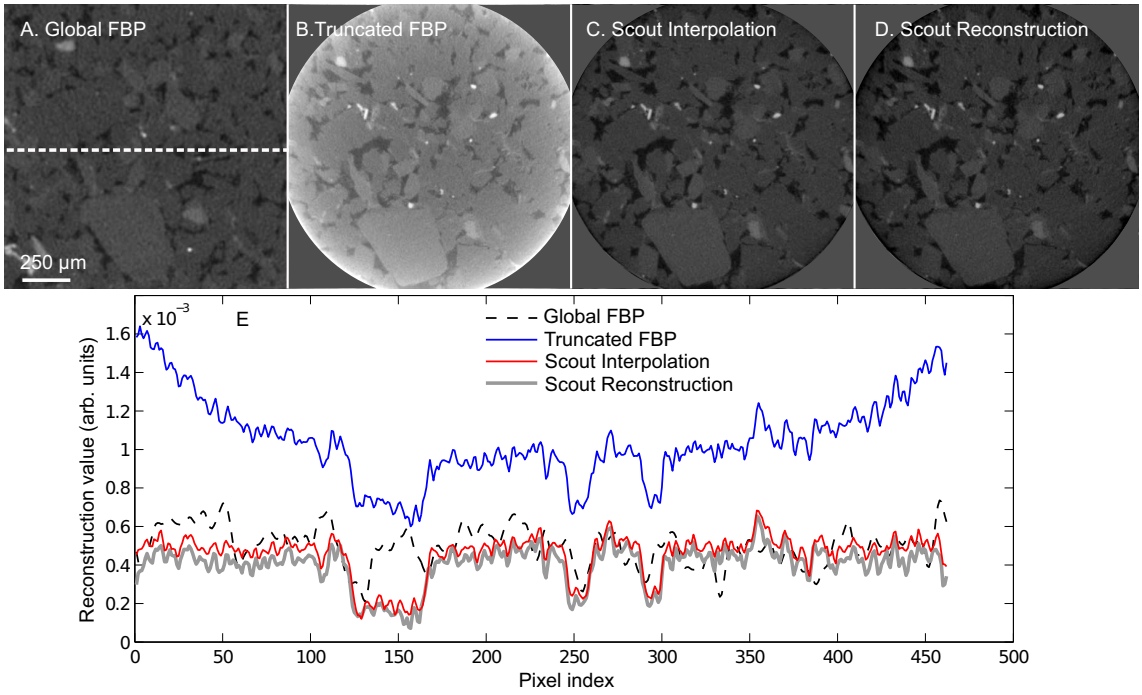

Figure 3.8: Results on rock sample. (A) Interior ROI from FBP of low-resolution global scan is up-sampled to pixel-size of high-resolution interior scan, and serves as a reference. Reconstruction of interior ROI by (B) truncated-FBP, (C) scout-interpolation, and (D) scout-reconstruction techniques. (E) Plot of line profiles across white dotted line in subfigure A.

while posing a very minor scanning overhead.

3.4.3 Results: Rock sample

The rock sample was scanned globally at 3.4 μm detector pixel size, followed by an interior scan at 1.4 μm detector pixel size. The global sinogram was reconstructed by traditional FBP. The interior ROI was cropped out and up-sampled to pixel width of interior scan in the same way as Sec. 3.4.2; the resultant image is shown in Fig. 3.8A. Next, the result of truncated-FBP is shown in Fig. 3.8B, where a DC bias and cupping artifact are clearly visible.

Axis of rotation of interior and global scans were identical for this sample. However Tab. 3.1 shows that the source-to-rotation axis distances are different – 19 mm in the global scan, and 8 mm in the interior scan. Ideally, the scan setting of Fig. 3.3A is not obeyed, and as such, the scout-interpolation method cannot be employed. However the main role of the scout views is to provide realistic projection values just outside the truncated projection data. As

a very rough approximation, the global projections acquired at 19 mm were used as scout views to extrapolate the interior projections acquired at 8 mm. This approximation was possible mainly because the axes of rotation were identical. The reconstructed slice is shown in Fig. 3.8C, and no cupping artifacts were observed. Finally, the scout-reconstruction algorithm was employed, and the reconstructed slice is in Fig. 3.8D. No cupping artifact was observed.

Profiles were taken across the line marked in Fig. 3.8A, and plotted in Fig. 3.8E. When compared with the global reconstruction line profile, the cupping artifact of truncated-FBP is evident around the left and right edges of the plot. Both the scout-interpolation and scout-reconstruction methods provided a much better match to the global reconstruction, though exact feature-to-feature correspondence does not exist. An exact feature-to-feature correspondence was observed in Fig. 3.7D for the interior phantom II because it had very coarse and regular features. For the rock sample, such an exact correspondence is not possible to achieve because the global scan is carried at much lower resolution than the interior scan, and the sample contains highly detailed features.

3.4.4 Results: Mouse lung

For the mouse lung sample of Fig. 3.1D, the global sinogram was reconstructed by traditional FBP, and the interior ROI (after up-sampling to the pixel size of the interior scan) is displayed in Fig. 3.9G. In this image, the features inside the interior ROI are not clearly distinguishable because the resolution of the global scan is not sufficient to resolve the detailed features of the mouse lung.

The interior scan was performed at a different axes of rotation than the global scan. The scout-interpolation method was not applicable, and thus, truncated-FBP and scout- reconstruction methods were applied. Figures 3.9A and 3.9D show the reconstruction results by these two methods. Arrows in subfigures A and G mark the corresponding features that are only faintly discernible in the up-sampled global reconstruction (subfigure G). Figure 3.9H contains line profiles across line marked in subfigures A and D. The line plots do not show any significant difference in DC values between the two interior reconstruction methods. Also, no cupping artifact was observed by either of the reconstruction methods.

For better characterization of the results, further tests were carried out. The original interior sinogram (containing 988 detector pixels) was further truncated down to 814 and 648 detector pixels (i.e. reduced by 18% and 36% from original length, respectively). Truncated-FBP and scout-reconstruction methods were employed – the reconstructed slices are shown in subfigures B, C, E and F. Cupping artifact begins to appear in the truncated-FBP reconstruction when the detector length decreases to 648 pixels (see subfigure C, and the right edge of the corresponding line-plot in H). However, scout-reconstruction results do not show cupping artifact at any detector length, and hence this method is more robust than truncated-FBP. Overall, the artifacts due to truncated-FBP are much lower for this sample

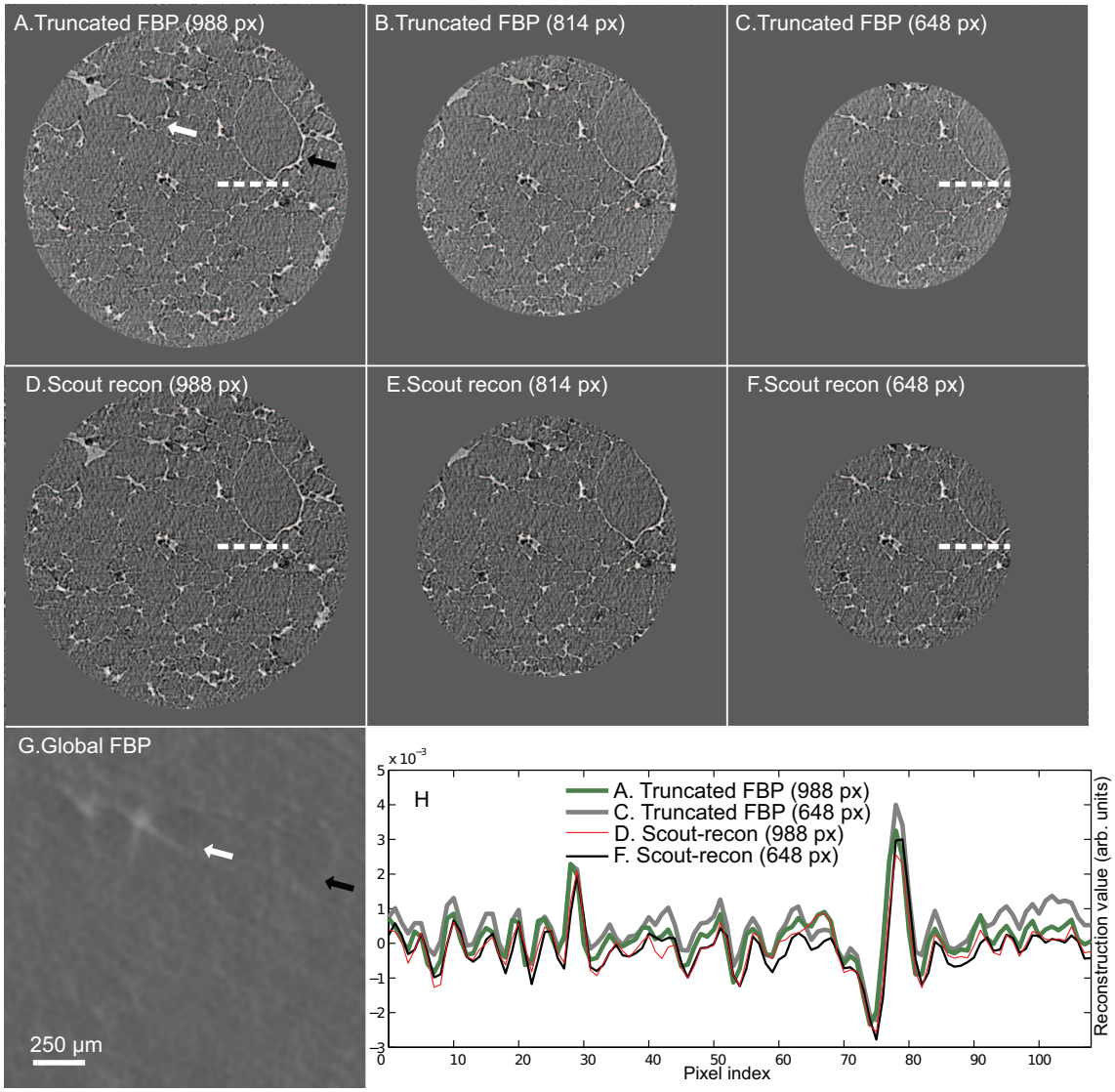

Figure 3.9: Tomographic reconstruction of mouse lung sample. Reconstruction of interior ROI by (A) truncated-FBP, (D) scout-reconstruction, and (G) global FBP (after up-sampling to pixel size of high-resolution scan). In subfigures A and G, arrows mark corresponding features. Interior sinogram, originally 988 detector pixels long, was further truncated down to 814 and 648 pixels. Truncated-FBP and scout-reconstruction methods were applied at the different detector lengths, and the corresponding reconstructed slices are shown in subfigures B, C, E, and F. (H) Plot of line profiles across white dotted lines in subfigures A, C, D, F.

than for other samples in this study – this may be explained by the fact that the sample has no highly absorbing structures outside the FOV for the interior scan.

3.5 Conclusion and discussion

In this study, we introduced two methods that use only a small number of scout views to achieve accurate interior reconstruction. The scout-interpolation method (Sec. 3.3.4) is an extension of multi-resolution acquisition techniques [24, 28, 35]. While it is only applicable to special scan configurations, it provides an extremely simple technique to achieve accurate interior reconstruction. The scout-reconstruction method (Sec. 3.3.4) combines compressed sensing based reconstruction [42] with multi-resolution acquisition. This technique is more dynamic as it can be applied to multiple scan configurations. Scout-interpolation and reconstruction techniques were first verified on physical micro-CT phantoms that were specially fabricated for this study. The methods were then tested on two datasets from separate studies that could benefit from this new technique. In all cases except the lung sample, there was a major reduction of cupping artifacts and DC bias as compared to truncated-FBP. For the lung sample, scout-reconstruction and truncated-FBP provided similar reconstruction values for the original interior data. However, when the data was truncated even further, scout-reconstruction was shown to be more robust.

We demonstrated that five to seven scout views enabled accurate interior reconstruction in all the samples tested in this study. The phantoms and samples were designed or selected so that they posed a variety of challenges e.g. symmetric vs. asymmetric location of ROI, moderately attenuating vs. highly attenuating material etc. However certain samples may pose extremely limiting geometry or attenuation conditions, and require a higher number of scout views. While this remains a matter of further investigation, the number of scout views is still expected to be lesser than 20 (the number of views that has been shown to achieve sufficiently high image quality in various studies on sparse image reconstruction [3, 31, 45]).

The start- and end-angles (i.e. the angular range) of the scout views should be selected such that they provide the most relevant information for the two proposed methods. In Sec. 3.4.1, some guidelines for selecting these values for the scout-interpolation technique were noted. For the scout-reconstruction technique, acquiring scout views over the short-scan range of (180° + fan-angle) [26] is the optimum choice as this provides the most complimentary information in the SS-SART-TV step of Sec. 3.3.4 [31]. In the current study, these guidelines were obeyed, and high reconstruction accuracy was achieved. Only in case of the rock sample, scout views were acquired over the entire 360°, but the circular nature of the sample allowed high reconstruction accuracy without optimum sampling.

The run-times for the reconstruction algorithms described in Sec. 3.3.4 (truncated-FBP, scout-interpolation, scout-reconstruction and SS-SART-TV) were measured for the rock sample. The timing results, which are tabulated in Tab. 3.2, show that scout-interpolation and

Table 3.2: Algorithm run-times. The first row lists the absolute run-times and the second row lists the run-times after normalization w.r.t run-time of truncated-FBP.

Algorithm	Trunc. FBP	Scout-interp.	Scout-recon	SS-SART-TV
Run time (sec.)	116.44	123.45	142.89	5527.32
Run time (normalized)	1.00	1.06	1.23	47.47

scout-reconstruction represent only a 6% and 23% overhead w.r.t. truncated-FBP, while SS-SART-TV is almost 47 times more time consuming than truncated-FBP. SS-SART-TV is the most time-consuming because it is a purely iterative reconstruction method, and works on all the interior projections acquired at a dense angular sampling. Within the scout-reconstruction method, there is a sub-step involving iterative reconstruction (Step (3) in Sec. 3.3.4). But this sub-step uses only a handful of scout views, and is thus extremely quick. Also, in step (4) of the scout-reconstruction method, the forward projection was performed on a sparse grid. This helped to sidestep the issue (pointed out in [18]) of computational overload for a prohibitively large forward projection. Our implementation was not fully optimized, and future optimizations (e.g. through GPU implementation, TV minimization by soft-thresholding [45]), would further reduce all run-times.

Overall, the two new methods introduced in this study allow accurate interior reconstruction. Due to their low computational cost, these methods can be easily incorporated into commercial micro-CT scanners. These methods may extended to industrial CT, or any imaging modality in which the scanner allows the acquisition of both global overview projections as well as high-resolution interior projections. Future research directions may include efforts to extend the scout-interpolation technique to arbitrary scan geometries e.g. by using "data-weighting" schemes similar to the one described in [18].

3.6 Acknowledgments

The authors thank Michael Feser and Tom Case for their advice about raw-data corrections before reconstruction, reconstruction performance metrics, manuscript write-up, etc. The authors also thank Abhilash Kizhakke Puliyakote for his assistance with data acquisition and analysis. The CT studies were performed in the SBES Advanced Multiscale Computed Tomography Facility (SAMCT), supported by an NIH SIG grant (RR025667), an NSF MRI grant (CMMI0923297), an NIH R01 grant (R01-080285), as well as internal funding from ICTAS and SBES at Virginia Tech.

Bibliography

[1] Bassam Alfeeli, Daniel Cho, Mehdi Ashraf-Khorassani, Larry T. Taylor, and Masoud Agah. MEMS-based multi-inlet/outlet preconcentrator coated by inkjet printing of polymer adsorbents. *Sensors and Actuators B: Chemical*, 133(1):24–32, July 2008.

[2] Deepak K Bharkhada. *Development of Novel Cardiac CT Methods*. PhD thesis, Wake Forest University, 2010.

[3] E.J. Candès, Justin Romberg, and Terence Tao. Robust Uncertainty Principles : Exact Signal Reconstruction from Highly Incomplete Frequency Information. *Information Theory, IEEE Transactions on*, 52(2):489–509, 2006.

[4] R Chityala, K R Hoffmann, S Rudin, and D R Bednarek. Artifact reduction in truncated CT using Sinogram completion. *Proceedings - Society of Photo-Optical Instrumentation Engineers*, 5747(3):2110–2117, February 2005.

[5] Marius Costin, Delphine Lazaro-Ponthus, Samuel Legoupil, Philippe Duvauchelle, and Valérie Kaftandjian. A 2D multiresolution image reconstruction method in X-ray computed tomography. *Journal of X-ray science and technology*, 19(2):229–47, January 2011.

[6] Bruno De Man, Samit Basu, JB Thibault, J. Hsieh, JA Fessier, C. Bouman, and K. Sauer. A study of four minimization approaches for iterative reconstruction in X-ray CT. In *Nuclear Science Symposium Conference Record*, volume 5, pages 2708–2710, 2005.

[7] Michel Defrise, Frédéric Noo, Rolf Clackdoyle, and Hiroyuki Kudo. Truncated Hilbert transform and image reconstruction from limited tomographic data. *Inverse Problems*, 22(3):1037–1053, June 2006.

[8] Adel Faridani, EL Ritman, and KT Smith. Local Tomography. *SIAM Journal on Applied Mathematics*, 52(2):459–484, 1992.

[9] M Feser, J Gelb, H Chang, H Cui, F Duewer, S H Lau, A Tkachuk, and W Yun. Sub-micron resolution CT for failure analysis and process development. *Measurement Science and Technology*, 19(9):094001, September 2008.

[10] B. Goris, W. Van den Broek, K.J. Batenburg, H. Heidari Mezerji, and S. Bals. Electron tomography based on a total variation minimization reconstruction technique. *Ultramicroscopy*, 113:120–130, November 2011.

[11] G.T. Herman and R.M. Lewitt. Evaluation of a preprocessing algorithm for truncated CT projections. *Journal of Computer Assisted Tomography*, 5(1):127–135, 1981.

[12] Stefan Hoppe, Joachim Hornegger, Gunter Lauritsch, Frank Dennerlein, and Frederic Noo. Truncation correction for oblique filtering lines. *Medical Physics*, 35(12):5910, 2008.

[13] Willi A. Kalender. *Computed tomography: fundamentals, system technology, image quality, applications*. Wiley-VCH, 2011.

[14] Daniel Kolditz, Michael Meyer, Yiannis Kyriakou, and Willi a Kalender. Comparison of extended field-of-view reconstructions in C-arm flat-detector CT using patient size, shape or attenuation information. *Physics in medicine and biology*, 56(1):39–56, January 2011.

[15] H Kong and J Pan. Sequence Subsets SART for Cone-Beam CT. *Journal of Computational Information Systems*, 12:4514–4521, 2011.

[16] A Kyrieleis, V Titarenko, M Ibison, T Connolley, and P J Withers. Region-of-interest tomography using filtered backprojection: assessing the practical limits. *Journal of microscopy*, 241(1):69–82, January 2010.

[17] RM Lewitt and RHT Bates. Image reconstruction from projections: III: Projection completion methods (theory). *Optik*, 50(3):189—-204, 1978.

[18] Clemens Maaß, Michael Knaup, and Marc Kachelrieß. New approaches to region of interest computed tomography. *Medical Physics*, 38(6):2868, 2011.

[19] Ryuta Mizutani, Akihisa Takeuchi, R Yoshiyuki Osamura, Susumu Takekoshi, Kentaro Uesugi, and Yoshio Suzuki. Submicrometer tomographic resolution examined using a micro-fabricated test object. *Micron*, 41(1):90–5, January 2010.

[20] O. Nalcioglu, ZH Cho, and RY Lou. Limited Field of View Reconstruction in Computerized Tomography. *Nuclear Science, IEEE Transactions on*, 26(1):546–551, 1979.

[21] Frank Natterer. *The mathematics of computerized tomography*. SIAM, 2001.

[22] Frédéric Noo, Rolf Clackdoyle, and Jed D Pack. A two-step Hilbert transform method for 2D image reconstruction. *Physics in Medicine and Biology*, 49(17):3903–3923, September 2004.

[23] K Ogawa and H Urabe. Image quality in the modified ordered subset-Bayesian reconstruction. In *Nuclear Science Symposium, 1999. Conference Record. 1999 IEEE*, volume 2, pages 874–878, 1999.

[24] D. Pak-Kong Lun and T.C. Hsung. Region-of-interest tomography using multiresolution interpolation. In *Acoustics, Speech, and Signal Processing, 1997. ICASSP-97., 1997 IEEE International Conference on*, pages 2825–2828, 1997.

[25] Xiaochuan Pan, Emil Y Sidky, and Michael Vannier. Why do commercial CT scanners still employ traditional, filtered back-projection for image reconstruction? *Inverse problems*, 25(12):1230009, January 2009.

[26] D.L. Parker. Optimal short scan convolution reconstruction for fanbeam CT. *Medical Physics*, 9:254, 1982.

[27] Erik L Ritman. Micro-computed tomography-current status and developments. *Annual review of biomedical engineering*, 6:185–208, January 2004.

[28] B Sahiner and a E Yagle. Region-of-interest tomography using exponential radial sampling. *IEEE transactions on image processing : a publication of the IEEE Signal Processing Society*, 4(8):1120–7, January 1995.

[29] K. Sen Sharma, S. Seshadri, M. Feser, and G. Wang. Accurate Resolution Measurement for X-Ray Micro-CT Systems. In *AIP Conference Proceedings*, volume 1365, pages 337–340, 2011.

[30] Kriti Sen Sharma, Xin Jin, Christian Holzner, Shree Narayanan, Baodong Liu, Dong Wang, Masoud Agah, Linbing Wang, Hengyong Yu, and Ge Wang. Experimental studies on few-view reconstruction for high-resolution micro-CT. *Journal of X-ray science and technology*, 21(1):25–42, January 2013.

[31] Emil Y Sidky, Chien-min Kao, and Xiaochuan Pan. Accurate image reconstruction from few-views and limited-angle data in divergent-beam CT. *Journal of X-Ray Science and Technology*, 14:119–139, 2006.

[32] Stuart R. Stock. *MicroComputed Tomography: Methodology and Applications*. CRC Press, 2008.

[33] Katsuyuki Taguchi, Jingyan Xu, Somesh Srivastava, Benjamin M. W. Tsui, Jochen Cammin, and Qiulin Tang. Interior region-of-interest reconstruction using a small, nearly piecewise constant subregion. *Medical Physics*, 38(3):1307, 2011.

[34] Jie Tang, Brian E Nett, and Guang-Hong Chen. Performance comparison between total variation (TV)-based compressed sensing and statistical iterative reconstruction algorithms. *Physics in medicine and biology*, 54(19):5781–804, October 2009.

[35] G. Tisson, P. Scheunders, and D. Van Dyck. 3D region of interest x-ray CT for geometric magnification from multiresolution acquisitions. In *2004 2nd IEEE International Symposium on Biomedical Imaging: Macro to Nano (IEEE Cat No. 04EX821)*, volume 2, pages 567–570. Ieee, 2004.

[36] Hiroshi Urabe and K Ogawa. Improvement of Reconstructed Images in Ordered Subset - Bayesian Reconstruction Method. In *Nuclear Science Symposium, 1998. Conference Record. 1998 IEEE*, pages 1342–1346, 1998.

[37] Gert Van Gompel. *Towards accurate image reconstruction from truncated x-ray CT projections*. PhD thesis, University of Antwerp, 2009.

[38] Dragos M Vasilescu, Zhiyun Gao, Punam K Saha, Leilei Yin, Ge Wang, Beatrice Haefeli-Bleuer, Matthias Ochs, Ewald R Weibel, and Eric a Hoffman. Assessment of morphometry of pulmonary acini in mouse lungs by nondestructive imaging using multiscale microcomputed tomography. *Proceedings of the National Academy of Sciences of the United States of America*, 109(42):17105–10, October 2012.

[39] Dragos Mihai Vasilescu, Christine Klinge, Lars Knudsen, Leilei Yin, Ge Wang, Ewald R Weibel, Matthias Ochs, and Eric a Hoffman. Stereological Assessment of Mouse Lung Parenchyma via Non-destructive Multi-scale Micro CT Imaging validated by Light Microscopic Histology. *Journal of applied physiology (Bethesda, Md. : 1985)*, December 2012.

[40] G. Wang, Y. Bresler, and V. Ntziachristos. Guest Editorial Compressive Sensing for Biomedical Imaging. *Medical Imaging, IEEE Transactions on*, 30(5):1013–1016, 2011.

[41] Ge Wang, Tein-Hsiang Lin, Ping-chin Cheng, and Douglas M. Shinozaki. A General Cone-Beam Reconstruction Algorithm. *Ieee Transactions on Medical Imaging*, 12(3):486–496, 1993.

[42] H Yu and G Wang. Compressed sensing based interior tomography. *Physics in medicine and biology*, 54(9):p2791–2805, 2009.

[43] Hengyong Yu, Guohua Cao, Laurel Burk, Yueh Lee, and Jianping Lu. Compressive sampling based interior reconstruction for dynamic carbon nanotube micro-CT. *Journal of X-ray science and technology*, 17(4):295–303, 2009.

[44] Hengyong Yu and Ge Wang. A General Formula for Fan-Beam Lambda Tomography. *International Journal of Biomedical Imaging*, 2006:1–9, 2006.

[45] Hengyong Yu and Ge Wang. A soft-threshold filtering approach for reconstruction from a limited number of projections. *Physics in medicine and biology*, 55(13):3905–16, July 2010.

[46] Hengyong Yu, Ge Wang, Jiang Hsieh, Daniel W Entrikin, Sandra Ellis, Baodong Liu, and John Jeffrey Carr. Compressive sensing-based interior tomography: preliminary clinical application. *Journal of computer assisted tomography*, 35(6):762–4, 2011.

Chapter 4

Interior micro-CT with an offset detector array

Publication information

The manuscript: *Kriti Sen Sharma*, Omid Ghasemalizadeh, Hengyong Yu, Ge Wang, Guohua Cao, "Interior micro-CT with an offset detector array" is under preparation.

Author contributions

The contributions of the various authors are listed below:

- *Kriti Sen Sharma*[1]: Design and implementation of all reconstruction algorithms, experimental design, numerical simulation, manuscript writing
- *Omid Ghasemalizadeh*[2]: Phantom fabrication, design and implementation of micro-CT scanner that allowed offset detector acquisition, scans of phantom
- *Hengyong Yu*[3] and *Ge Wang*[4]: Manuscript writing, code debugging, design of reconstruction algorithms
- *Guohua Cao*[5]: Experimental design, manuscript writing, design and implementation of micro-CT scanner that allowed offset detector acquisition

Author affiliations

1. Dept. of Elec. & Comp. Eng., Virginia Tech, Blacksburg, VA 24061, USA
2. Dept. of Mechanical Eng., Virginia Tech, Blacksburg, VA 24061, USA

3. Biomedical Imaging Division, VT-WFU School of Biomedical Eng. & Sciences, Wake Forest Univ. Health Sciences, Winston-Salem, NC 27157, USA

4. Biomedical Imaging Center, Rensselaer Polytechnic Institute, Troy, NY 12180, USA

5. Biomedical Imaging Division, VT-WFU School of Biomedical Eng. & Sciences, Virginia Tech, Blacksburg, VA 24061, USA

4.1 Abstract

Offset detector acquisition has been used in the past to increase the size of the scan field of view. Yet, previous studies assumed that the entire sample was covered after offset detector acquisition. In this study, we focus on the case where the imaged area after offset detector acquisition still covers an interior region-of-interest of the sample. The increased scan coverage is beneficial to multiple applications; yet special care must be taken to handle the dual projection truncation due to interior and offset detector acquisition. We developed three reconstruction methods by combining projection completion with analytic and compressed sensing (CS) based iterative methods for offset detector reconstruction. Next, we tested the methods through extensive numerical simulation and tests on real data. The CS based reconstruction yields the highest image quality in the numerical simulation. Yet, some limitations of the CS based techniques are observed in case of real data with various imperfect properties. Important guidelines are suggested for future improvements.

4.2 Introduction

Micro computed tomography (micro-CT) [23, 29] has emerged as a powerful non-invasive tool for a variety of applications including preclinical cancer research [16, 22], failure analysis in industrial applications [5], studies on bone structure [37], evolutionary studies [26] etc. Compared to clinical CT scanners (resolution: 1 mm), micro-CT scanners usually achieve much higher spatial resolution (1 – 100 μm). When optimizing micro-CT scanner geometry, there is usually a trade-off between the spatial resolution and the field-of-view (FOV) size. A geometry with high magnification leads to a higher spatial resolution but smaller FOV. When a certain spatial resolution is required but the object is larger than the FOV, projection truncation unavoidably occurs. The reconstruction by using truncated projections may suffer from cupping artifact at the edges, and a difference in CT numbers (a DC bias) [3, 38]. These artifacts may be negligible or unimportant in certain applications [13]. Alternatively the artifacts may be reduced by a multitude of interior reconstruction algorithms [12, 17, 19, 20, 36, 38] – the most common of which are the projection completion techniques [32, 33]. Yet, despite the possibility of reconstruction artifacts, the practise of acquiring truncated projections of an interior ROI is very common in the field.

The scan FOV may be increased up to twice its original size, by displacing the detector in a direction tangential to the acquisition trajectory [2, 34]. The 'offset detector' or 'displaced detector' acquisition leads to asymmetric coverage of the imaged object at each projection angle, and consequently, the reconstruction process must account for this. Over the years, many such reconstruction techniques have been developed, and they can be categorized into three groups:

1. The first group of algorithms employ a weighting scheme along with fan-beam (or cone-beam) filtered back projection (FBP) reconstruction [2, 6, 15, 34, 39]. The weighting scheme accounts for the fact that a central overlap region is sampled over the entire 360°, while the remaining is sampled over 180° only. The weighting is carried out either before the ramp filtering step of FBP (pre-convolution weighting), or after (post-convolution weighting).
2. A second class of algorithms employs the local derivative filter instead of the non-local ramp filter in the first step, and a back-projection filtration (BPF) or derivative back-projection (DBP) in the subsequent steps [14, 25]. These methods also involve a inverse Hilbert filtering step [11]. The DBP / BPF based methods provided theoretically exact reconstruction schemes for offset detector CT [14], as FBP based methods typically involved certain approximations [2].
3. More recently, iterative reconstruction techniques have been developed that employ a weighted projection update scheme [1, 7]. The iterative techniques have been shown to reduce left-right shading artifacts [7], and also allowed high quality reconstruction when using a much lower number of projections [1].

All previous studies on offset detector CT assumed that the scan FOV after offset detector acquisition covered the entire sample. In this study, we investigate the case when the scan FOV after displacing the detector still covers an interior ROI of the sample. This is quite common in micro-CT where the imaged object may be more than twice the size of the detector array (offset detector acquisition can increase the FOV up to $2x$). Also it is usually beneficial if a larger ROI within the object of interest can be imaged, while maintaining the same spatial resolution. Clearly there is sufficient motivation for interior micro-CT with an offset detector array.

For truncated scans acquired with an offset detector, there are two types of truncation – the first due to offset detector acquisition, and the second w.r.t. the global sample. The reconstruction algorithms need to be modified accordingly. We note that the DBP / BPF based exact reconstruction methods are not directly applicable for such scans. The inverse Hilbert filtering step requires that measured information be available over an interval larger than the object support [25], but this is not the case in such scans. As such, we focus our attention on the FBP-based and iterative reconstruction schemes.

Our contributions in this study are as follows:

i. First, we detail the procedure for extending previous methods so as to allow interior reconstruction with an offset detector array. We describe a total of three reconstruction algorithms.
ii. Next, we run exhaustive numerical simulations to compare the three reconstruction methods. Through the simulations, we make the interesting observation that apart from extending the ROI, interior reconstruction with offset detector acquisition may actually lead to reduced DC bias artifact.
iii. We also observe that in the numerical simulations, iterative reconstruction scheme for offset detector array performs better than analytical methods.
iv. Finally, we test the reconstruction algorithms on real data collected on an in-house micro-CT system. We find that iterative reconstruction techniques have some limitations in case of real data, and we provide some important guidelines about this.

The rest of this paper is organized as follows. First, the scan geometry, numerical simulations, real data acquisition, and the three reconstruction algorithms are described in Sec. 4.3. The results of the numerical simulations and reconstruction on real data are described in Sec. 4.4. Finally, Sec. 4.5 concludes the paper with a discussion and future research directions.

4.3 Methods

4.3.1 Interior tomography with an offset detector array

The fan-beam geometry considered in this study is shown in Fig. 4.1A. The iso-center of the scan is marked by a white cross-hair in the figure. The detector array is marked by a thick black line. By introducing a detector offset, and acquiring projections across 360°, the effective-ROI increases as shown in the figure. However, even after offset-detector acquisition, the detector is too small to cover the global sample. Thus the acquired projections must be considered for both the detector offset, and the projection truncation w.r.t. the global sample.

4.3.2 Numerical simulations

A special modification of the Shepp-Logan phantom was created for the purpose of this work. Specifically, the Shepp-Logan phantom was expressed into two matrices – a 512×512 matrix with side length 5.92 mm, and another 256×256 matrix with side length 2.96 mm. In these two matrices, the length of the major axis of the largest ellipse were respectively 5.44 mm and 2.74 mm. The larger matrix was transposed, and the smaller phantom was then added on top of the larger matrix at a slightly skewed position from the center. This combination is termed as the 'double Shepp-Logan phantom' and is shown in Fig. 4.1A.

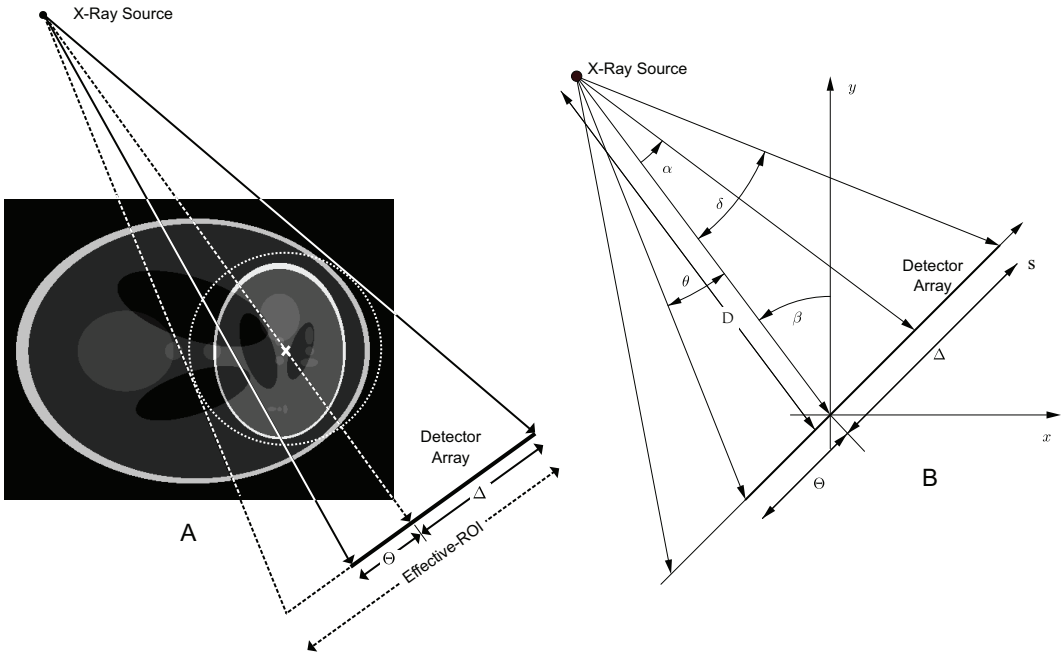

Figure 4.1: Interior tomography with offset detector array. (A) Fan-beam geometry for interior tomography with offset detector array. (B) Mathematical notations for the offset detector geometry, where the detector array is scaled to go through isocenter of the scan.

Only the inner Shepp-Logan phantom was targeted for the interior scans. This provided a sufficiently detailed ROI for testing purposes. The skewed position of the inner phantom guaranteed that the truncation was not uniform at different projection angles.

The source-to-iso-center distance was fixed at 106.28 mm, and the source-to-detector distance was fixed at 459.45 mm. These parameters were selected so as to match with the settings of the actual physical experiments that are described subsequently in Sec. 4.3.3. A CT detector with 154 elements and a detector pixel size of 50 μm (i.e. a length of 7.7 mm) was used to acquire x-ray projections of the double Shepp-Logan phantom. At the specified geometry, the ROI that can be imaged by this detector has a diameter of 1.78 mm, that is smaller than the inner Shepp-Logan phantom. To increase the extent of the ROI, the detector was offset by amounts equal to 9.4%, 18.8%, 28.2%, 37.6% and 46.9% of the detector length (again to match the conditions in the physical experiments). For each detector offset case, 720 projections were acquired to cover the entire angular range of 360°, with an angular separation of 0.5°. X-ray projections were calculated by using a distance driven ray-sum model [4].

Complete projections (i.e. without detector offset) were also acquired over the effective-ROI (see Fig. 4.1A) corresponding to each offset percentage. The acquisition over the effective-ROI was used to determine reconstruction accuracy as described in Sec. 4.3.4.

X-ray photon noise statistics are known to be well approximated by the Poisson noise model [9, 11]. In order to simulate realistic acquisition conditions, Poisson noise was added to the projection data. The noise level was fixed at a moderately high projection signal-to-noise ratio value of ∼75 [28]. For each data point, the experiment was repeated five times to measure the variability of the reconstruction w.r.t. the noise.

4.3.3 Experimental setup

Micro-CT scanner

Physical experiments were carried out on a micro-CT scanner that was developed in-house. The system consists of an Ultrabright™ microfocus x-ray source (Oxford Instruments, Oxfordshire, UK), a B5990TS™ motorized rotation stage (Velmex Inc., Bloomfield, NY), a manual lab-jack to adjust height of the rotation stage, a C7942CA-27™ flat panel detector (Hamamatsu Corp., Bridgewater, NJ), and two motorized translational stages (Velmex Inc.) to hold and position the detector. Also, an interface has been developed by LabVIEW™ (National Instruments Corp., Austin, TX) to control the rotation table and detector readout time for data collecting. Figure 4.2 shows all components of the micro-CT system.

The x-ray tube and detector are stationary, and the sample rotates during data collection. The bench-top micro-CT system gives the ability of having a range of magnification factors from ∼1.1 to 5.0. This provides a wide range of spatial resolution for different applications.

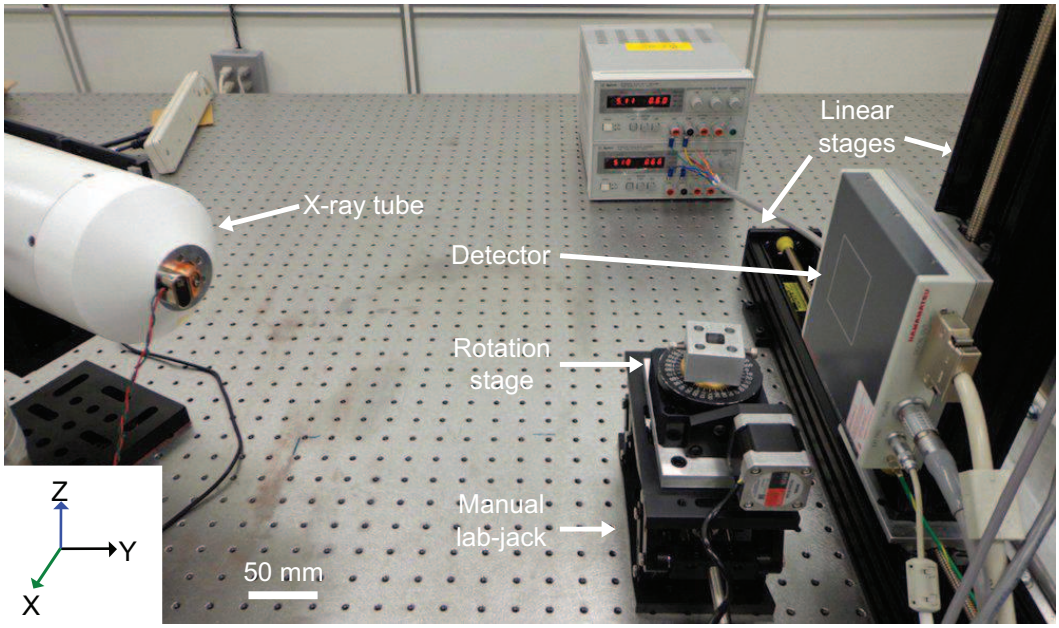

Figure 4.2: Micro-CT system components. Inset on left marks the x-y-z axes, where the x-y plane is the central plane of the cone-beam, and z is the vertical direction.

Detector offset is introduced by a horizontal translational stage, which is also controlled by the LabVIEW^{TM} VI.

Phantom fabrication

A micro-CT phantom developed previously by our group [27] was repurposed for this study. Figure 4.3A (i.) shows the previous micro-CT phantom that had a diameter of ∼8 mm. Using Scotch tape (3M Inc., Maplewood, MI), various plastic items (plastic screws, plastic tubes et.) were fixed rigidly around two acrylic tubes of inner diameter 9.5 mm and 22.5 mm mm. The tubes with items wrapped around them are shown in Figs. 4.3A (ii.) and (iii.). These tubes were assembled in a concentric manner as shown in Fig. 4.3B to form the micro-CT phantom used in this study.

Scanning protocol

The flat-panel CT detector in our in-house micro-CT scanner has an active detection region of 50.6 mm × 50.6 mm. The active region is divided into a grid of 1012 × 1012 with the isotropic detector pixel width being 50 μm. The scan geometry (i.e. source-to-detector distance etc.) and acquisition settings (number of projections etc.) were fixed according to

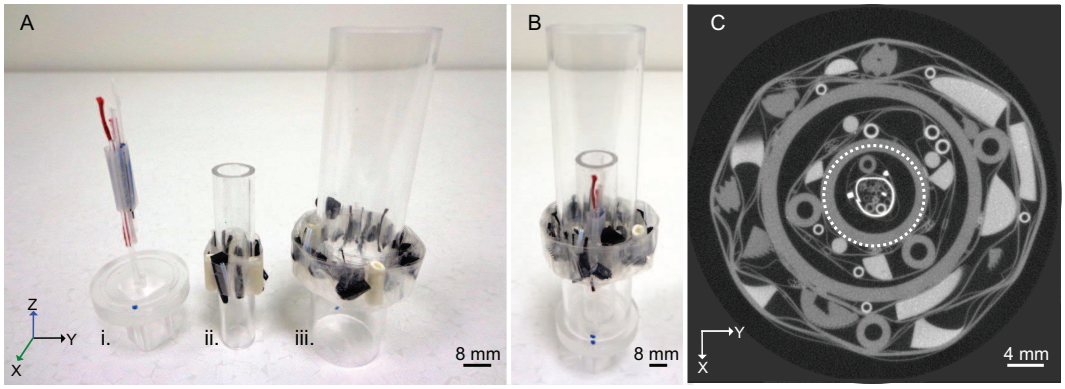

Figure 4.3: Micro-CT phantom fabrication. (A) The three components of the phantom including (i.) the 8 mm phantom and (ii.), (iii.) the two acrylic tubes wrapped with small plastic items. (B) The micro-CT phantom used in this study was assembled by placing (ii.) and (iii.) around (i.). (C) Reconstructed cross section across the central slice of the cone-beam; ROI of interior scan with centrally located detector (i.e. without offset-detector) is marked by dotted circle. x-y-z axes are marked according to convention in Fig. 4.2.

the parameters listed in the 'Interior scan' column of Tab. 4.1. At this geometry, an ROI of diameter 11.68 mm can be imaged, which is larger than diameter of the 8 mm phantom. Next, the detector panel was displaced horizontally (i.e. in the x direction) at the following detector offset percentages: 9.4%, 18.8%, 28.2%, 37.6% and 46.9%. Interior scans were acquired at each detector offset.

Finally, while keeping the sample position fixed, the relative positions of the source and detector were modified so that the entire micro-CT phantom ($\varnothing$. 39 mm) could be fit within the FOV. A global scan was acquired according to the parameters listed in Tab. 4.1 (column: 'Global scan'). The global scan provided a visual reference for our interior scans – the central slice of the global scan was reconstructed by fan-beam FBP algorithm and is shown in Fig. 4.3C. The global scan also allowed the determination of the object boundary, which was subsequently utilized to aid projection completion in the interior reconstruction algorithms (Secs. 4.3.4 and 4.3.4).

4.3.4 Reconstruction algorithms

In Fig. 4.1B, the mathematical notations are introduced. For ease of mathematical formulation, the detector array is scaled to pass through the iso-center of the scan (also the origin of the reconstruction system). D is the distance from x-ray source to the origin. β is the angular position of the x-ray source for the selected projection in the tomography. Θ and Δ are the lengths of the longer and shorter segments of the detector array w.r.t. the iso-center

Table 4.1: Scan settings for offset detector study. Scans were acquired on the Explorer system for the micro-CT phantom (RA = rotation axis).

Scan Parameter	**Interior scan**	**Global scan**
Source setting	80 kV, 250 μA	80 kV, 250 μA
Source-RA distance	106.28 mm	387.80 mm
Source-Detector distance	459.45 mm	451.81 mm
Number of detector pixels	1012	1012
Exposure time	1 sec	1 sec
Start-angle	0°	0°
End-angle	359.5°	359.5°
Number of projections	720	720
Image pixel size (effective)	11.55 μm	42.90 μm

(θ and δ are the corresponding angular values). Thus, $(\Theta + \Delta)$ is the total length of the detector array. s and α are respectively the spatial and angular values denoting a specific detector cell. The percentage p of offset of the detector array can be calculated as:

$$p = \frac{\frac{\Theta+\Delta}{2} - \Theta}{\Theta + \Delta} \times 100\% \tag{4.1}$$

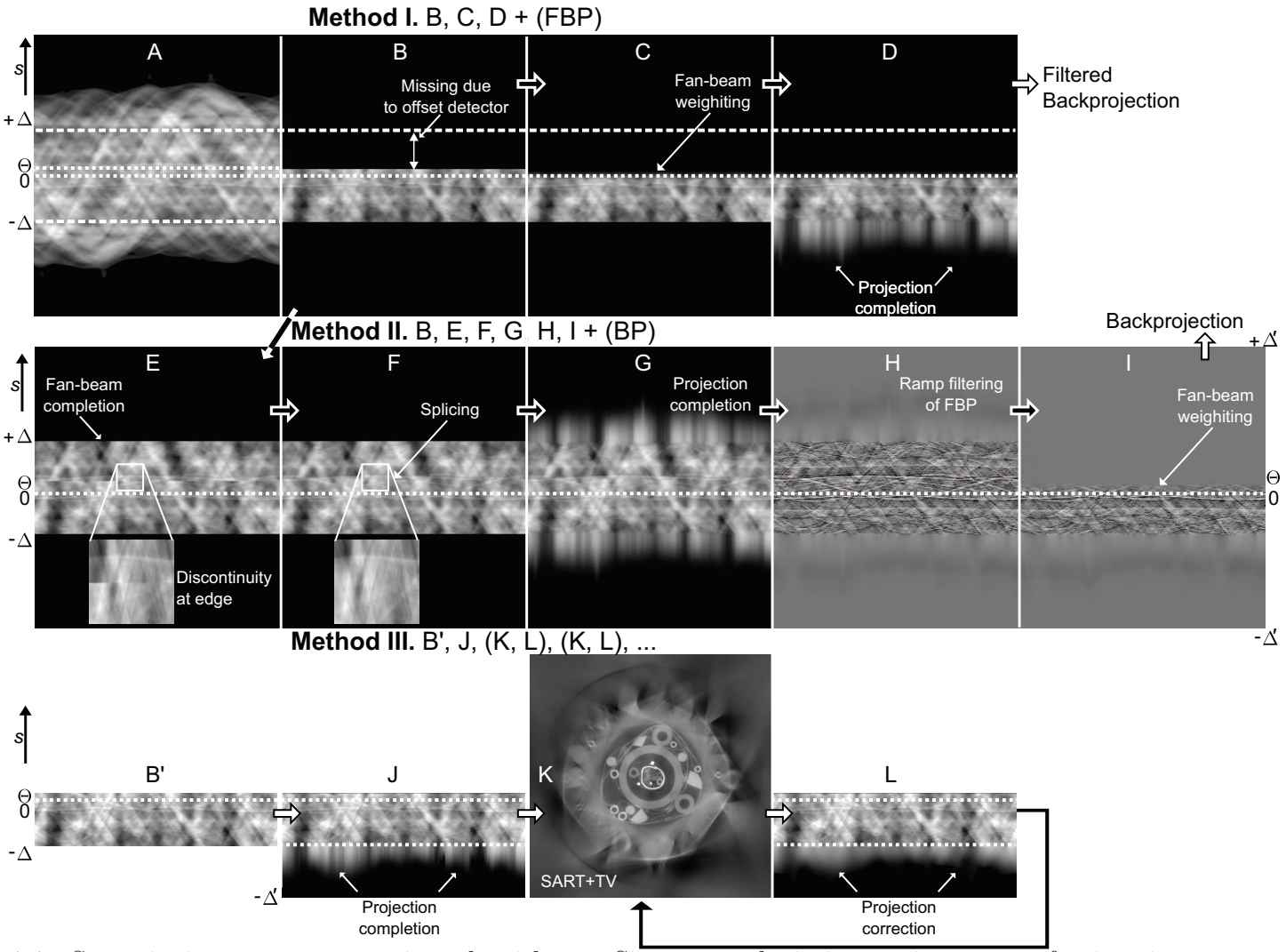

Figure 4.4: Steps in image reconstruction algorithms. Sinograms depicting various steps for interior reconstruction with an offset detector array. All sinograms have 360°angular coverage. (A) Global sinogram shown as reference. (B) Truncated sinogram with offset detector acquisition. (C) Sinogram after offset-detector weighting. (D) Projection completion by cos^2 extrapolation up to object boundary. (E) Fan-beam completion. (F) Splicing to remove discontinuity at edge. (G) Projection completion. (H) Ramp filtering. (I) Offset-detector weighting. (B′) Same as subfigure B, but without zeros at missing data-points. (J) Projection completion at external edge. (K) Result of one iteration of SART + TV algorithm. (L) Projection correction.

Method I: Pre-convolution weighting

The first reconstruction method is an extension of the pre-convolution weighting scheme described in [2], or equivalently the fan-beam weighting scheme of [34]. The steps of the algorithm are listed below, and each step-number denotes the index of corresponding subfigure in Fig. 4.4. The global sinogram for the micro-CT phantom is shown as a reference in Fig. 4.4A.

B. The interior sinogram with detector offset percentage at 37.6% is shown in Fig. 4.4B. The missing data between $\Theta \leq s \leq \Delta$ due to offset detector acquisition is marked in the subfigure.

C. The weighting function described in [34] is used to filter the fan-beam projections of Fig. 4.4B:

$$w(s,\beta) = w(s) = \begin{cases} 1, & -\Delta \leq s \leq -\Theta \\ \frac{1}{2}\left(-sin\left(\frac{\pi \arctan\frac{s}{D}}{2\arctan\frac{\Theta}{D}}\right)+1\right), & -\Theta \leq s \leq \Theta \\ 0, & \Theta \leq s \leq \Delta \end{cases} \tag{4.2}$$

D. Projection completion was carried out by extrapolating the truncated sinogram up to the object boundary by cosine-extrapolation [32].

- Finally, traditional fan-beam FBP reconstruction was employed on the completed sinogram to reconstruct the ROI.

Eq. 4.2 obeys the two requirements imposed by Parker [21] i.e. it (1) creates a smooth edge at the truncation edge, and (2) also weights the projections so that doubly sampled or redundant data have a unit total weight [34].

The sinogram after Step. C was still truncated at the outer edge, and thus projection completion was required before reconstruction by FBP. In our study, we assumed that the additional information about object boundary (i.e. object support) was known. This information is usually acquired from external physial measurements, a low-resolution global scan [3], or optical measurements by a time-of-flight camera [10]. Approximately accurate knowledge of the object support has been shown to significantly reduce the truncation errors [36, 10]. We selected the method of cosine-extrapolation up to object boundary because of its' ease of use and computational simplicity. Please note that other methods [3, 19, 27, 38] can be used to achieve even higher accuracy in the sinogram completion step.

Method II: Post-convolution weighting

The second reconstruction method is an extension of the post-convolution weighting scheme of [2]. The steps are listed below, and each step-number denotes the index of corresponding

subfigure in Fig. 4.4.

E. $R_\beta(s)$ denotes a fan-beam projection acquired at angle β, and s is the spatial position of a detector element. The missing data in the range $\Theta \leq s \leq \Delta$ is recovered by the technique of sinogram reflection [18] i.e. by using:

$$R_{\beta+\pi+2\alpha}(-s) = R_\beta(s) \tag{4.3}$$

where α is the angular position of a detector element as shown in Fig. 4.1B.

F. Due to non-linearities in the projection process (e.g. beam-hardening etc.), the recovered data may not be equal to the ground truth. This creates discontinuities at the edge where the real data meets the recovered data (like in Fig. 4.4E inset). The splicing technique of [2] was applied. The improvement by splicing is clearly evident in Fig. 4.4F inset.

G. Projection completion was carried out in the same way as in Sec. 4.3.4.

H. Next, the projections were filtered by a the smoothed Ram-Lak filter [11]. In our implementation, we used a Hanning window to do the smoothing.

I. The weighting function of Eq. 4.2 was applied to the filtered projections over the extended range $-\Delta' \leq s \leq \Delta'$. Here the overlap range $-\Theta \leq s \leq \Theta$ still remains the same.

- Finally, the filtered and weighted projections were back-projected to yield the reconstructed image.

The major difference between this method and the previous method of Sec. 4.3.4 is that the order of application of offset-detector weighting function, filtering, and backprojection is different. This method is known as the post-convolution weighting function because offset-detector weighting is applied after ramp filtering. Carrying out the operations in this order has been known to reduce artifacts at high offset percentages (but at the cost of introducing some estimation errors in the reflection and splicing steps above) [2].s

Method III: Iterative reconstruction

An iterative reconstruction algorithm was formulated by combining compressed sensing based reconstruction [28, 38], iterative reconstruction for offset detector CT [1, 7], and some special modifications for interior reconstruction. The different steps of the algorithm are listed below.

First, the projection data $R_\beta(s)$ is denoted by the discrete notation $\overrightarrow{R} = \{R_i\}$ where $i = 1, 2, \ldots M$ (the number of detector pixels in all projections), and the image grid is denoted by $\overrightarrow{f} = \{f_j\}$ where $j = 1, 2 \ldots N = W \times H$ (W is the width and H is the height of the image).

1. **Projection completion**: The projection data $R_\beta(s)$ that was originally measured between $-\Delta \leq s \leq \Theta$ (Fig. 4.4B′), was then extrapolated at the outer edge (i.e. within $-\Delta' \leq s \leq -\Delta$, see Fig. 4.4J) by the same method as in Sec. 4.3.4. In Fig. 4.4B′, missing data is not filled with zeros as in Fig. 4.4B.

2. **Weighted SART**: Data consistency was enforced by a modified version of the SART algorithm of [35]:

$$f_j^{(k+1)} = f_j^{(k)} + \lambda\, w(s) \sum_{i \in P(\psi)} \frac{a_{ij}}{\sum\limits_{i \in P(\psi)} a_{ij}} \left(\frac{R_i - \mathbf{A}_i \overrightarrow{f^{(k)}}}{\sum\limits_{j=1}^{N} a_{ij}} \right) \tag{4.4}$$

   where k is iteration number, and $\mathbf{A}_i$ is a row of the system matrix composed of weight elements a_{ij}. $\mathbf{A}_i \overrightarrow{f^{(k)}}$ yields the forward-projected result at the i^{th} detector bin. The summation of a_{ij} over $i \in P(\psi)$ is over all rays intersecting j^{th} pixel at fixed angle ψ. The relaxation parameter λ was chosen to be 0.8.

   - The main modification from [35] was that the redundancy weighting technique of [1, 7] was integrated by using the weighting function $w(s)$ (Eq. 4.2).

3. **TV minimization**: TV minimization by gradient descent was employed [38]. α parameter for TV minimization was set at 0.2, and number of TV iterations was set at 5. Resultant image after one iteration of SART+TV is shown in Fig. 4.4K.

4. **Projection correction**: The extrapolated sinogram data $R_\beta(s)$ within $-\Delta' \leq s \leq -\Delta$ is replaced by the corresponding part of the forward projected sinogram $\mathbf{A}\overrightarrow{f^{(k)}}$ (Fig. 4.4L). The splicing technique of [2] was employed to ensure smooth merging of measured and forward-projected data around $s = -\Delta$.

5. Steps 2, 3, 4 were repeated till convergence criterion was met, or maximum number of iterations was reached.

The importance of each of the above steps is discussed in Sec. 4.4.3.

Effective-ROI reconstruction (simulations only)

Due to offset detector acquisition, the fan-beam data is acquired in the range $-\Delta \leq s \leq -\Theta$. In our simulations, we also acquired projections over the larger detection range $-\Delta \leq s \leq \Delta$. Such a sinogram does not require special handling for offset detector acquisition. Projection completion was performed in the same way as Sec. 4.3.4. Fan-beam FBP and SART-TV algorithms were then employed to yield the reconstructed image. The reconstructions by this

method were termed as 'effective-ROI' reconstruction. Effective-ROI reconstruction by FBP was used as a baseline to quantify the performance of methods I (Sec. 4.3.4) and II (Sec. 4.3.4), while effective-ROI reconstruction by SART-TV was used as a baseline for method III (Sec. 4.3.4).

4.3.5 Image quality analysis

The two methods I and II described in Sec. 4.3.4 carry out two different operations – accounting for the offset detector acquisition, and extrapolating the truncated projections before FBP. In the numerical simulations, we wanted to study the effect of each operation separately, and hence designed our reconstruction metrics accordingly.

The first basis of comparison was the effective-ROI reconstruction described in Sec. 4.3.4. By this comparison, the effect of projection truncation was excluded, and the only difference was the way by which the offset detector acquisition was handled by methods I and II. The reconstructed images were compared with the effective-ROI reconstruction by means of line profiles, and relative root mean square error (RRME, calculated according to [30]).

Next, the reconstructed images were compared to the ground truth of the numerical phantom. Again, the tools for comparison were line profiles and RRME calculations w.r.t. the ground truth. By this method, the combined effect of all the steps comprising methods I and II could be evaluated.

4.4 Results

4.4.1 Results: numerical simulations

Visual analysis

The truncated projections of the double Shepp-Logan phantom acquired at different detector offset percentages were reconstructed by all the methods listed in Sec. 4.3.4. The reconstructed images are shown in Fig. 4.5. The reconstruction for 0% detector offset case (first column) shows the extent of the ROI that can be imaged without detector offset. As we increase the detector offset from 0% to 9.4% and so on, the extent of the ROI continuously increases. The same trend is observed for methods I (top row), II (middle row) and III (bottom row).

The reconstruction in all the images appears to be good, except for subfigure F, where a major artifact is observed at the center. This shows a limitation of method I – for a highly offset detector, the range of over-sampled data $-\Delta \leq s \leq \Delta$ is very narrow. After applying the smooth fan-beam weighting scheme to the inner edge of the sinogram, a sharp

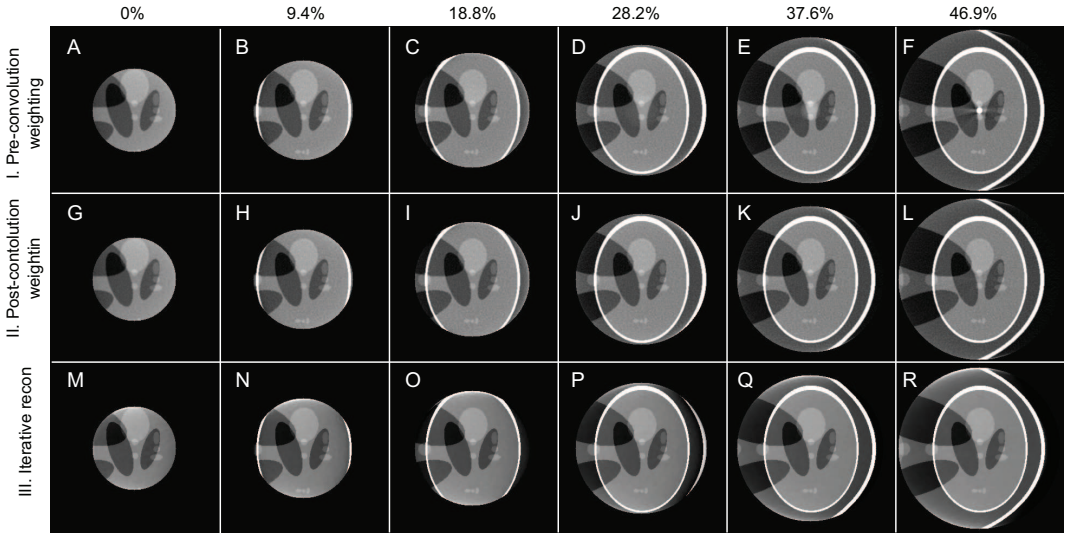

Figure 4.5: Reconstructed images for numerical simulations. Images were reconstructed at different detector offset percentages $(0, 9.4\%, \ldots 46.9\%)$ by using three reconstruction methods – pre-convolution weighting (*top row*), post-convolution weighting (*middle row*), and iterative reconstruction (*bottom row*).

transition still remains. Such a sharp transition is then amplified by the ramp filter of FBP algorithm to generate artifacts in the center of the reconstructed image [11]. The corresponding reconstructions by methods II and III (Figs. 4.5L and 4.5R, respectively) do not have the same artifact.

For better analysis of the image artifacts, the reconstructed images of Fig. 4.5 were subtracted from the corresponding effective-ROI reconstructions. The difference images are shown in Fig. 4.6. Such comparison with the effective-ROI reconstruction allows us to isolate the error in handling of offset-detector acquisition from the error in the projection completion step. The images in top-row of Fig. 4.6 clearly show that error by method I increases with the increase in detector offset percentage. The images for method II (middle-row) show that the artifact is almost negligible, except for subfigure L. The artifact in subfigure L is still much smaller than the corresponding artifact for method I (subfigure F). However method III (bottom row) shows the best performance, as there are no visible differences from the effective-ROI reconstruction at any detector offset percentage.

Line profiles

Fig. 4.7 compares the horizontal line profiles for the three reconstruction methods I, II and III at the 37.6% detector offset case. These plots also show the line profiles by global reconstruction and effective-ROI reconstruction (by FBP in subfigures I and II, and by

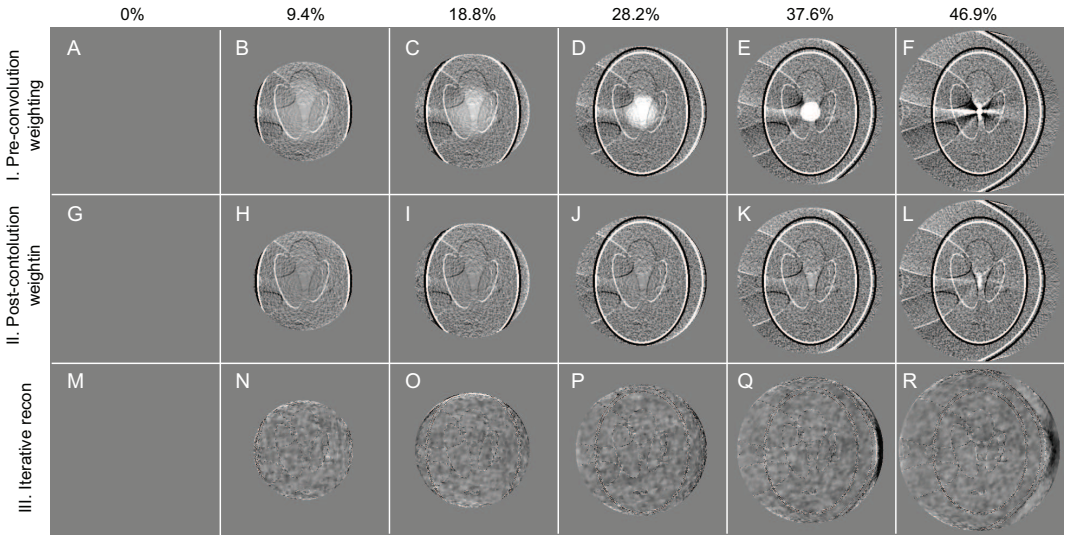

Figure 4.6: Difference of reconstructed image w.r.t. effective-ROI reconstruction. Images are shown at different detector offset percentages $(0, 9.4\%, \ldots 46.9\%)$ by using three reconstruction methods – pre-convolution weighting (*top row*), post-convolution weighting (*middle row*), and iterative reconstruction (*bottom row*).

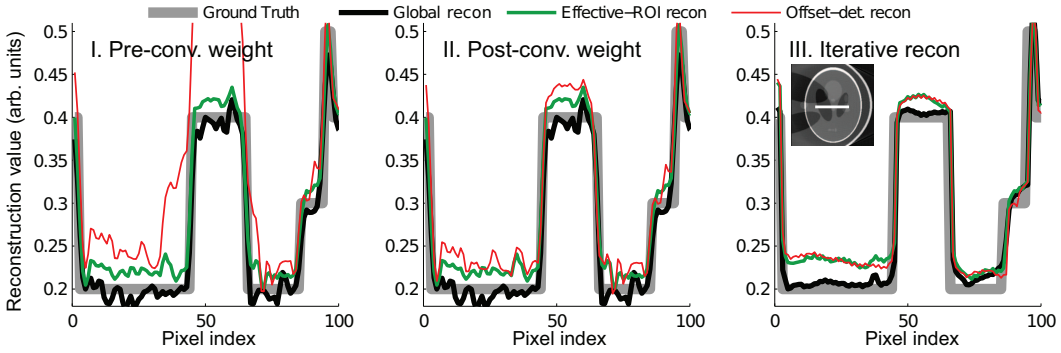

Figure 4.7: Line profiles for numerical simulations. Line profiles were measured across line marked in inset of subfigure III for 37.55% detector offset case and for three reconstruction methods: (I) pre-convolution weighting, (II) post-convolution weighting, and (III) iterative reconstruction. Algorithm used for global reconstruction and effective-ROI reconstruction is FBP in subfigures I and II, and SART-TV in subfigure III.

SART-TV in subfigure III). The effective-ROI reconstruction has a DC bias compared to the global reconstruction – this is due to projection truncation w.r.t. the global sample only [8] (as there is no offset detector acquisition here). It is worth noting that the best reconstruction of offset detector data is expected to approach the effective-ROI reconstruction, and is not expected to improve beyond this.

For the offset detector acquisition, we observe that the line profile for method I is significantly different from the effective-ROI reconstruction. The reconstruction line profile of method II closely matches the line profile of effective-ROI reconstruction. This reiterates the earlier observation that method II outperforms method I at high detector offsets.

For method III, the global reconstruction by SART-TV is better than the global reconstruction by FBP. This happens because the numerical phantom is piece-wise constant, and TV minimization tends to achieve higher reconstruction accuracy than FBP for such objects [28]. However, more interesting is the fact that offset detector reconstruction by method III is almost identical to effective-ROI reconstruction. This hints that the iterative reconstruction based method III may be able to surpass the post-convolution weighting based method II.

Error analysis

RRME plots in Fig. 4.8 provide further insights into the reconstruction results. First RRME is calculated w.r.t. the ground truth and we plot the values in Fig. 4.7A. We find that for method I, the error steadily increases as detector offset is increased. This is due to the fact that method I performs badly at higher detector offset percentages, and the artifacts degrade the reconstruction accuracy.

In contrast to method I, the error for method II keeps decreasing as detector offset is increased. This decrease in error w.r.t. global reconstruction reflects a reduction in DC bias with increasing detector offset. This is an important observation – while an increase in the extent of the ROI is a direct consequence of acquiring scans with an offset detector, the error reduction is an indirect but advantageous effect. We also found that this advantageous trend was not observed if we did not use the boundary information as additional knowledge in the projection completion step. This can be heuristically explained by the fact that with high detector offset and a finite object boundary, the amount of unknown information (that has to be guessed by the extrapolation step) is reduced. Thus the DC bias in the final reconstruction (that is an effect of extrapolation error) is consequently reduced.

The reconstruction accuracy for method III initially decreases with increasing detector offset, but then the trend does not hold for higher detector offsets. The performance of method III at higher detector offsets may be improved by an improved projection completion step in Sec. 4.3.4. Nevertheless, the error by method III is lesser than methods I and II for all detector offset cases.

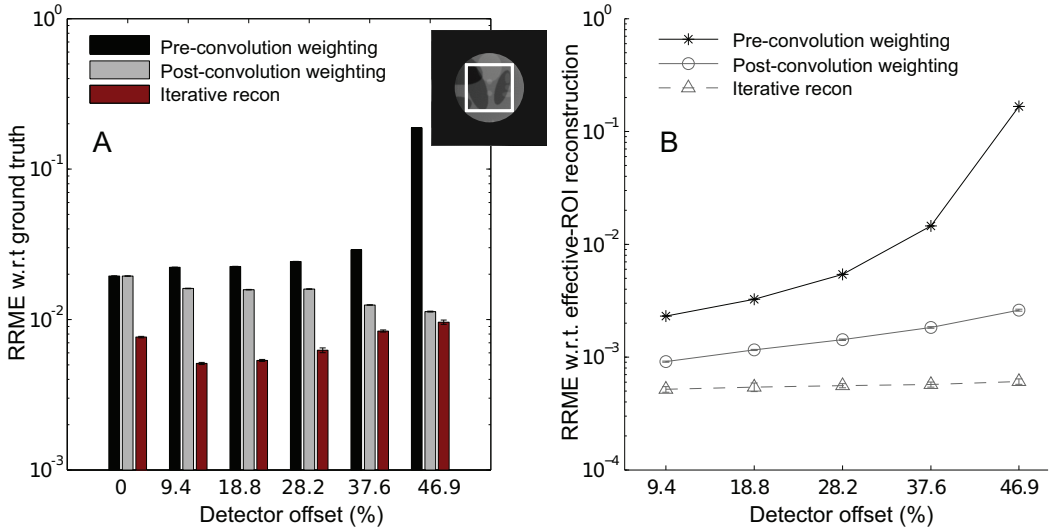

Figure 4.8: Plots of reconstruction error in numerical simulation. (A) Relative root mean square error (RRME) w.r.t. ground truth. Error at different detector offset percentages are plotted for all three reconstruction methods. (*Inset:*) The ROI used for error calculation is marked on the reconstruction of the 0% detector offset case. (B) RRME w.r.t. effective-ROI reconstruction for all the reconstruction methods. The y-axis is plotted on a logarithmic scale for both the plots.

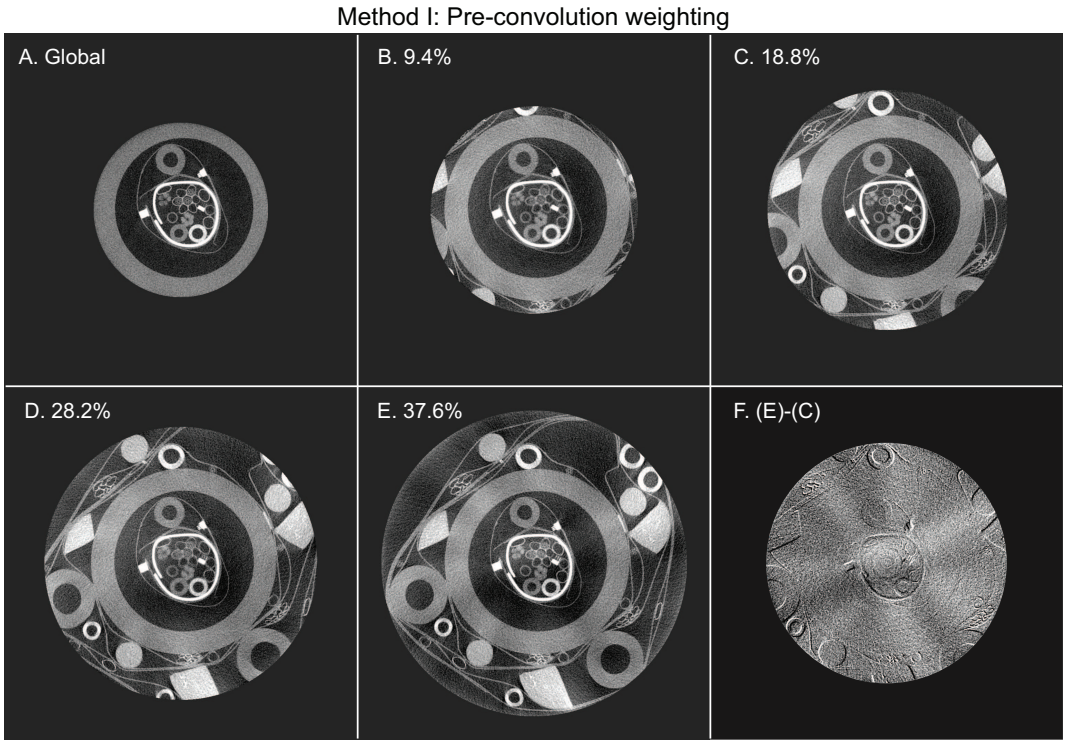

Figure 4.9: Reconstruction of micro-CT phantom by method I. (A-E) Reconstructed images of micro-CT phantom at different detector offset percentages $(0, 9.4\%, \ldots 37.6\%)$ by using method I. (F) Difference image of images E and C (only ROI of C is shown).

Next RRME was calculated w.r.t. the effective-ROI reconstruction and plotted in Fig. 4.7B. The error calculated by this way excludes the effect of projection completion and isolates the error due to improper handling of offset detector acquisition. It is observed that this error increases steadily with increase in detector offset for method I, but the rate of increase is much lower in case of method II. Finally, the error is almost constant for method III at all detector offsets. This shows that method III has the best ability to handle the offset detector acquisition as compared to methods I and II. Also it is worth noting that the y-axis for both plots in Fig. 4.8 are plotted on a logarithmic scale. Thus, in some cases, the error performance differs by almost one or two orders of magnitude.

4.4.2 Experimental results

The reconstruction results for the micro-CT phantom are shown in Fig. 4.9 for method I, Fig. 4.10 for method II, and Fig. 4.11 for method III. The reconstruction is carried out for acquisitions for detector offset percentage equal to 0%, 9.4%, 18.8%, 28.2%, and 37.6% (there was a problem with the acquisition at 46.9%, and this result is not included). In each figure,

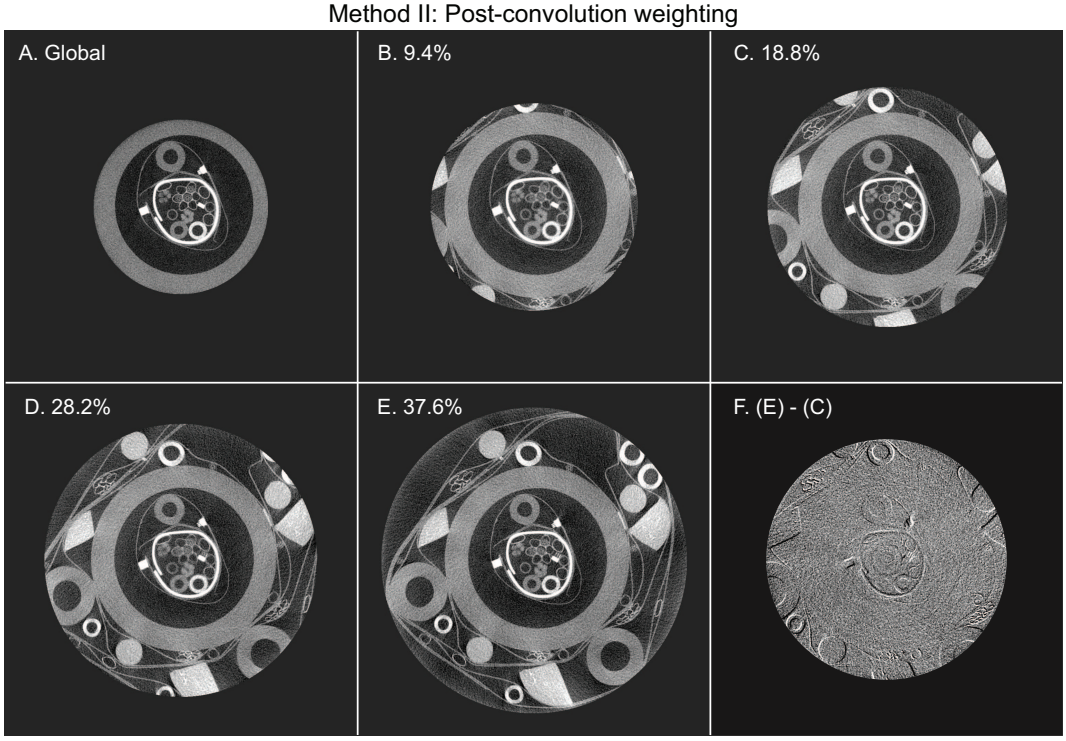

Figure 4.10: Reconstruction of micro-CT phantom by method II. (A-E) Reconstructed images of micro-CT phantom at different detector offset percentages $(0, 9.4\%, \ldots 37.6\%)$ by using method II. (F) Difference image of images E and C (only ROI of C is shown).

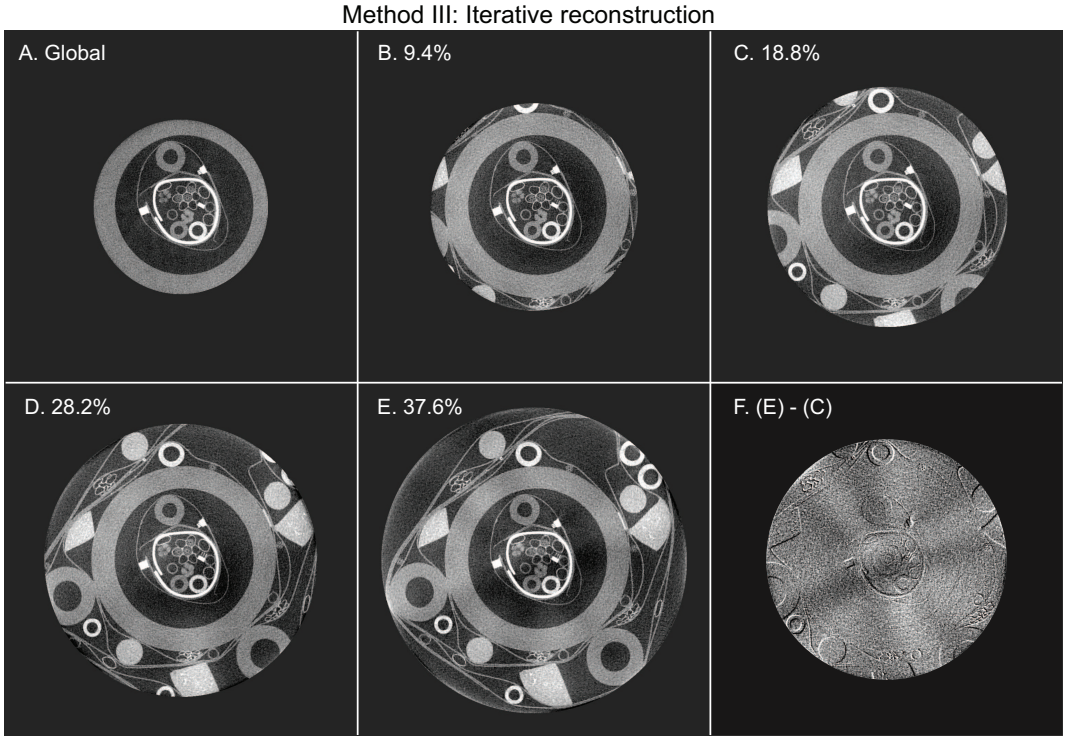

Figure 4.11: Reconstruction of micro-CT phantom by method III. (A-E) Reconstructed images of micro-CT phantom at different detector offset percentages $(0, 9.4\%, \ldots 37.6\%)$ by using method III. (F) Difference image of images E and C (only ROI of C is shown).

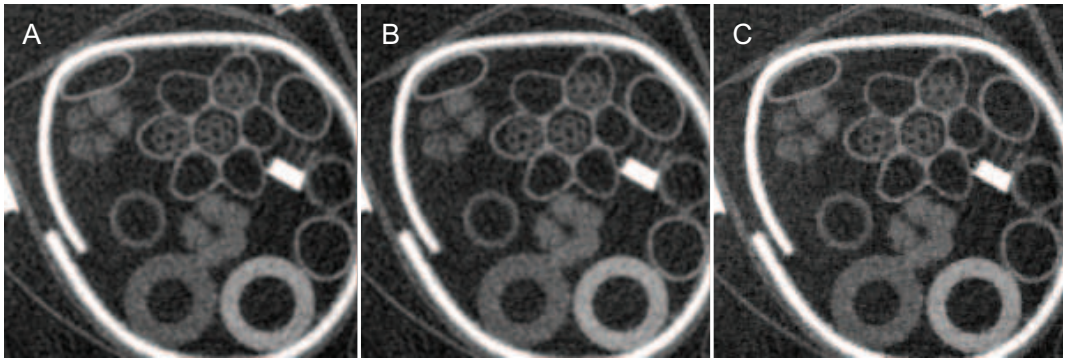

Figure 4.12: Central ROI for three reconstruction methods. The central ROI is shown for 18.8% detector offset case for three reconstruction methods: (A) pre-convolution weighting, (B) post-convolution weighting, and (C) iterative reconstruction.

the increase in the extent of the ROI with increase in detector offset is evident. However shading artifacts are visible at higher detector offsets for both method I (Figs. 4.9C-E) and method III(Figs. 4.11C-E). These are left-right shading artifacts similar to those observed in previous studies on offset detector reconstruction [7]. Figure 4.10 shows that the shading artifacts are much lesser in case of method II though minor artifacts still exist at the highest detector offset case (Fig. 4.10E).

Subfigure F in each of Figs. 4.9, 4.10 and 4.11 displays the difference of the reconstructions at 37.6% and 18.8% detector offsets. The difference image highlights the presence of shading artifacts at high detector offsets. Figures 4.9F and 4.11F show that there are distinct shading artifacts for methods I and III. For method II, Fig. 4.10F shows that the shading artifact is almost negligible.

Figure 4.12 shows the central ROI by all the reconstruction methods for the 18.8% detector offset case. This figure shows that the reconstruction quality is almost identical for all three methods. The first two methods are analytical reconstruction methods that use fan-beam FBP reconstruction, and are expected to have similar reconstruction quality. Method III is an iterative reconstruction process, and was made to achieve similar reconstruction quality as FBP by careful tuning of the iteration parameters.

4.4.3 Comments on method III

Importance of the different steps

The importance of each of the steps in Method III (Sec. 4.3.4) are explained below:

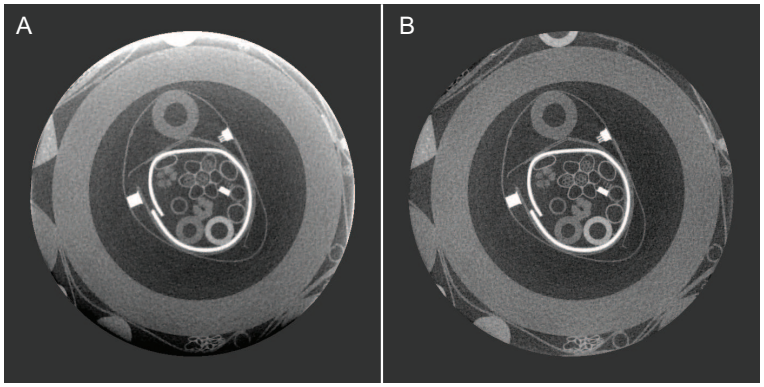

Figure 4.13: Effect of projection completion. Central ROI by method III for the 9.4% detector offset case, (A) without using projection completion, and (B) with projection completion.

1. The **projection completion** step is carried out to handle the sharp object truncation at the outer edge. If iterative reconstruction is carried out without projection completion, strong bias artifacts are observed within the reconstruction ROI as shown in Fig. 4.13A. With the projection completion step, the bias artifact is completely removed as shown in Fig. 4.13B. Since the extrapolated portion of the sinogram is an approximation of the underlying truth, the corresponding reconstruction outside the ROI is also approximate. But we are not interested in the reconstruction values outside the ROI, and the image is cropped back to the ROI for display after reconstruction.

2. Previous studies [7, 1] showed the advantage of using a smooth weighting function to modify the projection updates (i.e. **weighted SART**).

3. **TV minimization** was incorporated as it allows improvement of the noise characteristics of iterative reconstruction [28]. TV minimization has also been shown to allow few-view reconstruction for offset detector CT [1].

4. The iteration update of Eq. 4.4 minimizes the objective $\| \overrightarrow{R} - \mathbf{A} \overrightarrow{f} \|^2$. However the extrapolated portion of the sinogram $R_\beta(s)$ in $-\Delta' \leq s \leq -\Delta$ should not be considered during the minimization process. The **projection correction** step ensures that only the measured portion i.e. in $-\Delta \leq s \leq \Theta$ of the sinogram contributes to the minimization process. Also the backprojection-reprojection process improves the quality of sinogram completion e.g. the forward projected sinogram data obeys the sinogram consistency conditions[36], but the sinogram data after basic projection completion by cosine-extrapolation [32] does not.

Guidelines for improvement

The numerical simulation in Sec. 4.4.1 showed that the iterative technique of method III provided more accurate reconstruction than analytic methods. Among the analytic methods, method II (post-convolution weighting) was better than method I (pre-convolution weighting) especially at higher detector offsets. These trends are similar to those observed in previous studies on 'global' reconstruction with offset detector array [2, 7].

In the tests on real data (Sec. 4.4.2), we observed that method II performed the best. Methods I and III both suffered from significant shading artifacts especially at high detector offset (see Figs. 4.9E and 4.11E), but the same artifact was much lesser in case of method II (Fig. 4.10E). This result was contrary to observations in previous studies where iterative reconstruction performed better than analytic methods [1, 7]. Thus there is scope for further improvements in the iterative reconstruction framework for offset detector CT.

One of the important differences between the current study and previous studies is that an approximate projection extrapolation step had to be incorporated in this study. To decide whether this was the culprit behind the shading artifacts, we tried different extrapolation techniques to see if the shading artifact changed. However the shading artifact was not altered by changing the extrapolation methods. This leads us to believe that the projection completion step does not cause the shading artifact.

As detailed in Sec. 4.3.4, method II uses a fan-beam completion step to estimate the portion of the sinogram missing due to offset detector acquisition. Then it employs ramp filtering, following which the filtered projections are multiplied by the weighting function and back-projected. By using this sequence of steps, the ramp filtering does not meet any sharp truncation edge. And even though the filtering is approximate, the net result is that the artifacts are reduced. In the iterative reconstruction framework of method III, ramp filtering is not involved. Yet the weighted projection updates act across a sharp truncation edge, and this seems to have a similar effect as ramp filtering across a sharp edge. A possible solution would be to design a modified iterative reconstruction framework that incorporates local approximations by using complementary fan-beam data (i.e. sinogram reflection [18]) when dealing with the truncation edge.

4.5 Conclusions and Discussion

Offset detector acquisition has previously been shown to increase the size of the scan FOV to up to twice the original size. However previous studies assumed that the entire sample was covered as a result of offset detector acquisition. In this study, we focused on the case when the extended FOV still covers an internal ROI within a much larger sample. We developed three reconstruction methods (Sec. 4.3.4) that extend previous analytic and iterative reconstruction techniques to handle interior tomography with an offset detector

array. Then we demonstrated the efficacy of the algorithms by applying them in numerical simulations and on real data acquired on an in-house scanner. In numerical simulations, we made the interesting observation that the offset detector acquisition has the indirect effect of reducing the DC bias artifact of interior reconstruction (Sec. 4.4.1, and Fig. 4.8A). This trend was observed when the knowledge of object boundary was incorporated. We note here that additional knowledge like a low-resolution global scan [20, 24, 31] can easily be incorporated into our methods to further reduce the interior reconstruction artifact.

In the numerical simulations, the iterative algorithm (method III, see Sec. 4.3.4) provided the highest reconstruction accuracy in terms of relative root mean square error w.r.t. the ground truth and the effective-ROI reconstruction. The TV constraint in our iterative reconstruction technique enforces the piece-wise constancy constraint, and this ensures highly accurate reconstruction for the double Shepp-Logan phantom that is also piece-wise constant. However more interesting is the trend by which the iterative technique is also able to better recover the missing data due to offset detector acquisition (see Sec. 4.4.1, and Fig. 4.8B).

Next, we tested the reconstruction techniques on a real dataset acquired with an offset detector array. All three methods were able to increase the ROI extent, and the performance in terms of the high-frequency features was the same for all methods. However method II (post-convolution weighting, Sec. 4.3.4) proved to be the most robust. There were some low-frequency shading artifacts by the iterative technique. Such artifacts have not been reported before for iterative technique, and our study showed that more work still needs to be done to improve the iterative reconstruction framework. We also provided some guidelines for such improvements in Sec. 4.4.3.

Bibliography

[1] Junguo Bian, Jiong Wang, Xiao Han, Emil Y Sidky, Lingxiong Shao, and Xiaochuan Pan. Optimization-based image reconstruction from sparse-view data in offset-detector CBCT. *Physics in medicine and biology*, 58(2):205–30, January 2013.

[2] Paul S Cho, Anthony D Rudd, and Roger H Johnson. Cone-beam CT from width-truncated projections. *Computerized medical imaging and graphics*, 20(1):49–57, 1996.

[3] Marius Costin, Delphine Lazaro-Ponthus, Samuel Legoupil, Philippe Duvauchelle, and Valérie Kaftandjian. A 2D multiresolution image reconstruction method in X-ray computed tomography. *Journal of X-ray science and technology*, 19(2):229–47, January 2011.

[4] Bruno De Man and Samit Basu. Distance-driven projection and backprojection in three dimensions. *Physics in Medicine and Biology*, 49(11):2463–2475, June 2004.

[5] M Feser, J Gelb, H Chang, H Cui, F Duewer, S H Lau, A Tkachuk, and W Yun. Sub-micron resolution CT for failure analysis and process development. *Measurement Science and Technology*, 19(9):094001, September 2008.

[6] J Gregor, SS Gleason, and MJ Paulus. Conebeam x-ray computed tomography with an offset detector array. In *Image Processing, 2003. ICIP 2003. Proceedings. 2003 International Conference on*, volume 2, pages II–803, 2003.

[7] Eberhard Hansis, Jörg Bredno, David Sowards-Emmerd, and Lingxiong Shao. Iterative Reconstruction for Circular Cone-Beam CT with an Offset Flat-Panel Detector. In *Nuclear Science Symposium Conference Record (NSS/MIC), 2010 IEEE*, pages 2228–2231, 2010.

[8] G.T. Herman and R.M. Lewitt. Evaluation of a preprocessing algorithm for truncated CT projections. *Journal of Computer Assisted Tomography*, 5(1):127–135, 1981.

[9] Jiang Hsieh. *Computed tomography: principles, design, artifacts, and recent advances.* SPIE Publications, 2003.

[10] Mahmoud Ismail, Katsuyuki Taguchi, Jingyan Xu, Benjamin M. W. Tsui, and Emad M. Boctor. 3D-guided CT reconstruction using time-of-flight camera. In *SPIE Medical Imaging*, pages 796429(1)–796429(11), March 2011.

[11] A.C. Kak and M. Slaney. *Principles of Computerized Tomographic Imaging*. Society of Industrial and Applied Mathematics, 2001.

[12] Hiroyuki Kudo, Matias Courdurier, Frédéric Noo, and Michel Defrise. Tiny a priori knowledge solves the interior problem in computed tomography. *Physics in medicine and biology*, 53(9):2207–31, May 2008.

[13] A Kyrieleis, V Titarenko, M Ibison, T Connolley, and P J Withers. Region-of-interest tomography using filtered backprojection: assessing the practical limits. *Journal of microscopy*, 241(1):69–82, January 2010.

[14] Shuai Leng, Tingliang Zhuang, Brian E Nett, and Guang-Hong Chen. Exact fan-beam image reconstruction algorithm for truncated projection data acquired from an asymmetric half-size detector. *Physics in medicine and biology*, 50(8):1805–20, April 2005.

[15] Vinson Liu, Nicholas R. Lariviere, and Ge Wang. X-ray micro-CT with a displaced detector array: Application to helical cone-beam reconstruction. *Medical Physics*, 30(10):2758, 2003.

[16] K Machin and S Webb. Cone-beam x-ray microtomography of small specimens. *Physics in medicine and biology*, 39(10):1639–57, October 1994.

[17] O. Nalcioglu, ZH Cho, and RY Lou. Limited Field of View Reconstruction in Computerized Tomography. *Nuclear Science, IEEE Transactions on*, 26(1):546–551, 1979.

[18] M Nassi, WR Brody, P Cipriano, P Stonestrom, C Morehouse, D Moss, and A Macovski. Application of a reflection technique for improved temporal resolution with dynamic and ECG-gated computed tomography. In *Proc. SPIE 0206 Recent and Future Developments in Medical Imaging II*, volume 103, 1979.

[19] Frédéric Noo, Rolf Clackdoyle, and Jed D Pack. A two-step Hilbert transform method for 2D image reconstruction. *Physics in Medicine and Biology*, 49(17):3903–3923, September 2004.

[20] D. Pak-Kong Lun and T.C. Hsung. Region-of-interest tomography using multiresolution interpolation. In *Acoustics, Speech, and Signal Processing, 1997. ICASSP-97., 1997 IEEE International Conference on*, pages 2825–2828, 1997.

[21] D.L. Parker. Optimal short scan convolution reconstruction for fanbeam CT. *Medical Physics*, 9:254, 1982.

[22] M J Paulus, S S Gleason, S J Kennel, P R Hunsicker, and D K Johnson. High resolution X-ray computed tomography: an emerging tool for small animal cancer research. *Neoplasia (New York, N.Y.)*, 2(1-2):62–70, 2008.

[23] Erik L Ritman. Micro-computed tomography-current status and developments. *Annual review of biomedical engineering*, 6:185–208, January 2004.

[24] B Sahiner and a E Yagle. Region-of-interest tomography using exponential radial sampling. *IEEE transactions on image processing : a publication of the IEEE Signal Processing Society*, 4(8):1120–7, January 1995.

[25] Dirk Schafer, Michael Grass, and Peter van de Haar. FBP and BPF reconstruction methods for circular X-ray tomography with off-center detector. *Medical Physics*, 38(S1):S85, 2011.

[26] J. D. Schiffbauer, S. Xiao, Kriti Sen Sharma, and G. Wang. The origin of intracellular structures in Ediacaran metazoan embryos. *Geology*, 40(3):223–226, January 2012.

[27] Kriti Sen Sharma, Christian Holzner, Dragos M Vasilescu, Jin Xin, Shree Narayanan, Masoud Agah, E. A. Hoffman, Hengyong Yu, and Ge Wang. Scout-view Assisted Interior Micro-CT. *Physics in Medicine and Biology*, 2013.

[28] Kriti Sen Sharma, Xin Jin, Christian Holzner, Shree Narayanan, Baodong Liu, Dong Wang, Masoud Agah, Linbing Wang, Hengyong Yu, and Ge Wang. Experimental studies on few-view reconstruction for high-resolution micro-CT. *Journal of X-ray science and technology*, 21(1):25–42, January 2013.

[29] Stuart R. Stock. *MicroComputed Tomography: Methodology and Applications*. CRC Press, 2008.

[30] Jie Tang, Brian E Nett, and Guang-Hong Chen. Performance comparison between total variation (TV)-based compressed sensing and statistical iterative reconstruction algorithms. *Physics in medicine and biology*, 54(19):5781–804, October 2009.

[31] G. Tisson, P. Scheunders, and D. Van Dyck. 3D region of interest x-ray CT for geometric magnification from multiresolution acquisitions. In *2004 2nd IEEE International Symposium on Biomedical Imaging: Macro to Nano (IEEE Cat No. 04EX821)*, volume 2, pages 567–570. Ieee, 2004.

[32] Greg Tisson. *Reconstruction from transversely truncated cone beam projections in microtomography*. PhD thesis, Universiteit Antwerpen, Belgium, 2006.

[33] Gert Van Gompel. *Towards accurate image reconstruction from truncated x-ray CT projections*. PhD thesis, University of Antwerp, 2009.

[34] Ge Wang. X-ray micro-CT with a displaced detector array. *Medical Physics*, 29(7):1634, 2002.

[35] Ge Wang and Ming Jiang. Ordered-subset simultaneous algebraic reconstruction techniques (OS-SART). *Journal of X-ray Science and Technology*, 12:169–177, 2004.

[36] Jingyan Xu, Katsuyuki Taguchi, and BMW Tsui. Statistical projection completion in x-ray CT using consistency conditions. *IEEE transactions on medical imaging*, 29(8):1528–40, August 2010.

[37] T Yamashita, Y Nabeshima, and M Noda. High-resolution micro-computed tomography analyses of the abnormal trabecular bone structures in klotho gene mutant mice. *The Journal of endocrinology*, 164(2):239–45, February 2000.

[38] H Yu and G Wang. Compressed sensing based interior tomography. *Physics in medicine and biology*, 54(9):p2791–2805, 2009.

[39] Lifeng Yu, Charles Pelizzari, and Xiaochuan Pan. Application of asymmetric cone-beam CT in radiotherapy. In *Nuclear Science Symposium Conference Record, 2004 IEEE*, volume 5, pages 3249—-3252, 2004.

Chapter 5

Conclusion

5.1 Contributions of this work

The following contributions have been made in this work:

I. Scan times in micro-CT scanners may range anywhere between 30 minutes to 6+ hours [4, 10]. The long scan times of micro-CT scanners are especially problematic when numerous scans are desired as part of a study, or in a routine process. In **chapter 2**, we showed that a CS based reconstruction technique can significantly reduce the number of views and yet achieve high quality reconstruction. The argument is supported by numerical simulations and tests on real data acquired on the Xradia MicroXCT-400 scanner. For performance characterization, a novel micro-CT phantom was also fabricated. As compared to conventional FBP techniques, the new techniques achieved similar reconstruction quality with only $1/8^{th}$ the number of views. The reduction in number of views, and consequently in scanning time, is an important enhancement in the capability of micro-CT scanners.

II. According to tomographic reconstruction theory, x-rays need to cover the entire sample so that the object may be uniquely reconstructed [12]. In micro-CT, the object of interest is often larger than the scan field-of-view (FOV). In such cases, the projections are truncated, and reconstruction of truncated projections leads to two kinds of artifacts – a cupping artifact at the edges (leading to a loss in resolution), and a difference in CT numbers (a DC bias) w.r.t. the global reconstruction [3, 7, 17]. Previously, multi-resolution techniques have been developed that used a low-resolution global scan (in addition to the high-resolution truncated scan) to correct the interior artifacts [9, 11, 13, 14, 15]. However previous studies used a fully sampled global scan which drastically increased the scanning overhead. Also most previous methods placed severe restrictions on the scan geometries for multi-resolution acquisition.

In **chapter 3**, we developed two new reconstruction methods that achieved accurate interior reconstruction with only a limited number of global projections / scout views as additional information. Thus, the scanning overhead for multi-resolution scans was greatly reduced. Of the two methods, the first method is a simple extension of previous multi-resolution techniques, but this method still placed a restriction on the scan geometry of the global scout views vis-à-vis the high-resolution truncated scan. The second technique combined CS based reconstruction with multi-resolution methods to achieve accurate interior reconstruction. Also, this method did not place any restrictions on the relative scan geometries. The two methods proposed here were tested on two different numerical phantoms, and two typical micro-CT datasets.

III. While the previous chapter focuses on the accuracy of interior reconstruction, **chapter 4** deals with the size of an interior ROI that can be imaged with a fixed sized detector. Previous studies have shown that with offset detector acquisition, the scan FOV may be increased by up to twice its original size [2, 16]. However all previous methods assumed that the scan FOV (after offset detector acquisition) covered the entire sample i.e. the problem of interior artifacts was circumvented by acquiring a global scan with offset detector geometry.

   Equally interesting is the case when, even after acquiring projections with an offset detector, the scan FOV still covers an interior ROI, albeit of a larger size. The larger ROI is advantageous on many occasions, especially when the detector size is limited, and we want to maximize the scanned area within the sampled object. Here, the increased extent of the ROI takes a higher priority over accuracy of the interior. Yet, no new artifacts should be introduced just by the offset acquisition process. In our study, we extended previous analytic and CS based iterative techniques of 'global' offset detector CT [1, 2, 5, 6, 8, 16, 18] to the proposed interior offset detector case. The new methods were tested in numerical simulations and on real data. In numerical simulations, the CS based technique provided the highest accuracy. Yet, the CS based technique suffered from certain artifacts in case of a real dataset that had various imperfect properties. To counter these artifacts, important guidelines were provided for future developments.

5.2 Future research directions

The above contributions support our original claim that compressed sensing (CS) based reconstruction methods can enhance the imaging capability of micro-CT scanners. Yet, there are many avenues of future research that would complement and enhance the findings of this study. Some future research directions are noted below:

i. Further optimization of the iterative algorithms to reduce the computational burden

ii. Development of truly open-source image reconstruction libraries and data archives

iii. Further improvements in interior tomography with an offset detector array, especially within the iterative framework so that existing shading artifacts are removed.

Bibliography

[1] Junguo Bian, Jiong Wang, Xiao Han, Emil Y Sidky, Lingxiong Shao, and Xiaochuan Pan. Optimization-based image reconstruction from sparse-view data in offset-detector CBCT. *Physics in medicine and biology*, 58(2):205–30, January 2013.

[2] Paul S Cho, Anthony D Rudd, and Roger H Johnson. Cone-beam CT from width-truncated projections. *Computerized medical imaging and graphics*, 20(1):49–57, 1996.

[3] Marius Costin, Delphine Lazaro-Ponthus, Samuel Legoupil, Philippe Duvauchelle, and Valérie Kaftandjian. A 2D multiresolution image reconstruction method in X-ray computed tomography. *Journal of X-ray science and technology*, 19(2):229–47, January 2011.

[4] M Feser, J Gelb, H Chang, H Cui, F Duewer, S H Lau, A Tkachuk, and W Yun. Sub-micron resolution CT for failure analysis and process development. *Measurement Science and Technology*, 19(9):094001, September 2008.

[5] J Gregor, SS Gleason, and MJ Paulus. Conebeam x-ray computed tomography with an offset detector array. In *Image Processing, 2003. ICIP 2003. Proceedings. 2003 International Conference on*, volume 2, pages II–803, 2003.

[6] Eberhard Hansis, Jörg Bredno, David Sowards-Emmerd, and Lingxiong Shao. Iterative Reconstruction for Circular Cone-Beam CT with an Offset Flat-Panel Detector. In *Nuclear Science Symposium Conference Record (NSS/MIC), 2010 IEEE*, pages 2228–2231, 2010.

[7] G.T. Herman and R.M. Lewitt. Evaluation of a preprocessing algorithm for truncated CT projections. *Journal of Computer Assisted Tomography*, 5(1):127–135, 1981.

[8] Vinson Liu, Nicholas R. Lariviere, and Ge Wang. X-ray micro-CT with a displaced detector array: Application to helical cone-beam reconstruction. *Medical Physics*, 30(10):2758, 2003.

[9] Clemens Maaß, Michael Knaup, and Marc Kachelrieß. New approaches to region of interest computed tomography. *Medical Physics*, 38(6):2868, 2011.

[10] Brian D Metscher. MicroCT for comparative morphology: simple staining methods allow high-contrast 3D imaging of diverse non-mineralized animal tissues. *BMC physiology*, 9:11, January 2009.

[11] O. Nalcioglu, ZH Cho, and RY Lou. Limited Field of View Reconstruction in Computerized Tomography. *Nuclear Science, IEEE Transactions on*, 26(1):546–551, 1979.

[12] Frank Natterer. *The mathematics of computerized tomography*. SIAM, 2001.

[13] D. Pak-Kong Lun and T.C. Hsung. Region-of-interest tomography using multiresolution interpolation. In *Acoustics, Speech, and Signal Processing, 1997. ICASSP-97., 1997 IEEE International Conference on*, pages 2825–2828, 1997.

[14] B Sahiner and a E Yagle. Region-of-interest tomography using exponential radial sampling. *IEEE transactions on image processing : a publication of the IEEE Signal Processing Society*, 4(8):1120–7, January 1995.

[15] G. Tisson, P. Scheunders, and D. Van Dyck. 3D region of interest x-ray CT for geometric magnification from multiresolution acquisitions. In *2004 2nd IEEE International Symposium on Biomedical Imaging: Macro to Nano (IEEE Cat No. 04EX821)*, volume 2, pages 567–570. Ieee, 2004.

[16] Ge Wang. X-ray micro-CT with a displaced detector array. *Medical Physics*, 29(7):1634, 2002.

[17] H Yu and G Wang. Compressed sensing based interior tomography. *Physics in medicine and biology*, 54(9):p2791–2805, 2009.

[18] Lifeng Yu, Charles Pelizzari, and Xiaochuan Pan. Application of asymmetric cone-beam CT in radiotherapy. In *Nuclear Science Symposium Conference Record, 2004 IEEE*, volume 5, pages 3249—-3252, 2004.

Appendix A

Other related work carried out during dissertation

This section lists some related projects carried out at the SBES advanced multi-scale CT facility (SAMCT) during the duration of this author's dissertation. The facility houses the micro- and nano-CT scanners used in this study, and is one of the only facilities in the world allowing x-ray imaging over a resolution range: 50 nm to 5 mm. Using the instrumentation and data from the facility, many collaborative interdisciplinary projects were initiated, and significant progress was made. These projects are listed briefly in this section.

System characterization

Accurate measurement of modulation transfer function (MTF), or alternatively point spread function, of an x-ray micro-CT system is essential for various purposes e.g. to determine scanner resolution, to retrieve further information about scanned object by image-processing, etc. In this project, a new method for MTF measurement was proposed that can be used with any resolution pattern and is more adept at studying MTF spatial variation than traditional method of using bar pattern analysis. Resolution target used to determine micro-CT resolution was scanned in a lab-based nano-CT system – the image from the nano-CT gave the 'ground truth' as shown in Figs. A.1a and b. The ground truth was quantitatively compared with micro-CT projection of same target (Fig. A.1c) to determine the point spread function of the system. Results matched well with bar pattern analysis, but the new method was able to study spatial variation while bar pattern analysis failed. More details are available in [9].

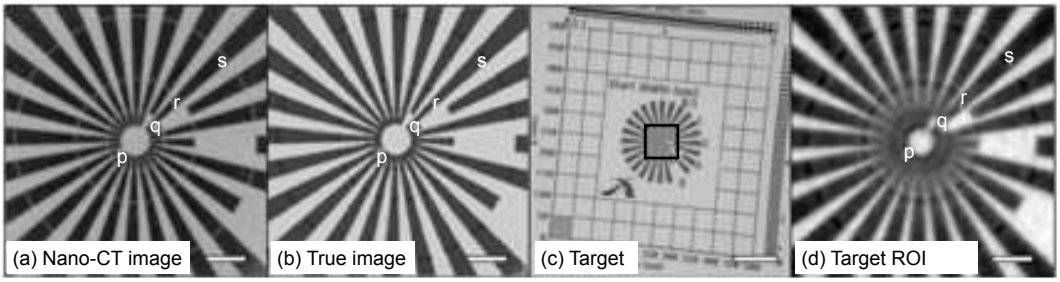

Figure A.1: Steps in matching of nano-CT and micro-CT images. **(a)** Nano-CT projection image of the resolution target, acquired by Xradia NanoXCT-100 system. **(b)** True image generated from the nano-CT projection after grayscale matching and scaling. **(c)** Target - A projection image of the same target using Xradia MicroXCT-400 40x objective. ROI in target image (marked by dotted bounding box in the middle), which is registered to true image, is used in proposed MTF calculation method. A much larger region in field-of-view is required to measure MTF by bar pattern analysis (marked by line on top). **(d)** Target ROI - Zoomed in view of ROI marked by dotted bounding box in (c) [Resolution pattern bar widths are marked in (a), (c) and (d): (p) 0.5 μm, (q) 1 μm, (r) 2 μm, and (s) 4 μm. Scale bar, marked at bottom right corner of each image, is 10 μm in (a), (b) and (d), and 100 μm in (c).]

Software infrastructure

There has been tremendous growth in open-source code development for image processing, signal processing, volume visualization etc. Some notable initiatives are VTK, ITK and ImageJ [1, 3], but there are many other projects. In the field of image reconstruction, there is still no coordinated effort to consolidate data and software specific to this field [6]. Also CT systems are typically 'closed' systems, and the specific details of scanner configuration are known only to the manufacturer. An unfortunate result of this is that many advances in inverse mathematics are never translated into the real world. This author made an effort in developing a community-based portal for sharing CT data and image reconstruction software. CT data that are used in Dr Wang's research group are archived on a web-server running Alfresco [2]. All codes for image reconstruction are available at the following link: https://bitbucket.org/bid/openrecon/

Application projects

This author worked closely with multiple collaborators on the micro- and nano-CT scanners, and contributed through training, sample preparation, experiment design, sample scanning, data analysis, volume visualization etc [8, 7, 10]

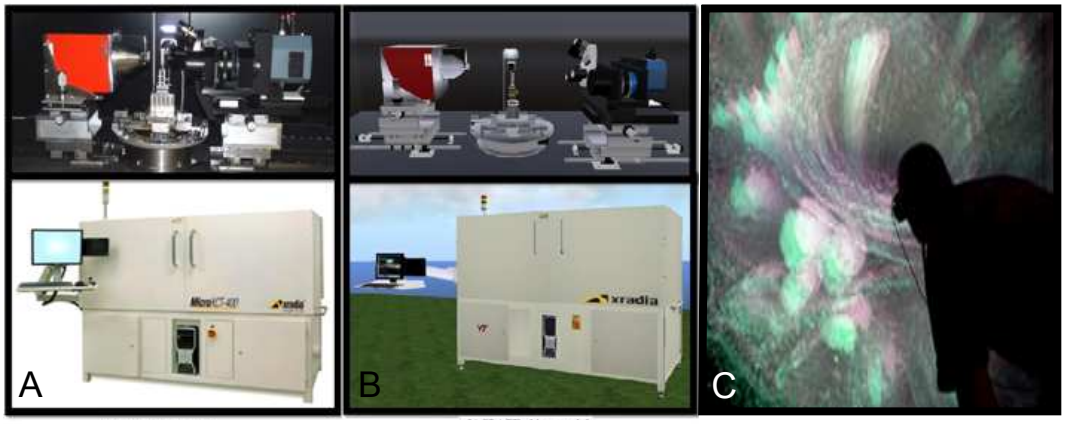

Figure A.2: Training and education, and volume visualization. (A) Xradia MicroXCT-400 scanner (bottom) and internal components (top). (B) Virtual replica in Second Life. (C) A participant experiencing a training data-set in the Viscube at Virginia Tech

Training and education

Training on micro- and nano- computed tomography (CT) scanners has been traditionally conducted via extensive practice on the instrument. This entails presence of an instructor to guide through the training procedure, until reasonable experience is attained. Modern tomographic instruments being expensive to maintain, the operational costs escalates with increasing number of training conducted. In a pioneering approach, the technical know-how to operate such equipment has been partly imparted via virtual reality environment running on the Second Life grid. In Fig. A.2A, the Xradia MicroXCT-400 scanner (bottom) and its internal components (top) is featured. An exact replica was created in Second Life (see Fig. A.2B) and used for training. Experimentation has indicated that self-learning on the virtual platform leads to a reduction of the total expert assisted training time. More details are available in [5]. In this project, this author contributed greatly in conceptualization of idea, design of virtual training environment, and manuscript writing.

Volume visualization

Volume visualization of 3D data-sets is typically carried out on 2D displays using various volume rendering techniques. The use of immersive virtual reality (VR) systems has been proposed, but there is little empirical research exploring effects of higher levels of immersion for volume visualization. A study was carried out to determine how various components of immersion influence the effectiveness of visualization in VR. It was found that there is significant benefit of analyzing volume data in an environment involving specific comments

of immersion; also that the components have variable influence depending on the volume analysis objectives. The research was published in [4]. This author contributed in research design, experimental set-up at Viscube (the VR set-up at Virginia Tech, which is shown in Fig. A.2C), determination of tasks used in user study, data analysis, manuscript writing, etc.

Bibliography

[1] M.D. Abràmoff, P.J. Magalhães, and S.J. Ram. Total Variation regulated iterative algorithms for microCT. *Biophotonics international*, 11(7):36–42, 2004.

[2] Alfresco Software Inc. Alfresco.

[3] L. Ibanez, W. Schroeder, L. Ng, and J. Cates. The ITK Software Guide. *Kitware Inc*, 2005.

[4] Bireswar Laha, Kriti Sensharma, James D Schiffbauer, and Doug A Bowman. Effects of Immersion on Visual Analysis of Volume Data. *IEEE Transactions on Visualization and Computer Graphics (Proceedings of Virtual Reality 2012, in press)*, 18(4), 2012.

[5] S. Mishra, Kriti Sen Sharma, S. J. Lee, E. A. Fox, and G. Wang. SLATE: Virtualizing multiscale CT training. *Journal of X-ray Science and Technology*, 20(3):383, 2012.

[6] Xiaochuan Pan, Emil Y Sidky, and Michael Vannier. Why do commercial CT scanners still employ traditional, filtered back-projection for image reconstruction? *Inverse problems*, 25(12):1230009, January 2009.

[7] James D Schiffbauer, Shuhai Xiao, Kriti Sen Sharma, and Ge Wang. The origin of intracellular structures in Ediacaran metazoan embryos. In *2011 GSA Annual Meeting*, Minneapolis, MN, 2011.

[8] James D Schiffbauer, Shuhai Xiao, Kriti Sen Sharma, and Ge Wang. The origin of intracellular structures in Ediacaran metazoan embryos. *Geology (in press)*, 2012.

[9] K. Sen Sharma, S. Seshadri, M. Feser, and G. Wang. Accurate Resolution Measurement for X-Ray Micro-CT Systems. In *AIP Conference Proceedings*, volume 1365, pages 337–340, 2011.

[10] K. Sen Sharma, D. M. Vasilescu, A. S. Kizhakke Puliyakote, E. A. Hoffman, T. Andric, J. W. Freeman, C. Markert, J. D. Schiffbauer, S. Xiao, H. Yu, and G. Wang. Novel Biomedical and Biological Applications using Lab-based Multi-scale CT System. In *Annual Meeting of the Biomedical Engineering Society*, Hartford, CT, 2011.

Appendix B

Program parameters

The program parameters for the different algorithms described in the thesis are outlined in this appendix.

B.1 Few-view micro-CT

In chapter 2, fan-beam FBP reconstruction was compared with SART-TV reconstruction for the application of few-view micro-CT. The starting point for both algorithms was the sinogram corresponding to the central slice of a cone beam tomography. The final output of the algorithms was an image reconstructed on a grid that was selected to be sufficiently large to fit the entire object. Reconstruction by the two algorithms was carried out as described below:

B.1.1 Fan-beam FBP

Micro-CT scans have two unique characteristics – short scan and center shift. As described in the appendix of chapter 2, both the characteristics were handled before applying fan-beam FBP reconstruction. First, the adjustment for short scan was applied to the sinogram by using the weighting scheme of Eq. 2.6. Next, Eq. 2.8 was applied to the weighted sinogram to account for center shift. The value of center-shift was calculated by reconstructing the sinogram first at many random values to find a region of good center-shift. Then a fine search was carried out in the approximate region to determine the actual center-shift. The commercial reconstruction software XMReconstructor provided by the scanner manufacturer Xradia (Pleasanton, CA) was used to determine the center-shift as it provides a graphical user interface (GUI) for this purpose. However the same can also be done without the GUI. After the two weighting schemes were applied in successive order, a traditional fan-beam

FBP algorithm was applied.

There are multiple implementations of fan-beam FBP algorithms available through commercial products (e.g. MATLAB, The Mathworks Inc., Natick, MA) and open-source platforms. However we implemented the entire FBP algorithm from scratch and made sure to use the same co-ordinate system as our SART-TV implementation (this reduced the possibility of differences in algorithm results due to differences in implementation). However, the FBP ultimately uses a pixel driven backprojector, while the SART-TV implementation uses a ray-driven projector and backprojector, so some differences are unavoidable.

The main parameter in the fan-beam FBP reconstruction is the choice of smoothing filter to accompany the ramp filter. We used the 'Hanning' filter implementation of the MATLAB `iradon` function. We found that the Hanning filter provided an optimum balance between resolution and noise performance.

Equation 2.9 represents the backprojection step of FBP. The exact details of implementing the backprojection for FBP algorithm are explained in A. C. Kak and Malcolm Slaney, *Principles of Computerized Tomographic Imaging*, IEEE Press, 1988.

After applying (1) short-scan weighting, (2) center-shift weighting, (3) Hanning filtering accompanied with ramp filtering, and (4) backprojection, the reconstructed image is obtained.

B.1.2 SART-TV

The SART-TV algorithm is an iterative reconstruction technique, and the details are provided in Sec. 2.5.2 and in the appendix of chapter 2. The program parameters are also listed in those sections.

B.2 Scout-view assisted interior micro-CT

For this study, four algorithms were implemented, and the program parameters for each are detailed below. The starting point for each of these algorithms was a truncated sinogram with data missing at the edges due to truncation. The final output of the algorithms was an image reconstructed on a grad that fit the truncated field-og-view (FOV). For the scout-interpolation and scout-reconstruction methods, two to eight scout views were also provided as additional information.

B.2.1 Truncated-FBP

In this technique (see Sec. 3.3.4), the truncation of the sinogram was handled by extrapolating the edges by using a Gaussian smoothing function i.e. the non-zero value at the

truncation edge was rolled off to zero, and the roll-off curve was a Gaussian kernel. The standard deviation of the Gaussian kernel was selected as 7.25% of the length of the truncated sinogram (the standard deviation of the Gaussian kernel determines the length of the roll-off).

Finally, fan-beam FBP was applied with the same program parameters as in Sec. B.1.1.

B.2.2 SS-SART-TV

A sequence subsets SART-TV (SS-SART-TV) implementation was used for this study. The references describing the algorithm and the parameters for SART-TV are detailed in Sec. 3.3.4. The SART-TV implementation was same as that in Sec. B.1.2. In our implementation of the sequence subsets SART-TV, we used the largest subset size (i.e. one ordered subset or OS containing all the projections) for first three iterations, two OS-s with half the projections in each OS for the next three iterations, four OS-s for the next three projections, and so on. Thus the number of OS-s in subsequent iterations was: 1, 1, 1, 2, 2, 2, 4, 4, 4, *ldots*. For an OS containing N projections, the projections were selected to be equally distributed within the angular range. In all, 23 iterations were carried out.

B.2.3 Scout interpolation

As detailed in Sec. 3.3.4, the first steps of the scout-interpolation methods involve up-sampling the scout-sinogram to the pixel width of the high-resolution sinogram, and then interpolating/extrapolating to all projection angles of the high-resolution sinogram. Because of these two interpolation operations, it is now possible to merge the global information from the scout-sinogram with the local information of the high-resolution sinogram. Both the up-sampling and the interpolation/extrapolation steps are achieved by the `interp1` 1-D data interpolation routine of MATLAB. Using the parameter selection choices of this routine, a cubic spline was fitted to the data to achieve the up-sampling/interpolation/extrapolation. As noted in Sec. 3.4.1, the extrapolation step was most prone to error and start- and end-angles for the scout-views should be selected carefully.

Finally FBP was carried out in the same way as in Sec. B.1.1.

B.2.4 Scout-reconstruction

The scout-reconstruction method is detailed in Sec. 3.3.4. In step 3, SS-SART-TV algorithm was used to reconstruct the scout-sinogram. All the parameters were same as in Sec. 3.3.4 and B.2.2, except that the number of TV iterations was set to 20, and the total number of iterations was set at 15. The image grid for the reconstruction was selected such that it fit

the entire object

Next, the reconstructed image was forward projected in the high-resolution geometry (Step 4 of Sec. 3.3.4. There were a few parameters to take care of during this procedure. First, the number of detector pixels for the forward projection was selected such that none of the projections were truncated. This was usually determined on a case-by-case basis as there was wide variation in the size of samples and the high-resolution geometry. Secondly, there was a change in co-ordinate axes while carrying out the forward projection i.e. while the earlier SS-SART-TV step was carried out in terms of the low-resolution scans, the forward projections had to be performed in the high-resolution geometry. As shown in Fig. 3.1, the centers of rotation of the two scans may be significantly different. An accurate registration between the two geometries was easily achieved in our study because the Xradia MicroXCT-400 scanner records the co-ordinates of the iso-center for each scan in terms of global co-ordinate values. Also, while acquiring the different scans, we made sure that the iso-centers of the two scans were co-located at the same z-axis (or vertical) axis value, or that the difference was negligible.

The next step involved up-sampling the forward projected sinogram to the pixel width of the high-resolution sinogram. This was achieved in a similar manner as described in Sec. B.2.3. Finally, the two sinograms were merged, and FBP was applied by using the same parameters as Sec. B.1.1.

B.3 Interior micro-CT with an offset detector array

Three reconstruction algorithms were developed for this study. The starting point for each of the algorithms was a truncated sinogram that had been acquired by an offset detector array. The physical distance (in mm) of the detector offset was also known. All distances (detector length, detector offset etc.) were expressed in terms of image pixel width e.g. the detector offset measured at the detector location was scaled to the equivalent distance at the sample location.

Finally, knowledge of the global object boundary was utilized in the sinogram extrapolation step. In our study, the global scan was available as reference, and the global reconstruction was used to determine the object boundary by a binary thresholding process. The value for thresholding was selected through a trial-and-error method till a sufficiently accurate object boundary was determined. The details of the three algorithms are described in Sec. 4.3.4, and the program parameters are described below.

For the analytic techniques I and II below, and at all offsets, the image reconstruction grid size was chosen such that it covered the FOV at the highest offset. For the iterative technique III, the FOV covered the entire object (i.e. the global support).

B.3.1 Method I: Pre-convolution weighting

The values of Θ and Δ were determined, and the weighting function of Eq. 4.2 was applied. The resultant sinogram was still a truncated sinogram, and sinogram extrapolation was applied next. Cosine extrapolation was employed to roll off the truncated edge to zero. The width of the roll-off was determined from the knowledge of the actual object boundary. Finally, the fan-beam FBP reconstruction algorithm (see Sec. B.1.1) was employed.

B.3.2 Method II: Post-convolution weighting

The first step of this algorithm is sinogram reflection to estimate missing values due to offset detector acquisition. Next, splicing was performed to remove discontinuities at the merged edge. The width over which splicing was performed was set at 100 pixels when data binning was 2. The rest of the procedure was similar to Sec. B.3.1, with a difference in ordering of operations as described in Sec. 4.3.4.

B.3.3 Method III: Iterative reconstruction

In this algorithm, step 1 consisted of a projection completion step that was similar to that in Sec. B.3.1. In step 2, the formula of Eq. 4.2 was applied to weight the projection updates of SART algorithm. The λ parameter of SART was set at 0.8, and the α parameter for TV minimization was set at 0.05. The number of iterations for TV minimization were 5, and the total number of SART-TV iterations were 4. OS-SART was not used, or equivalently, the OS size was one. In step 4, splicing was performed with the same parameters as in Sec. B.3.2.

Appendix C

Publication information

Journal publications

1. Laha, Bireswar, **Kriti Sen Sharma**, James D Schiffbauer, and Doug A Bowman. "Effects of Immersion on Visual Analysis of Volume Data." *IEEE Transactions on Visualization and Computer Graphics (Proceedings of Virtual Reality 2012)* 18, no. 4 (2012).

2. Mishra, S., **Kriti Sen Sharma**, S. J. Lee, E. A. Fox, and G. Wang. "SLATE: Virtualizing Multiscale CT Training." *Journal of X-ray Science and Technology* 20, no. 3 (2012): 383.

3. Schiffbauer, J. D., S. Xiao, **Kriti Sen Sharma**, and G. Wang. "The Origin of Intracellular Structures in Ediacaran Metazoan Embryos." *Geology* 40, no. 3 (January 23, 2012): 223226.
http://geology.gsapubs.org/cgi/doi/10.1130/G32546.1.

4. **Kriti Sen Sharma**, Xin Jin, Christian Holzner, Shree Narayanan, Baodong Liu, Dong Wang, Masoud Agah, Linbing Wang, Hengyong Yu, and Ge Wang. "Experimental Studies on Few-view Reconstruction for High-resolution micro-CT." *Journal of X-ray Science and Technology* 21, no. 1 (January 1, 2013): 2542.
http://www.ncbi.nlm.nih.gov/pubmed/23507850

5. **Kriti Sen Sharma**, Christian Holzner, Dragos M Vasilescu, Jin Xin, Shree Narayanan, Masoud Agah, E. A. Hoffman, Hengyong Yu, and Ge Wang. "Scout-view assisted interior micro-CT", *Physics in Medicine and Biology*, to appear, (2013)

Conference proceedings (full paper)

1. Wang, G., Hengyong Yu, **Kriti Sen Sharma**, Chris Wyatt, L. Wang, Tea Andric, J. Freeman, et al. "Interior Reconstruction for Multi-scale CT Facility." In *1st International Conference on Image Formation in X-Ray Computed Tomography*, 7679. Salt Lake City, UT, 2010.

2. **Kriti Sen Sharma**, S. Seshadri, M. Feser, and G. Wang. "Accurate Resolution Measurement for X-Ray Micro-CT Systems." In *AIP Conference Proceedings*, 1365:337340, 2011.

Conference proceedings (abstracts)

1. **Kriti Sen Sharma**, T Andric, L D Wright, J W Freeman, C L Wyatts, and G Wang. "Micro-CT for Osteon-like Scaffolds." In *11th Annual Conference of the North Carolina Tissue Engineering and Regenerative Medicine Society*. Winston-Salem, NC, 2009.

2. Lee, Spencer J, **Kriti Sen Sharma**, Edward A Fox, Ge Wang, and Matthew Ruder. "Micro-CT Scanner Training in a 3D Virtual World : Second Life Aided Training and Education (SLATE)." In *Annual Meeting of the Biomedical Engineering Society*, 2010.

3. **Kriti Sen Sharma**, D. M. Vasilescu, A. S. Kizhakke Puliyakote, E. A. Hoffman, T. Andric, J. W. Freeman, C. Markert, et al. "Novel Biomedical and Biological Applications Using Lab-based Multi-scale CT System." In *Annual Meeting of the Biomedical Engineering Society*. Hartford, CT, 2011.